



Project Title:

**Innovative compact HYbrid electrical/thermal storage systems
for low energy BUILDings**

Project Acronym:

HYBUILD

Grant Agreement N°: 768824

Collaborative Project

Deliverable Report

Deliverable number:

D2.1

Deliverable title:

Report on adsorber/desorber and evaporator/condenser design and manufacturing

Related task:	2.1
Lead beneficiary:	CNR
Authors and institutions:	CNR - Andrea Frazzica, Valeria Palomba, Alessio Sapienza, Walter Lombardo FAHR - André Große, Ralph Herrmann MIK - Raymund Bastian, Dieter Girlich AKG - Andreas Strehlow, Birgo Nitsch FRESN - Hartmut Schneider, Antoni Castells Sanabra
Due date:	M24 - 30 th of September 2019



This project has received funding from the European Union's Horizon 2020 research and innovation programme under grant agreement No 768824.

The content of this document reflects only the author's view and the Commission is not responsible for any use that may be made of the information it contains.

DISSEMINATION LEVEL		
PU	Public, fully open, e.g. web	X
CO	Confidential, restricted under conditions set out in Model Grant Agreement	
CI	Classified, information as referred to in Commission Decision 2001/844/EC.	

DOCUMENT STATUS HISTORY		
Date	Description	Partner
2019/07/31	First draft	CNR
2019/08/16	Second draft	AKG
2019/08/28	Third draft	CNR
2019/09/02	Fourth draft	FAHR
2019/09/03	Finalized version	CNR
2019/09/20	Internal quality review completed	UDL, R2M, COMSA

Table of contents

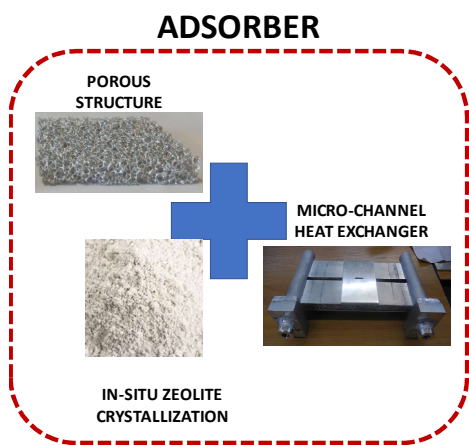
Publishable executive summary.....	5
Acronyms and Abbreviations.....	7
1 Introduction.....	9
1.1 Aims and objectives.....	9
1.2 Relations to other activities in the project	9
1.3 Report structure	9
1.4 Contributions of partners	9
2 Description of the sorption storage concept	10
3 Design and manufacturing of the adsorber	12
3.1 Development of aluminium porous structures	12
3.1.1 Evaluation of heat transfer characteristics of the porous structures	12
3.1.2 Effect of pore density.....	16
3.1.3 Effect of pore density for crystallization process.....	18
3.2 Description of the SAPO-34 in-situ crystallization process.....	20
3.3 Detailed model of the small scale adsorber configurations	20
3.3.1 Model of the porous structure.....	20
3.3.2 Model of the small-scale adsorber	22
3.4 Experimental evaluation of the adsorber performance	27
3.4.1 Testing apparatus.....	27
3.4.2 Testing procedure description	28
3.4.3 Tested adsorber configurations and operating conditions.....	28
3.4.4 Results: typical test detailed analysis.....	31
3.4.5 Results: Comparison of different adsorber configurations.....	34
3.5 Adsorber sizing.....	35
3.6 Full-scale adsorber design and manufacturing.....	37
4 Design and manufacturing of the evaporator/condenser	41
4.1 Lab-scale aluminium HEXs	41
4.2 Lab-scale HEXs testing	43
4.2.1 Testing facilities.....	43
4.2.2 Configurations tested.....	47
4.2.3 Testing procedure – Pool boiling	48
4.2.4 Testing procedure –Thin film evaporation.....	49
4.2.5 Data reduction	49

4.2.6	Example of a typical test – 0° configuration, pool boiling, submersed HEX	50
4.2.7	List of tests – pool boiling	53
4.2.8	Test results -pool boiling.....	55
4.2.9	Comparison of the different arrangements.....	62
4.2.10	Configurations with variable level of the refrigerant.....	63
4.3	Test results – thin film evaporation.....	65
4.3.1	Effect of HTF flow rate	65
4.4	Semi-empirical models for the investigation of water evaporation under sub-atmospheric pressure conditions - pool boiling	67
4.4.1	Identification of the evaporation mechanism	67
4.4.2	Semi-empirical model	71
4.5	Full-scale evaporator/condenser design and manufacturing.....	72
5	Conclusions.....	75
6	References.....	76

Publishable executive summary

HYBUILD is an EU Horizon 2020-funded project, led by COMSA Corporación, which will develop two innovative compact hybrid electrical/thermal storage systems for stand-alone and district connected buildings.

The present report describes the activity regarding the development of the sorption module, that is an essential part of HYBUILD Mediterranean solution, since it allows the operation of the compression with high efficiency by storage and conversion of solar energy. The main components that were optimised within WP2 of HYBUILD project are the adsorber and the evaporator of the sorption module. The main innovation proposed in the adsorber is the integration of a porous structure, onto which zeolite is crystallised by means of a patented technique by FAHR, inside the micro-channel heat exchanger realised by AKG. To this aim, numerical and experimental activity were coupled. At first, heat transfer in different porous structures was evaluated and subsequently the most promising one were chosen for testing in

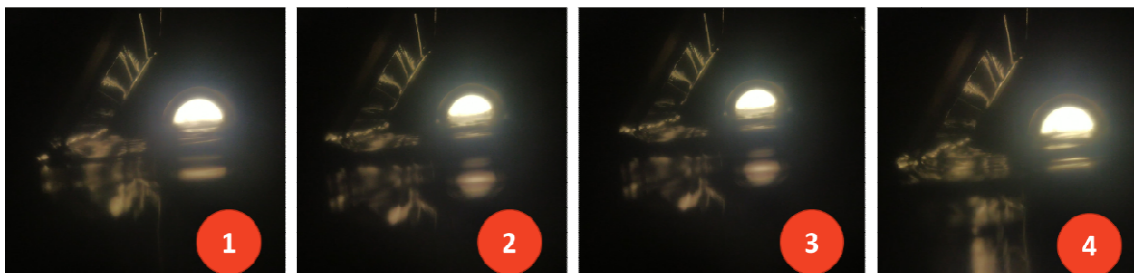


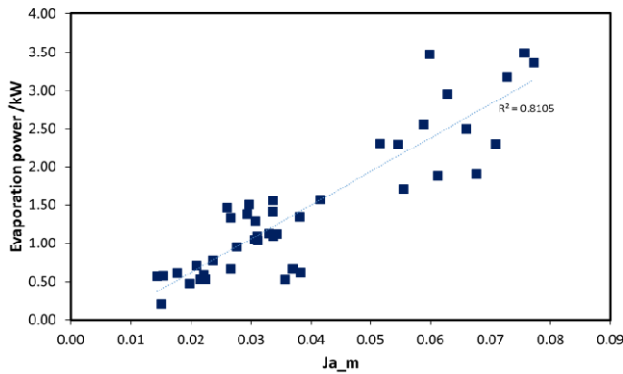
small-scale adsorbers in a set-up already present at ITAE (Gravimetric Large Temperature Jump apparatus). The different porous structures coated and evaluated are: (i) high density pressed fins produced by AKG, (ii) aluminium foams produced by AKG, (iii) aluminium foams produced by MIKR, (iv) aluminium chips produced by MIKR. The results of the activity allowed the identification of the volumetric and mass-specific cooling power that each structure can achieve and the final selection for full-scale adsorber. High-density pressed fins showed the best performance and therefore the full scale adsorber was designed and manufactured by FAHR and AKG. The results of the experimental testing were also used to implement a

COMSOL model that was validated and that can be employed for the optimization of the system.



The full-scale adsorber has a fin space area of around 33 m² with two of those heat exchangers combined in one module. This allows for achieving the required minimum of 50 m² fin space area needed to generate a zeolite mass between 11 to 13 kg.





The second focus of the activity of T2.1 was the experimental evaluation of evaporators for sub-atmospheric evaporation conditions, typical of sorption systems. To this aim, a microchannel aluminium heat exchanger with high density aluminium fins by AKG was tested in a testing rig that was specifically built at ITAE. Two evaporation mechanisms were tested: pool boiling and thin film evaporation,

since they correspond to the possible evaporation mechanisms that can be used in a sorption module if combined with a compression chiller, as in the HYBUILD solution. For the pool boiling case, different configurations were tested, i.e. 0°, 45° and 90°, as well as different filling levels of the vessels. For each case examined, the evaporation power and the heat transfer coefficient were measured/calculated. The activity was completed with the evaluation of semi-empirical models for the systematic design of such components. To this purpose, the evaporation mechanism was visualised and the possibility of applying correlations based on modified dimensionless groups commonly applied in fluid-dynamic was evaluated. The results demonstrated that it is possible to adequately correlate the conditions under which evaporation occurs (i.e. temperature and pressure in the condenser and evaporator) to the power and heat transfer coefficient of the heat exchanger. According to possible issues arising from the partial corrosion of aluminium in contact with water under vacuum conditions, it was decided to proceed with the design and manufacturing of a copper-based heat exchanger, acting as evaporator/condenser, exploiting capillary effect to operate under thin film evaporation conditions. Fahrenheit will size it according to the final capacity of the adsorbers, to properly operate the whole adsorption module.

Acronyms and Abbreviations

Bo	Bond number
C	Concentration, mol/m ²
c _p	Specific heat, kJ/kg K
D	Diffusion coefficient, m ² /s
h	Convective heat transfer coefficient, W/(m ² K)
H	Enthalpy, kJ
Ja	Jakob number
k	Thermal conductivity, W/(mK)
Ku	Kutateladze number
m	Mass, kg
\dot{m}	Mass flow, kg/s
Nu	Nusselt number
p	Pressure, Pa
Pr	Prandtl number
q	Phase change enthalpy, kJ/kg
\dot{Q}	Thermal Power, kW
r	Radius, m
R	Universal gas constant, kJ/(kg K)
Re	Reynolds Number
SCP	Specific cooling power, W/kg
t	Time, s
T	Temperature, °C
U	Heat transfer coefficient W/(m ² K)
v	Specific volume, m ³ /kW
V	Volumetric flow rate, l/min
w	Uptake, kg/kg

Greek letters

α	Heat transfer rate, W/s
β	Expansion coefficient, 1/K
ε	porosity
ρ	Density, kg/m ³

σ Surface tension N m

Subscripts

ads adsorption

ave average

c condenser

crit critical

des desorption

e evaporator

eff effective

eq equilibrium

ext external

i internal

in inlet

lam laminar

liq liquid

m modified

out outlet

sat saturation

sorb sorbent

turb turbulent

v vapour

Abbreviations

Ad Adsorber

HEX Heat EXchanger

LMTD Logarithmic Mean Temperature Difference

LTJ Large temperature Jump

G-LTJ Gravimetric large Temperature Jump

1 Introduction

1.1 Aims and objectives

In this deliverable a detailed analysis of the activities performed in the course of Task 2.1 of HYBUILD, focused on the development of core components of the sorption module, are reported. The aim of the activity was to develop efficient components through detailed theoretical and experimental investigation at lab level, in order to optimize the design of the full-scale components. In particular, the activity on the adsorber aimed at the identification of the optimal porous structure to be included inside the HEX, focusing on maximising the achievable specific power, to keep the overall volume as limited as possible. This was obtained by developing a detailed numerical heat and mass transfer model, validated through experimental data on small-scale adsorbers. The evaporator/condenser was carefully investigated experimentally, by analysing different HEX positioning and varying the boundary conditions. The experimental results were then used to create a semi-empirical model for assisting the design of the full-scale component.

1.2 Relations to other activities in the project

The activity presented in this report was carried out within the Task 2.1, aiming at the theoretical and experimental development of core components of the sorption module, which will allow developing the final prototype to be tested in the lab within Task 3.2 and then installed in the demo sites within WP6. Some of the details related to the manufacturing process will be also useful for the life cycle analysis in WP5.

1.3 Report structure

This deliverable is structured as follows:

- Section 2: description of the sorption module concept and its operation inside the HYBUILD Mediterranean concept;
- Section 3: theoretical and experimental analyses for the development and the manufacturing of the final adsorber configuration;
- Section 4: theoretical and experimental analyses for the development and the manufacturing of the final evaporator/condenser configuration;
- Section 5: description of the full-scale sorption module manufacturing.

1.4 Contributions of partners

Fahrenheit, as task leader, supervised the activities concerning the design and manufacturing of the core components. CNR, was in charge for the main experimental activity concerning the core components characterization as well as the development of theoretical and semi-empirical models for supporting the design of the final components. AKG, as heat exchangers manufacturing company, supported the design and manufacturing of the lab-scale HEXs as well as the full-scale ones. Mikrometal delivered the porous structures for the adsorber manufacturing. Fresnex supported the analysis of operating conditions of the sorption module.

2 Description of the sorption storage concept

HYBUILD solutions for the Mediterranean climate is meant to ensure comfort condition in residential buildings by specifically targeting cooling production, since it represents the most critical operating conditions. To this aim, a DC-driven chiller is coupled to a hybrid storage system that allows to efficiently convert and store energy to increase the share of renewables in summer and winter conditions. In particular, the sorption storage allows increasing the efficiency of the compression chiller by reducing the temperature lift between evaporator and condenser. The sorption storage exploits thermal energy from linear Fresnel collectors to obtain a cooling effect at the evaporator, that is connected to the condenser of the compression chiller. In order to obtain a constant useful effect, the sorption storage is based on a two-adsorbers architecture that work in counter-phase, as shown in Figure 1.

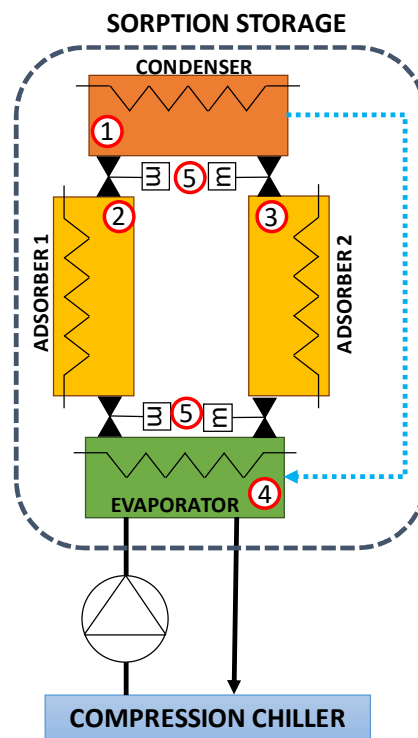


Figure 1: Overall sorption storage layout and connection to the compression chiller. 1: condenser, 2-3: adsorbers, 4: evaporator

The main innovative parts of the storage system are the adsorber with enhanced heat and mass transfer properties and the optimised evaporator. The overall concept for the development of the adsorber is shown in Figure 2: the sorbent material is SAPO-34 zeolite that is directly synthesized using Fahrenheit patented technology onto an enhanced support structure, i.e. aluminium foam produced by Mikrometal and embedded in a microchannel heat exchanger produced by AKG.

The optimized evaporator is based on an aluminium HEX with high-density fins produced by AKG, whose configuration was optimised for pool boiling evaporation under sub-atmospheric pressures. The possibility of direct integration of the evaporator as an integrated evaporator/condenser, i.e. by connecting the HEX directly to the refrigerant loop of the compression chiller was evaluated and specific tests were carried out within WP3 activities.

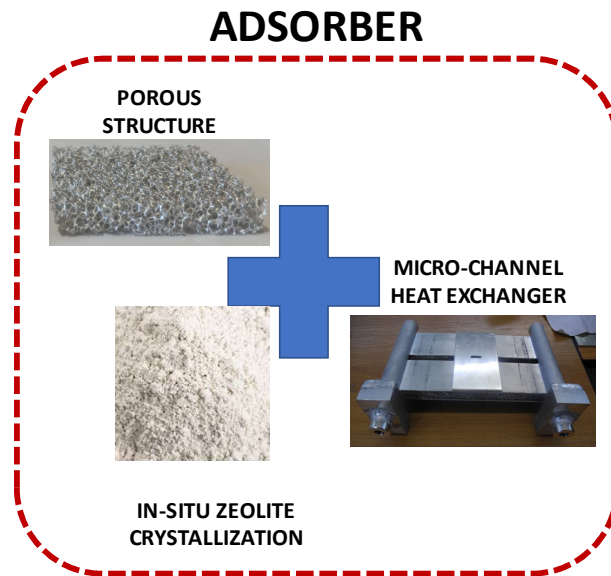


Figure 2: Overall concept for the adsorber development.

The development of the sorption storage is schematically summarised in Figure 3. As it is possible to notice, both the activities that led to the realisation of the adsorber and the evaporator consist of two phases: a first one coupling experimental and numerical activity, to get the optimised design of the component as outcome, and the realisation of the component. Small-scale samples were provided by technology manufacturers and tested at CNR, whereas the full-scale components for prototypes to be installed in demo sites were realised by a synergistic collaboration between Mikrometal, Fahrenheit and AKG.

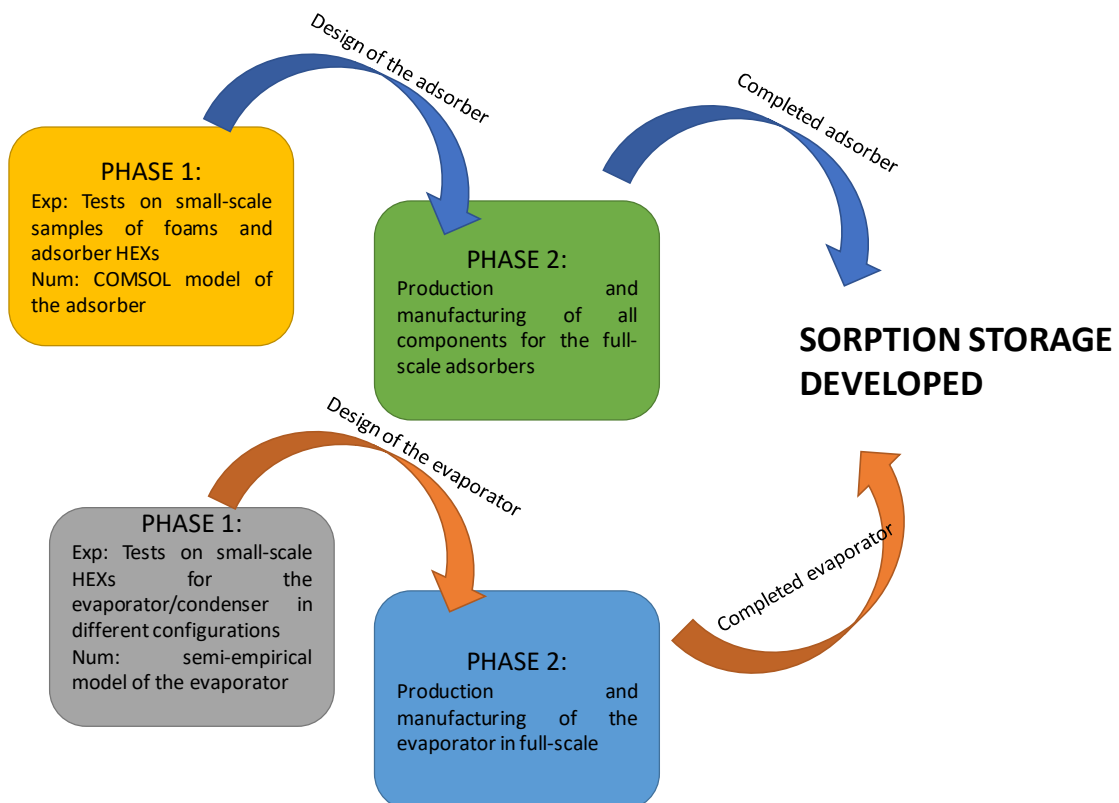


Figure 3: Process of development of sorption storage in HYBUILD.

3 Design and manufacturing of the adsorber

3.1 Development of aluminium porous structures

3.1.1 Evaluation of heat transfer characteristics of the porous structures

A first experimental activity was devoted to the evaluation of heat transfer features of different aluminium foam samples, in order to identify the most promising candidates for zeolite synthesis. To this aim, samples with different pore densities and thicknesses were realized. A list of the available samples is shown in Table 1. Instead, Figure 4 shows the pictures of the samples with different pore densities. It is worth remarking that the slightly different colours of the samples are due only to different ambient conditions during synthesis.

Table 1: Samples of Al foam tested.

Sample n.	Pore density (PPI)	Thickness (mm)
1	10	10
2	10	20
3	10	40
4	20	8
5	20	15
6	20	27
7	30	12
8	30	20
9	40	15

In order to have a more complete information on the morphology of the materials, an optical microscope was used for the visual characterization of the samples. The pictures in Figure 5 show the details of one cell for the samples with different pore density, with the dimensions indicated.

(a)10 ppi



(b)20 ppi



(c)30 ppi

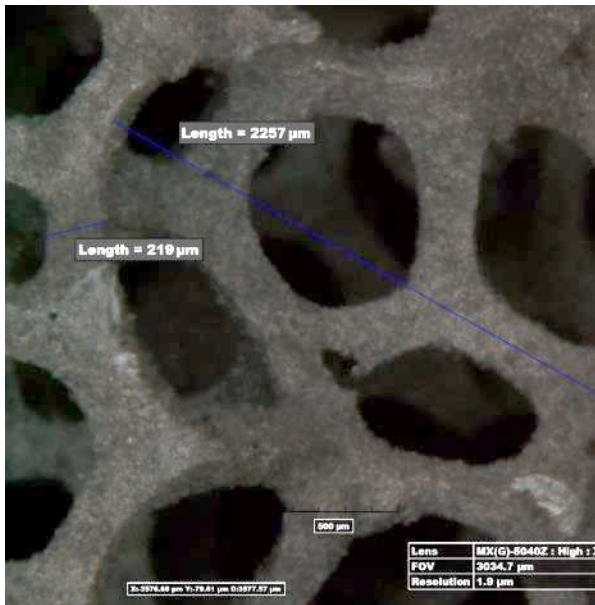


(d)40 ppi



Figure 4: Pictures of the samples with different pore densities.

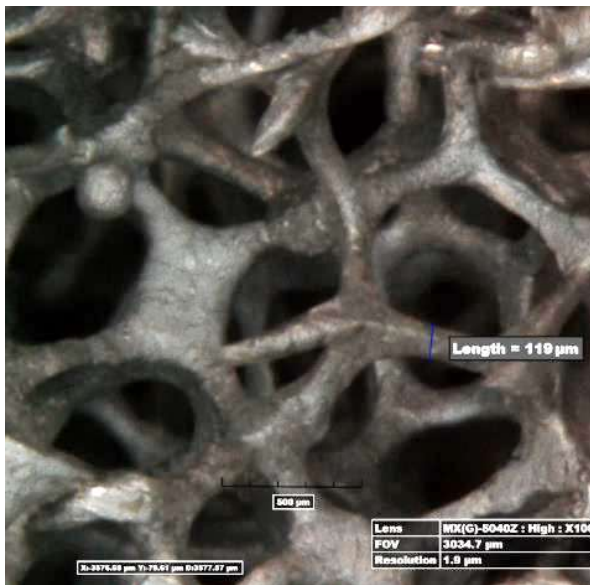
(a)10 ppi



(b)20 ppi



(c)30 ppi



(d)40 ppi

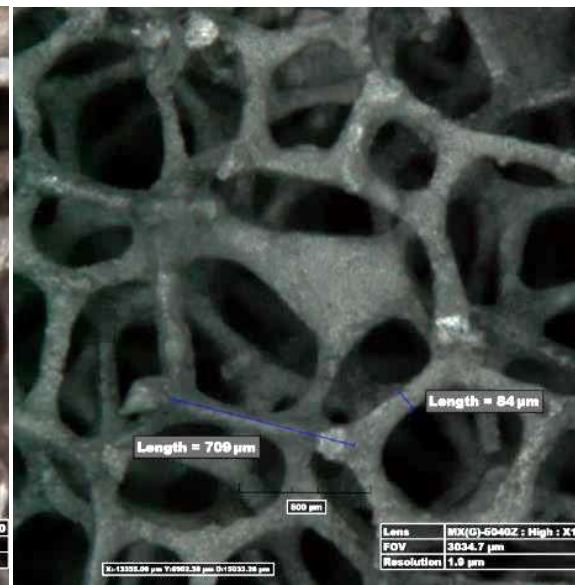


Figure 5: Microscopic enlargement of the samples with different pore densities.

For the measurements on heat transfer characteristics of aluminium foams, an experimental setup already present at CNR-ITAE lab was used, whose schematic layout is shown in Figure 6. It consists of a series of Peltier cells onto which the samples have been placed, using thermal paste to improve thermal contact between the cell and the sample. The bottom part of the Peltier cell is connected to a heat sink with fans for the dissipation of the heat. The cells are electrically connected to a time-controlled relay circuit that allows changing the polarity of the voltage on the cell, thus performing heating and cooling cycles. The temperature of the cell and on the upper surface of the sample is measured by means of type T thermocouples. In addition, a Raytek Instruments Marathon MM infrared temperature sensor is used to monitor and record the temperature of the sensor without the need for thermal contact with the foam. All the temperature signals are acquired and monitored by means of a NI cFP acquisition system.

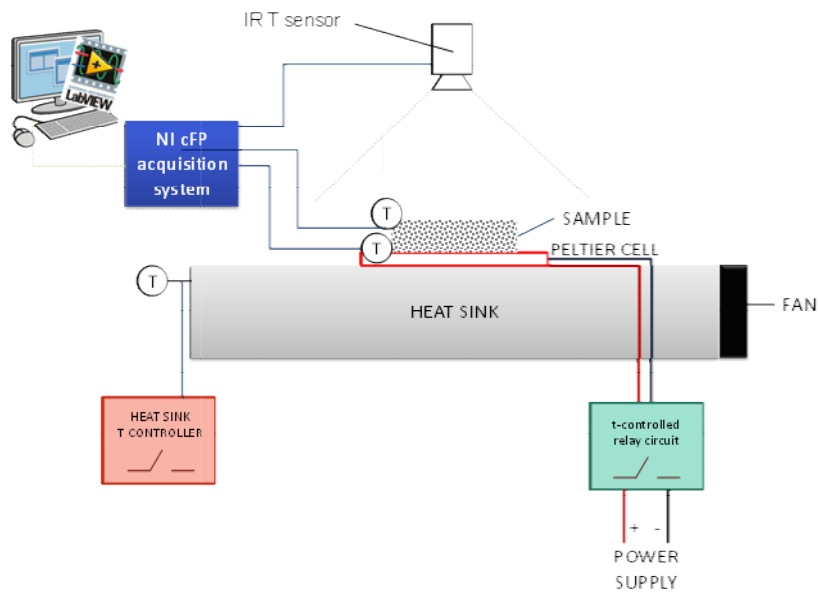
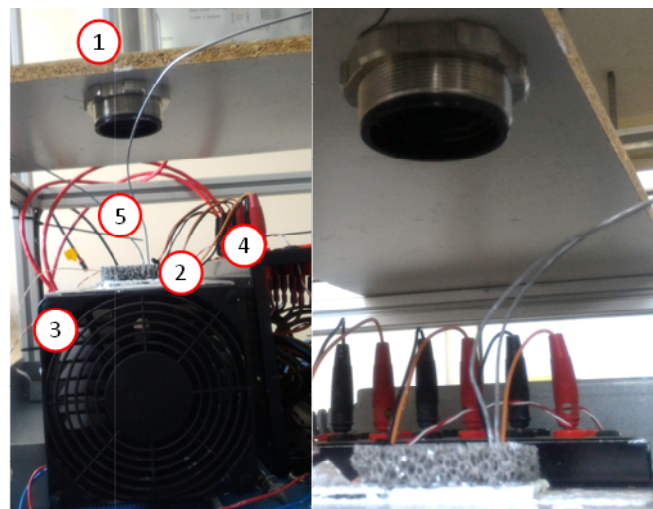


Figure 6: Schematics of the apparatus for heat transfer measurements.

Some pictures of the experimental apparatus during the measurement campaign are shown in Figure 7.



- 1: IR temperature sensor
- 2: sample on Peltier cell
- 3: heat sink
- 4: electronics
- 5: thermocouples

Figure 7: View of the experimental setup at CNR-ITAE.

3.1.1.1 Experimental procedure

For the comparison of heat transfer capability of the various system, two tests were done, by changing the duration of the cycle time (i.e. the cumulative time of a heating and cooling ramp). The two cycle times selected were 2 minutes (1 minute heating + 1 minute cooling) and 6 minutes (3 minutes heating + 3 minutes cooling). All the tests were started when the samples were at room temperature. The heating and cooling rate of the Peltier cell and the magnitude of the supply voltage were not changed, in order to have constant and reproducible boundary conditions. For both cycle times, 5 cycles were completed and the results of the last three were used for data reduction and the subsequent calculations.

In order to analyze the experimental results, the following parameters were calculated:

- maximum and minimum temperature during the tests with 1 minute ramp $T_{max,1}$ and $T_{min,1}$;
- maximum and minimum temperature during the tests with 3 minutes ramp $T_{max,3}$ and $T_{min,3}$;
- the time difference between the minimum and the maximum temperature during each one of the 6 minutes' cycles ΔT_3 ;
- the average heating rate, calculated as:

$$\alpha = \frac{T_{max,3} - T_{min,3}}{\Delta T_3} \left[\frac{^{\circ}C}{s} \right]$$

3.1.1.2 Results

Figure 8 and Figure 9 give an example of the results recorded during a test, showing the temperature evolution of the Peltier cell and of the upper surface of the sample measured with two thermocouples (T1 and T2) and with the IR temperature sensor (T_IR). Both tests are done on a sample with pore density of 30 PPI and 10 mm thickness.

During the tests with cycle time of 2 minutes, the samples don't reach equilibrium, whereas a plateau in the maximum temperature reached by the samples is observed in the tests with 6 minutes cycle time. The results for the three consecutive cycles analyzed in both cases are very similar, thus indicating a good reproducibility of the measurement. The temperature difference between the Peltier cell and the upper surface of the sample is around 20°C and can be explained by the imperfect contact between the cell itself and the sample and the heat losses through the environment, since the samples are not thermally insulated. The difference in the temperature measured by the three different temperature sensors depends on their response time (e.g. the IR sensor is able to better follow the dynamic trend. However, it is within the uncertainty of the instruments and the trend for each of them in the various cycles is repeatable. It is therefore possible to consider that the system behaves homogeneously. For all the calculations, the average temperature of the sensors will be considered.

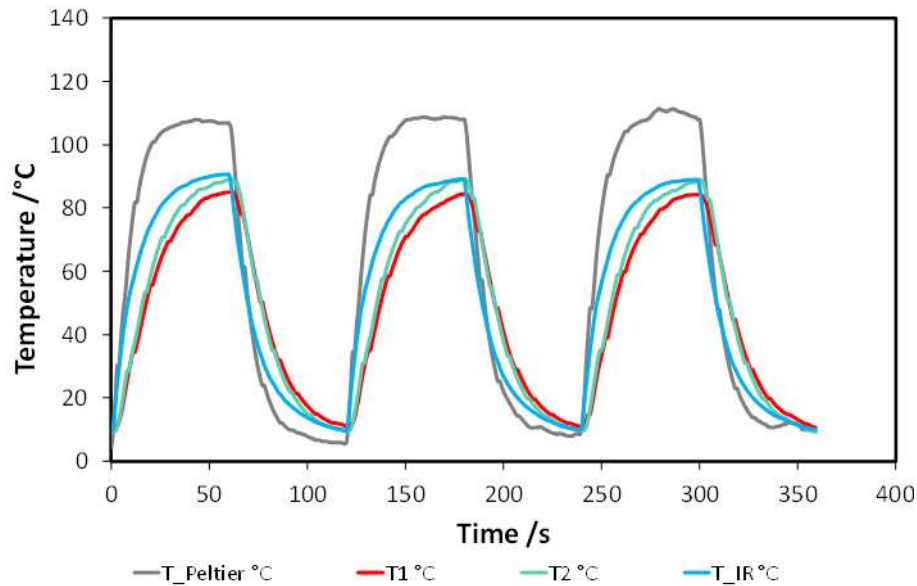


Figure 8: Temperature evolution for a test with cycle time of 2 minutes. Sample: 30 PPI, 10 mm thickness.

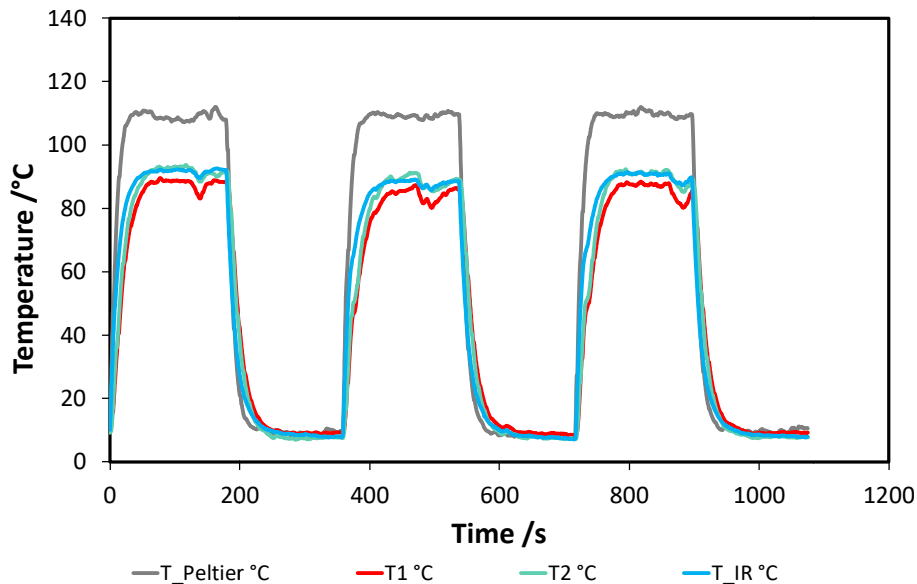


Figure 9: Temperature evolution for a test with cycle time of 6 minutes. Sample: 30 PPI, 10 mm thickness.

3.1.2 Effect of pore density

The first parameter whose effect was evaluated is pore density. In particular, the following samples were chosen:

- 40 PPI and 15 mm thickness,
- 30 PPI and 12 mm thickness;
- 20 PPI and 8 mm thickness;
- 10 PPI and 10 mm thickness.

The results are reported in Figure 10, in terms of the maximum and minimum temperature reached during the tests with a cycle time of 2 minutes. Apparently, a slightly different temperature is reached by the different samples. However, this is mainly due to the thickness of the sample, rather than pore density: the sample with the highest $T_{max,1}$ and lower $T_{min,1}$ is the one with pore density of 20 PPI, which has also a slightly lower thickness. Instead, the one

with the lower $T_{max,1}$ and the maximum $T_{min,1}$ is the one with pore density of 40 PPI, which is also the one with a higher thickness. It is therefore possibly to conclude that pore density does not hold a significant effect.

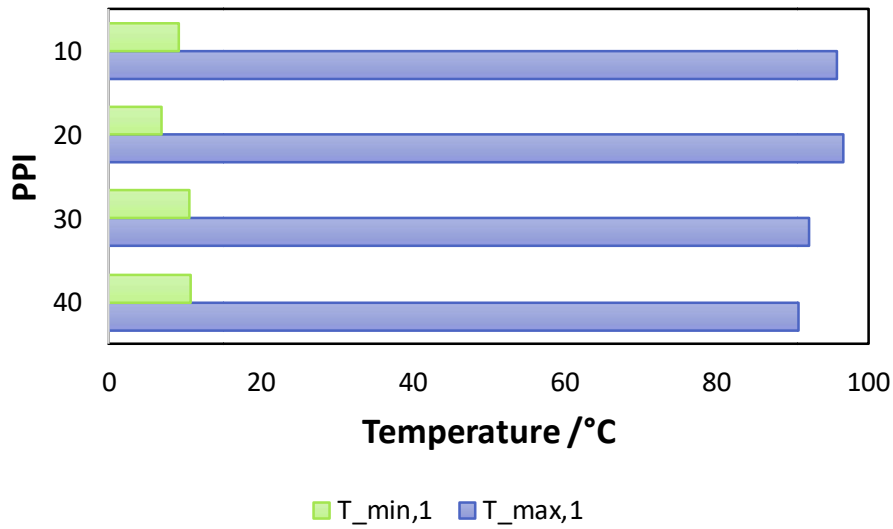


Figure 10: Effect of pore density.

The predominant effect of sample thickness over pore density is further remarked by the results reported in Figure 11 and Figure 12 that present $T_{max,1}$ and $T_{min,1}$, respectively, as a function of the thickness of the sample. The curves are parameterised according to the pore density of the foam. There is a clear trend with increasing $T_{min,1}$ for an increasing sample thickness and a decreasing $T_{max,1}$ for increasing sample thickness, disregarding of the pore density of the examined sample. This is particularly evident looking at the points for the 20 PPI, 30 PPI and 40 PPI samples at around 15 mm thickness of Figure 11 that are almost superimposed.

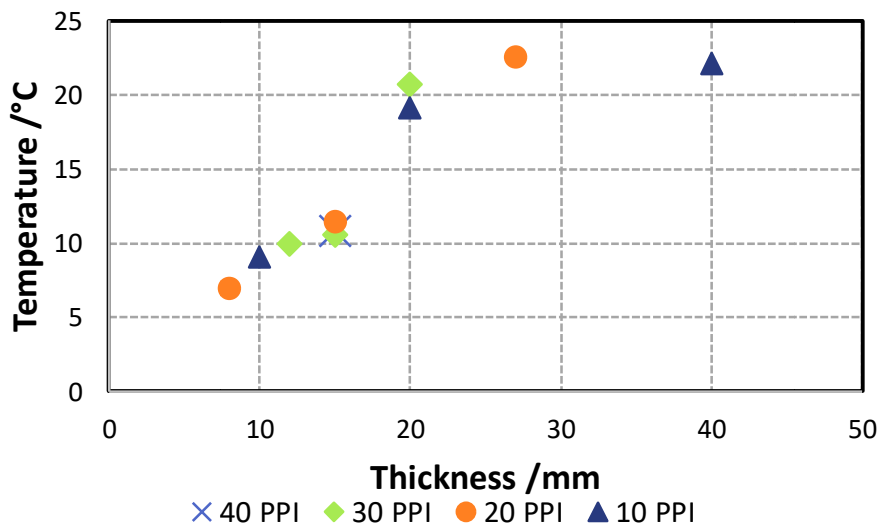


Figure 11: Effect of sample thickness on $T_{min,1}$.

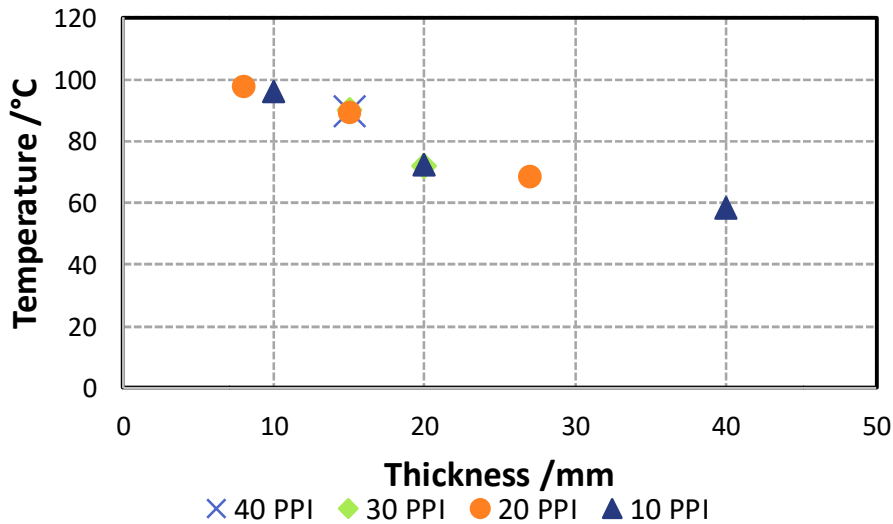


Figure 12: Effect of sample thickness on $T_{max,1}$.

The linear trend of decreasing temperature with increasing sample thickness is particularly evident in Figure 12, with the points relative to different pore densities but the same sample thickness almost superimposed. Furthermore, the heating rate α was calculated for the different tests carried out and is shown in Figure 13: the linear trend is similar to that already discussed. Consequently, in order to derive a parameter useful for system sizing, a corrected equivalent heating rate was calculated, averaged on all the measures taken:

$$\alpha' = 5.2 \cdot 10^{-3} \frac{K}{m s}$$

Such a parameter can be useful for sizing of a system employing the materials tested.

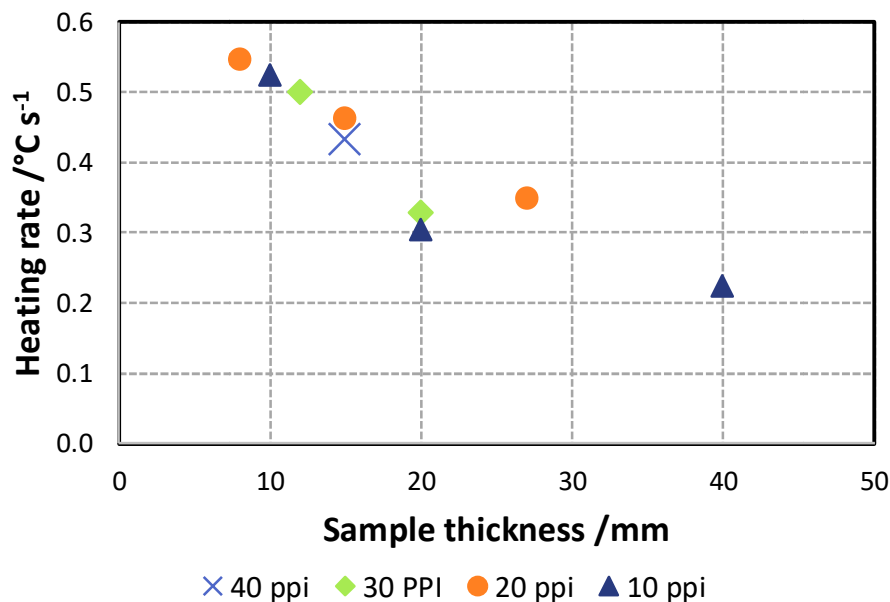


Figure 13: Effect of sample thickness on α .

3.1.3 Effect of pore density for crystallization process

For the crystallization process at FAHR and for good HEX configurations the foams from MIKR should fulfil defined constraints: enough surface area for high zeolite densities, the right wire thickness (in the crystallisation process a part of the Al structure will be dissolved and therefore too thin thickness means collapse of the structure and instability of the zeolite) and

a really plane structure between the foam and the hydraulic channel for good heat transfer. All these features are difficult and limited in the manufacturing process by MIKR at the moment because there is a compromise between the porosity and the right wire thickness. For that reason, FAHR pressed some of the best samples with 20ppi and 30ppi to half height for a better surface/volume ratio. This ratio determines the chemical solution for the crystallization process. Before the process starts, the foams will be cleaned in an aqueous solution to avoid any impurities (oils, fats). A picture of pressed samples is shown in Figure 14.

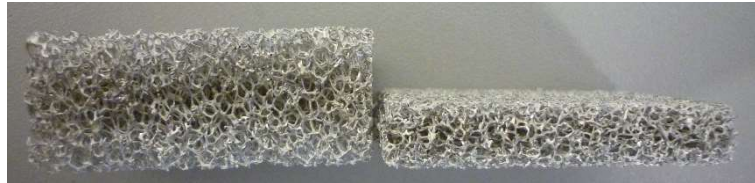


Figure 14: Pressed foam sample (20ppi)

Nonetheless, the crystallization process resulted in a strong dissolution of the foam (see Figure 15). It shows the reduction of the strut diameter caused by dissolution of the aluminum. During the reaction, the struts are not protected by the crystallized zeolite, instead it mainly crystallizes as a powder. After the experiment, the struts appear quite bare.



Figure 15: Wire thickness before and after crystallization process of non-useful foam sample

Therefore, it is possible to state that the use of the tested foams as high surface support in directly zeolite coated adsorber heat exchangers leads the following problems:

- the foams porosity is too high and thus achievable, calculated zeolite mass and resulting sorption power will be too few for efficient products;
- pressing the foams supplies more coatable Al surface but is accompanied with strong strut bending which induces cracks in the Al where stronger chemical dissolution occurs, leading to a significant loss of mechanical stability of the structure;
- for production reasons the strut thickness is strongly related to pore density: desired smaller pores will result in smaller strut diameters and in loss of mechanical stability;
- crystallization recipe can be adapted to some extent but will require foam porosity less 70% and strut thickness $>170 \mu\text{m}$;
- for later power density foam porosity should be in the range of 60-70%.

For such reasons, it was decided to test also other two possible porous structures, such as high-density finned packs, by AKG, and Aluminium chips, as described in the following paragraphs.

3.2 Description of the SAPO-34 in-situ crystallization process

Fahrenheit uses the Partial Support Transformation (PST) process to grow zeolites in an in-situ crystallization on the surface of metallic aluminium parts, e.g. on heat exchangers or HEX samples. The resulting zeolite layers are in best contact to the aluminium enabling fast heat transfer and very good mechanical stability.

The treatment takes place in a pressure tight reactor at temperatures up to 200°C. Due to the oxidation of the aluminium hydrogen is formed and has to be released continuously. In the crystallization process the hydraulic circle of the HEX has to be protected from the reaction liquid to avoid pressure drop increasing zeolite precipitates in the tubes. For smaller HEX samples reaction conditions were adapted.

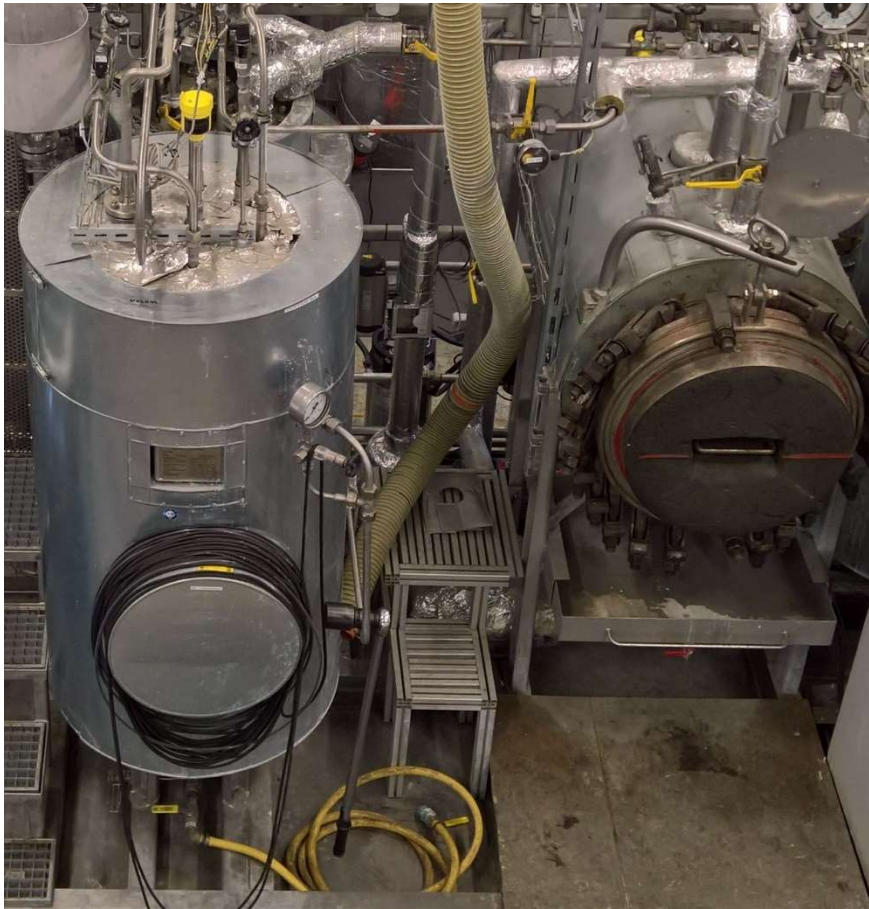


Figure 16: Fahrenheit pilot plant with PST reactor.

After the PST coating the HEX or samples are removed from the reactor, washed and dried.

The amounts of zeolites on the adsorber HEX/samples are documented after the calcination which is required to get rid of capacity limiting molecules in the pore system.

3.3 Detailed model of the small scale adsorber configurations

3.3.1 Model of the porous structure

Prior to the realization of the model for the small-scale adsorber, the results from the tests on porous structures described in section 3.1.1 were used to realize a validated model of the

porous structure. To this aim, COMSOL Multiphysics environment was selected, considering its wide use in the solutions of problems with coupled heat and mass transfer [1]. A simplified geometry was considered, with a regular distribution of the pores. Indeed, since the experimental testing proved that the material behaves homogeneously, this is a realistic assumption. The 3-dimensional geometry simulated and the boundary and initial conditions are shown in Figure 17.

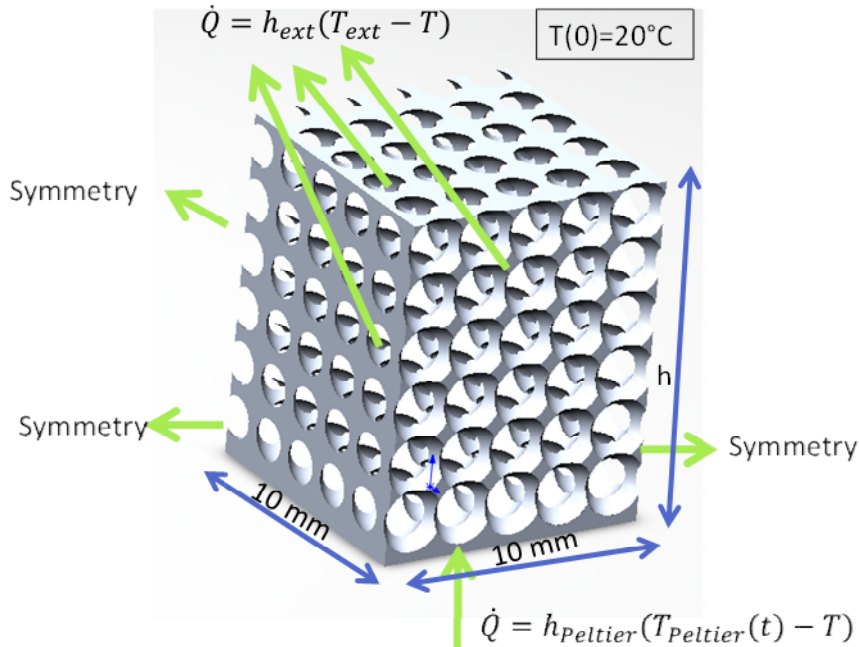


Figure 17: Geometry, initial and boundary conditions of the numerical model.

The dominant heat transfer mechanism is conduction and therefore can be described by means of Fourier's law:

$$\rho c_p \frac{\partial T}{\partial t} - k \nabla^2 T = \dot{Q}$$

Where: ρ is the material density [kg/m^3], c_p is the specific heat capacity [$\text{J}/(\text{kg K})$], k is the thermal conductivity [$\text{W}/(\text{m K})$] and \dot{Q} the thermal source [W].

The following boundary conditions were applied:

- symmetry on three sides of the modelled geometry;
- convective heat transfer between the Peltier cell and the sample. Since a good thermal contact was considered, a heat transfer coefficient h_{Peltier} of $1000 \text{ W}/\text{m}^2\text{K}$ was imposed. The temperature evolution of the Peltier cell during experimental measurement was used.
- natural convection between all the external surfaces of the sample and the ambient air. The coefficient of heat transfer h_{ext} was considered equal to $5 \text{ W}/\text{m}^2\text{K}$ [2].

Figure 18 shows the comparison of numerical and experimental results for a sample with 10 PPI pore density, 10 mm thickness and cycle time of 6 minutes. As it is possible to notice, there are no significant deviations of the experimental and numerical results, thus confirming that the model is able to accurately reproduce the experiments carried out and represents a good sizing tool.

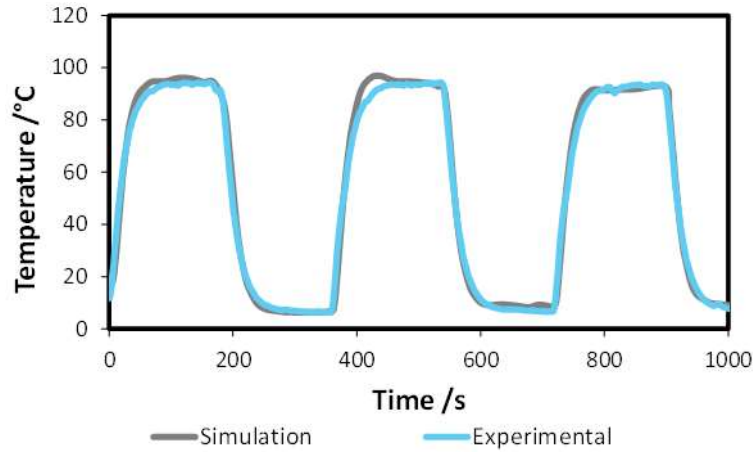


Figure 18: Comparison of numerical and experimental results.

The model developed was then adapted to implement an “equivalent” material, with the aim of simplifying the subsequent modeling of the foam + zeolite system. In particular, the rule of mixtures was used to define the equivalent density and specific heat of the solid, starting from the data of the aluminum alloy and air. Regarding thermal conductivity, the empirical correlation experimentally validated on aluminum foams in [3] was used:

$$k_{eff} = k_{air} \left[\varepsilon + A(1 - \varepsilon)^n \frac{k_{Al}}{k_{air}} \right]$$

with $A=0.181$ and $n=0.763$.

The final equivalent material is then defined by an equivalent thermal conductivity $k_{eff}=4.5 \text{ W m}^{-1} \text{ K}^{-1}$, $cp_{eff}=87 \text{ kJ kg}^{-1} \text{ K}^{-1}$ and $\rho_{eff}=290 \text{ kg m}^{-3}$. The comparison of the simulation for the material with the equivalent properties and the experimental data on the foams with 20 PPI and 20 mm thickness are reported in Figure 19. As it is possible to notice, the deviation is within measurement uncertainty and the proposed equivalent material can be therefore used as starting point for the definition of the COMSOL model of the small-scale adsorber.

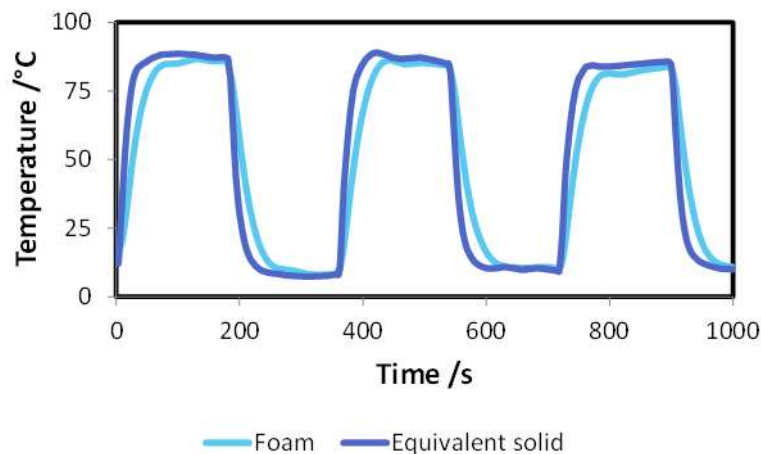


Figure 19: Verification of equivalent solid for modeling purposes.

3.3.2 Model of the small-scale adsorber

The model for the small scale adsorber realized in COMSOL Multiphysics is obtained by considering a 3D component with 2 domains: the sorbent domain and the water vapour domain.

3.3.2.1 Assumptions and main equations

The following assumptions were used [1]:

- the adsorbent is isotropic and has a uniform porosity
- the solid phase is in local thermal equilibrium with the adsorbate in the adsorbed phase.
- the gas phase is ideal
- the effective intra-particle diffusivity is temperature independent
- the channels of the heat exchangers are not simulated and a proper boundary condition is used instead
- the vapor phase surrounding the adsorbent grain is stagnant and at a constant pressure.
- radiation and heat losses/gain to the ambient have been neglected

The energy balance inside the sorbent domain can be described by:

$$(\rho c_p)_{sorb} \frac{\partial T}{\partial t} - \frac{\rho_{sorb}}{M} \Delta H \frac{\partial w}{\partial t} = \nabla(\lambda_{sorb} \nabla T_{sorb})$$

Whereas the mass balance inside the sorbent domain is given by:

$$\frac{\partial C}{\partial t} = \nabla(D \nabla C) - \frac{\rho_{sorb}}{\varepsilon} \frac{1}{M} \frac{\partial w}{\partial t}$$

And the energy balance inside the water vapor is:

$$\rho_v c_{p_v} \frac{\partial T_v}{\partial t} - \nabla(\lambda_v \nabla T_v)$$

The pressure of the gas is obtained from the ideal gas relationship:

$$p = RT_{sorb}(t)C(t)$$

Sorption dynamics is described by the Linear Driving Force model [4]:

$$\frac{\partial w}{\partial t} = D_{eff}(w_{eq} - w)$$

3.3.2.2 Equivalent properties

The sorbent domain in the model represents an “equivalent” material, which takes into account the properties of the aluminum porous structure + coating. As specified in the previous section, the aluminum foam can be described, in turn, as an equivalent solid with effective properties. In addition, from the measurements done at Fahrenheit, the estimated zeolite load (137 g_{zeolite}/dm³foam) was used to calculate the amount of coating, ca. 13%V and the apparent density of the solid. In order to derive the specific heat capacity of the solid, the rule of mixtures was then applied. Instead, to calculate the equivalent thermal conductivity of the zeolite + aluminium foam mixture, the overall thermal conductivity was calculated as:

$$k_{sorb} = (t_{coating} + t_{foam\ wall}) \left(\frac{t_{coating}}{k_{coating}} + \frac{t_{foam\ wall}}{k_{foam}} \right)^{-1}$$

The equivalent properties of the sorbent material calculated are then: $k_{sorb}=1.1 \text{ W m}^{-1} \text{ K}^{-1}$, $cp_{sorb}=220 \text{ kJ kg}^{-1} \text{ K}^{-1}$ and $\rho_{sorb}=290 \text{ kg m}^{-3}$

Since the small-scale adsorbers realized for the lab-testing activity were based on SAPO-5 as adsorbent material (belonging to the same family of the SAPO-34), the adsorption equilibrium of the SAPO-5 was calculated fitting the experimental data provided by Fahrenheit. The adsorption uptake as a function of the adsorption potential $A = \frac{R}{M} T_{sorb} \log \frac{p_{sat}(T_{sorb})}{p}$ is shown in Figure 20.

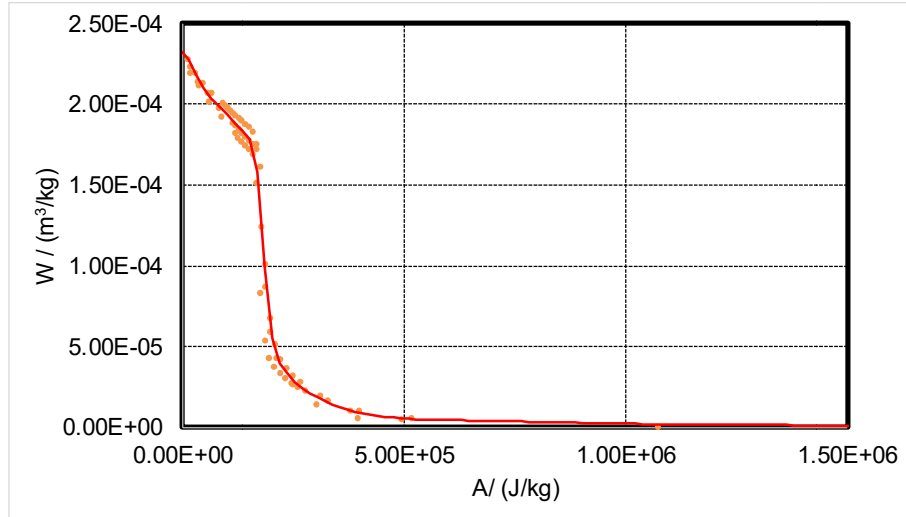


Figure 20: Adsorption capacity of SAPO-5.

The adsorption enthalpy is derived from the characteristic material equation:

$$\Delta H = q_{ev} + A - T_{sorb} \beta \frac{\partial A}{\partial \log w}$$

3.3.2.3 Initial and boundary conditions

The initial and boundary conditions used are schematically presented in Figure 21 and Figure 22, respectively. At the initial time, the concentration of water molecules in the sorbent is constant and corresponds to the equilibrium concentration at the initial pressure p_0 in the adsorber and at the initial temperature. The temperature of the sorbent and gas domains is constant and equal to T_0 .

The boundary conditions applied include convective heat transfer at the channel plate/sorbent interface and the equilibrium concentration of water vapor molecules with varying temperature of the sorbent.

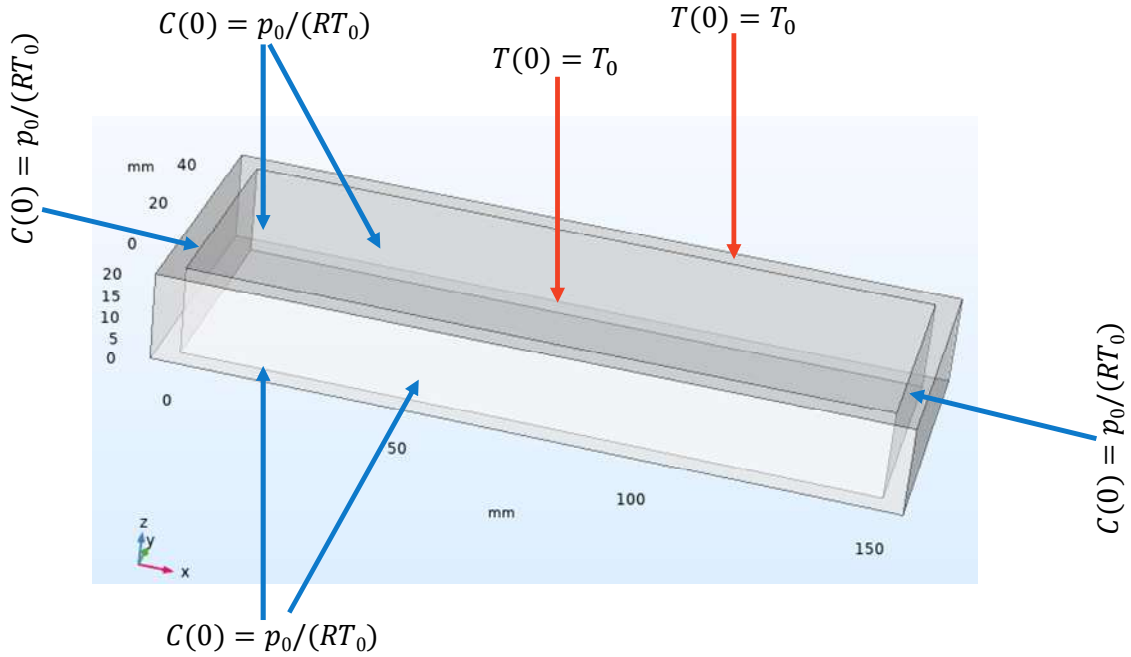


Figure 21: Initial conditions used in the model of the small-scale adsorber.

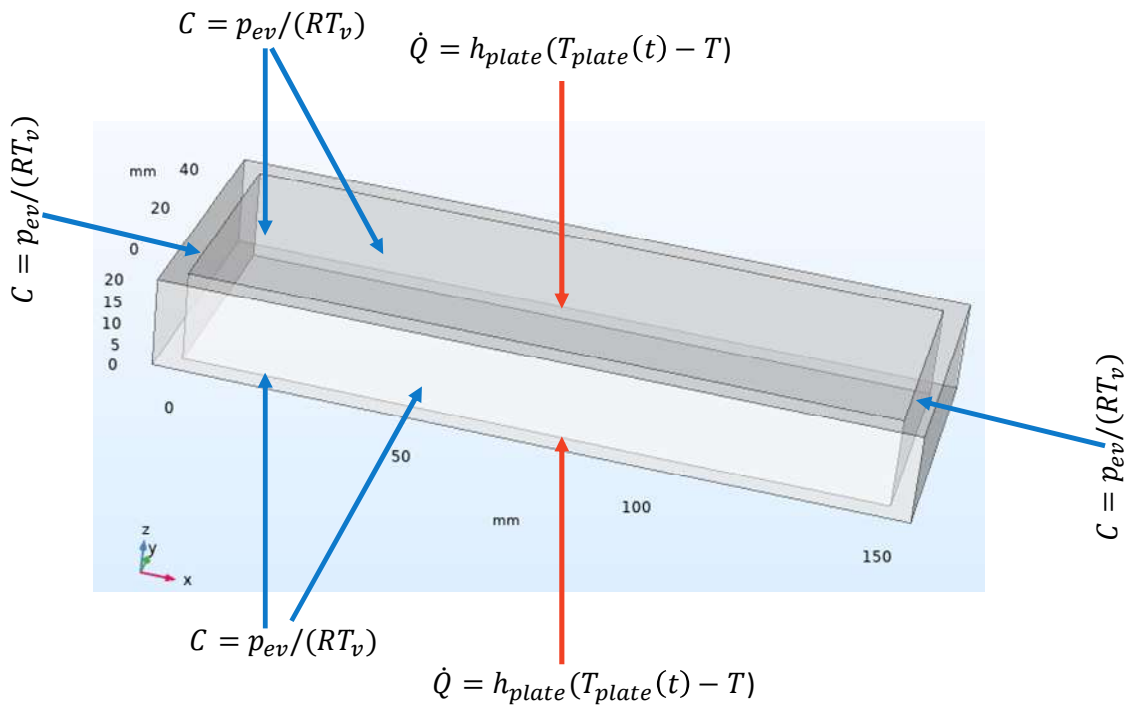


Figure 22: Boundary conditions used in the model of the small-scale adsorber.

3.3.2.4 Model validation

The model was validated using the results of the measurements that will be described in section 3.4. The results in Figure 23 show the evolution of uptake with time in the central point of the sorbent domain for a test at 20°C evaporation and $T_0=65^\circ\text{C}$, $T_{ads}=30^\circ\text{C}$. As is it possible to notice, the fitting in the range of 0.6-0.8, which is the common range used for sizing, is good, thus proving the potentiality of the model for the evaluation of different adsorber configurations.

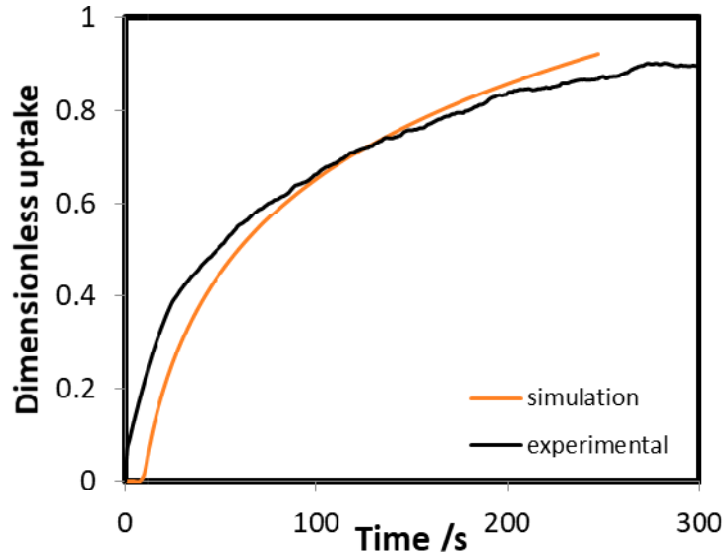


Figure 23: Model validation.

3.3.2.5 Parametric analysis

The model developed was used for the optimization of the adsorber final configuration, in terms of the space between two microchannels. To this aim, gaps between 25 mm and 60 mm were evaluated and the results compared in terms of the time needed to reach 80% of maximum uptake and temperature evolution inside the adsorbent, which represents a measure to evaluate the achievable capacity of the adsorber. The results are shown in Figure 24, where it is possible to notice a clear effect of the channels' space: increasing the height of the porous structure, the kinetics of the system is penalized, both due to the heat and mass transfer increased resistances. This is in agreement with the results on the uncoated foams reported in Figure 13. When a porous structure of 60 mm is considered, the shape of the curve changes, and the time needed to reach 80% of adsorption uptake under the selected conditions passes from 100 s to 300 s. Therefore, a configuration with 20 mm gap between the channels was selected as the optimal one.

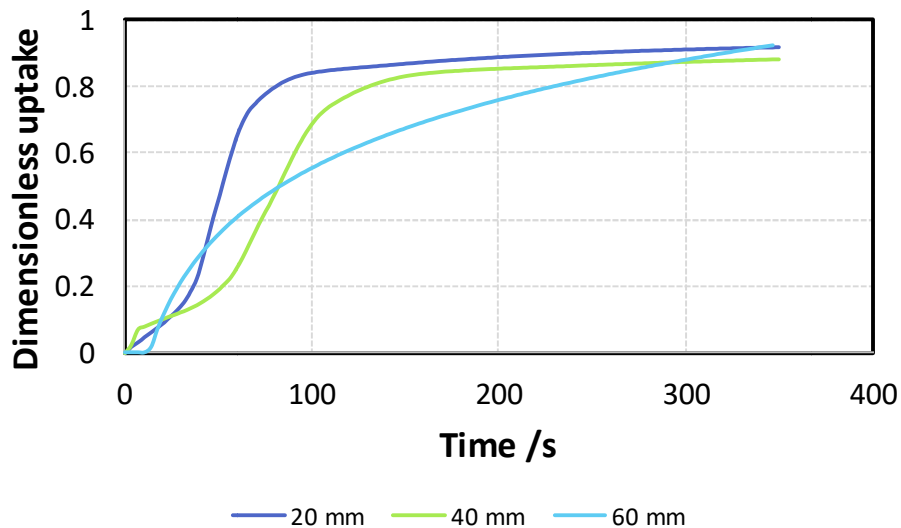


Figure 24: Parametric analysis of the adsorber configuration.

3.4 Experimental evaluation of the adsorber performance

The evaluation of the performance of the developed adsorbers was carried by the use of a testing facility specifically devoted to measure the dynamic performance of representative adsorber configuration under real boundary conditions. The setup employs the well-known “gravimetric version of the Large Temperature Jump method (G-LTJ)” here below described.

3.4.1 Testing apparatus

Aristov et al.[5] firstly developed a new measurement method able to reproduce the isobaric ad-/desorption step typical of an adsorption heat pump/chiller operation driven by a temperature jump/drop. This method, based on an indirect volumetric measurement of the uptake evolution versus time, was called “volumetric version of the Large Temperature Jump method (V-LTJ)”. Later Santamaria et al.[6] modified the method adding a weighing sensor to directly measure the sample mass during isobaric adsorption and desorption stages. This method took the name of gravimetric version of the Large Temperature Jump method (G-LTJ)”.

In the Gravimetric Large Temperature Jump Method (G-LTJ) the evolution of the adsorption/desorption phases are directly followed by measuring the weight of the adsorber by the use of a load cell on which the adsorber is located. This is why it is referred as the gravimetric Large Temperature Jump, indeed, it was employed to test complex small scale adsorber concepts with a remarkable range of masses (5–1000 g) and a wide kind of configurations.

Figure 25 shows the schematic layout of the experimental setup. It mainly consists of two vacuum chambers. The first one is the measuring unit (volume = 12 dm³) in which the Adsorbent – Heat Exchanger (Ad-HEX) is located and connected both to a hydraulic heating/cooling system and to a supporting weighing unit. The latter represents the heart of the entire system. It consists of a load cell able to follow the weight evolution of samples with mass ranging between 5 and 1000 g with the accuracy of 0.1 g and a time response faster than 0.1 s. The measuring chamber is connected, through the automatic valve V5, to the chamber 2 (volume = 6 dm³) which can operate as evaporator or condenser.

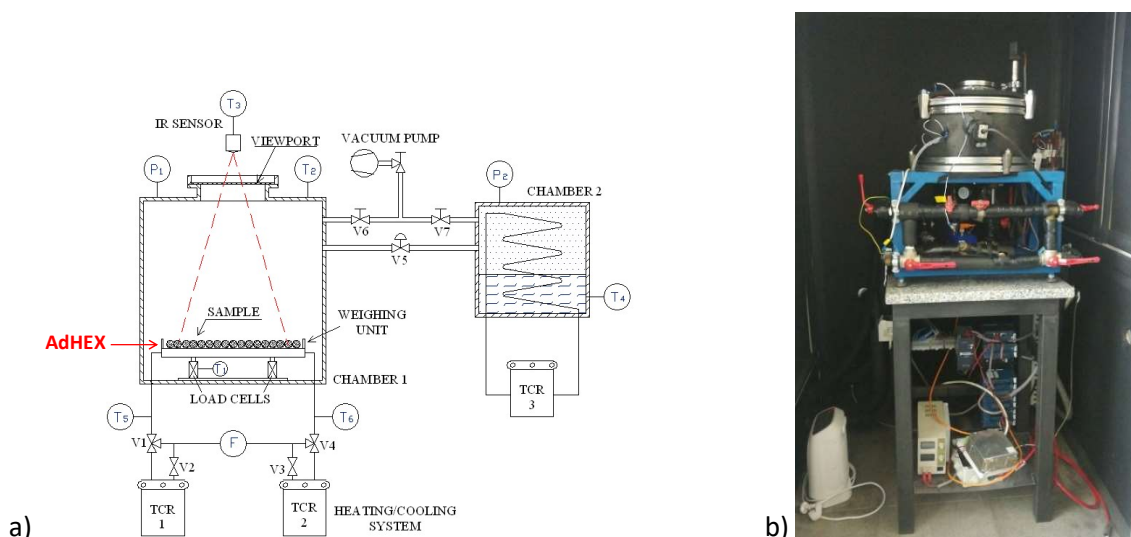


Figure 25: a) Schematic drawing of the experimental setup; b) Overall view of the G-LTJ measurement.

The entire system is realized in stainless steel AISI 316, allowing to operate with different refrigerants (water, methanol, ethanol). Three circulating thermal baths permit to fix and manage an ACH cycle reproducing with high accuracy a wide range of operating conditions. The flow rate, V , of the external heat transfer fluid (water) can be regulated acting on the

pump speed therefore different heating/cooling scenarios can be achieved. Also this component, such as the entire pipeline, is thermally insulated to prevent the heat dissipation to the ambient. All the relevant physical parameters (pressures, temperatures, flow rate) are acquired each 1 s through a dedicated acquisition data system and displayed by a friendly software interface, specifically developed in LABVIEW® environment. It was realized and installed an insulated box to avoid condensation inside the chambers and an external air heater fixed box temperature on the basis of the tested operating conditions. A detailed description of the setup can be found in [5,6].

3.4.2 Testing procedure description

The experimental setup is based on the monitoring of the uptake during a real isobaric step of an adsorptive cycle. Figure 26 depicts a hypothetical thermodynamic cycle (A–B–C–D) working under the following operating conditions: evaporation temperature T_e , condensation temperature T_c , desorption temperature T_H . Numerical values of T_c , T_e and T_H depend on the equilibrium properties of the tested working pair.

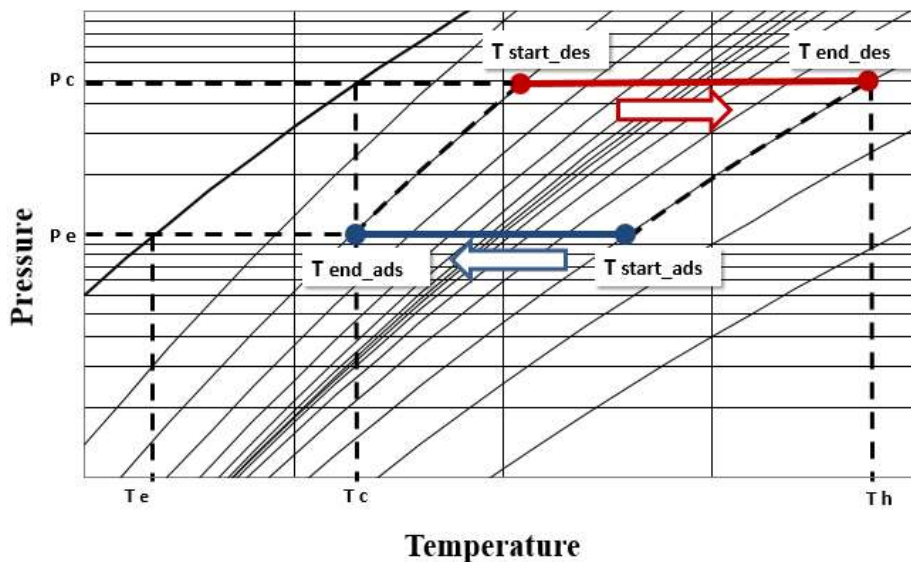


Figure 26: Testing procedure detailed on the isosteric adsorption chart for a generic adsorbent pair.

A standardized procedure is followed in order to guarantee a high reproducibility of the measurements. A typical experimental test consists of two phases. After a preliminary degassing, the adsorbent is led to the initial thermodynamic equilibrium ($T_{\text{start-ads}}$). Secondly, the desorption/adsorption stage is initiated by a fast temperature jump/drop. This causes a variation of the sample weight that directly corresponds to the water de/adsorbed. Tests are carried out under boundary temperatures and pressures defined directly from the thermodynamic cycle of the working pair. The test is considered completed when the new equilibrium point ($T_{\text{end-ads}}$) is achieved and the mass and the adsorber surface temperature remain constant.

3.4.3 Tested adsorber configurations and operating conditions

The tested Ad-HExs (adsorbent material + heat exchanger), produced by Fahrenheit GmbH, are developed by integration of an adsorbent material belonging to the SAPOs family (i.e. SAPO-5) into different HEx configurations. This adsorbent material was synthesized, instead of the foreseen SAPO-34, due to some deviations during the reaction phase inside the Fahrenheit' reactor, caused by the small dimension of the realized HEx. Nevertheless, SAPO-5 has a high

affinity to the SAPO-34, with the main difference related to the regeneration temperature, which is lower for SAPO-5 than for SAPO-34. For this reason, in order to test the adsorber configuration it was decided to stick with this solution, applying a preliminary sizing approach to achieve the final adsorber design.

The HExs are made of aluminium with the following overall dimensions: thickness 40 mm, length 115 mm and the width 190 mm (volume = 0.875 dm³). HExs were realized at AKG by brazing different porous structures on pairs of MPE-tubes in AKG's Controlled Atmosphere Brazing process. The tubes were then connected with header tubes and welded on flanges for connection to the systems at Fahrenheit. There the SAPO was synthesized on the different HEx-structures: finned, foam, chips. Fig. 24 shows one of tested Ad-HExs placed into the measuring chamber.



Figure 27: View of the adsorber installed in the measuring unit.

In order to verify the exact quantity of adsorbent material contained for each HEx, a preliminary equilibrium test was carried out. The sample is heated up to $T_h = 90\text{ °C}$ and evacuated by the use of a vacuum pump for the initial out-gassing phase making the sample almost completely dry ($p < 0.1\text{ mbar}$). Subsequently, on the basis of isotherms for SAPO-5 calculated by Fahrenheit, the adsorbent is led to the initial thermodynamic equilibrium at Point 1 corresponding to $T_{ads} = 20\text{ °C}$ and $P_{sat} = 10.2\text{ mbar}$ (7 °C) conditions as shown in Figure 28. The expected water content, corresponding to about 19%, is then used to calculate the adsorbent dry mass.

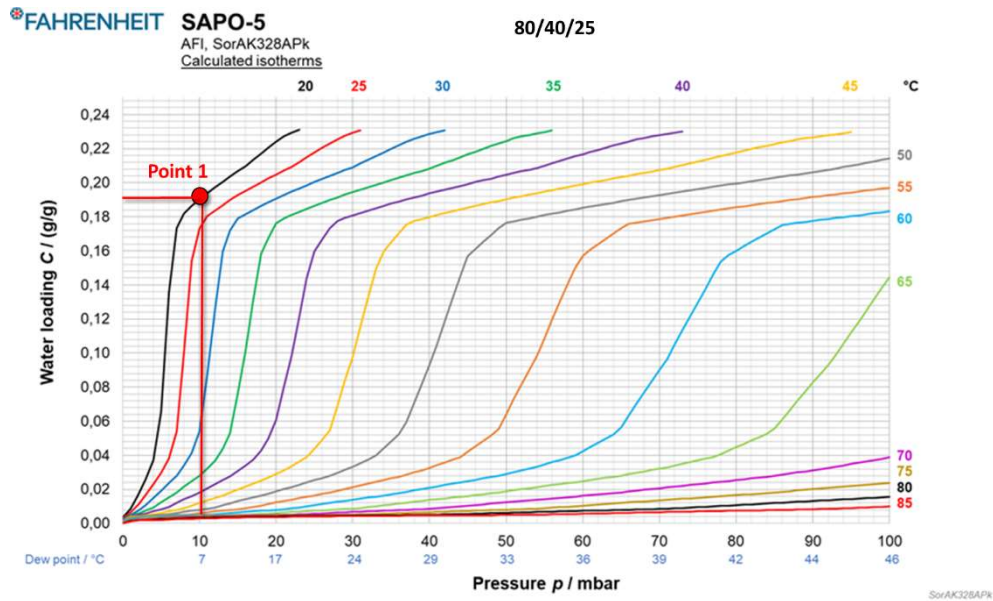


Figure 28: Calculated isotherms for SAPO-5 and equilibrium point for $T_{ads} = 20^{\circ}\text{C}$ $T_{ev} = 7^{\circ}\text{C}$ conditions.

The Ad-Hex configurations developed and tested are listed in Table 2. The two foam samples were provided by MIKR and AKG and subsequently pressed and coated by FAHR. They are realised with 99.5 pure Al alloy and had a starting pore density of 20 ppi (after pressing).

Table 2: List and main features of Ad-HEx configurations.

		CHIPS (AKG #M1192F)	
			Adsorbent material dry mass [g]
	HEx metal mass [g]	426	
	Water Content inside the Hex (mL)	150	
	Ratio between the dry adsorbent mass m and the total metal mass M m/M [g/g]	0.155	
		FINS (AKG #M1193F)	
			Adsorbent material dry mass [g]
	HEx metal mass [g]	405	
	Water Content inside the Hex (mL)	150	
	Ratio between the dry adsorbent mass m and the total metal mass M m/M [g/g]	0.153	
		FOAM #1 (AKG #M1183F)	

	Adsorbent material dry mass [g]	86
	HEx metal mass [g]	332
	Water Content inside the Hex (mL)	150
	Ratio between the dry adsorbent mass m and the total metal mass M m/M [g/g]	0.26
FOAM #2 (AKG #M1184F)		
	Adsorbent material dry mass [g]	45
	HEx metal mass [g]	332
	Water Content inside the Hex (mL)	150
	Ratio between the dry adsorbent mass m and the total metal mass M m/M [g/g]	0.135

The experimental activity was carried out under test conditions of interest for the specific applications and reported in Table 3. The isotherm diagram shown in Figure 28 allows to identify the adsorption/desorption step to be reproduced under the operating conditions defined by heating temperature T_h , condensation temperature T_c , evaporation temperature T_e .

Table 3: List of operating conditions.

Test condition ($T_h/T_c/T_e$)	Type	T drop/jump	T_e (P_e)	Delta Uptake [wt.%]
80°C/30°C/20°C	adsorption	68-30 °C	20 °C (23.3 mbar)	19%
	desorption	39-80 °C	30 °C (42.3 mbar)	19%
80°C/35°C/20°C	adsorption	65-35 °C	20 °C (23.3 mbar)	18%
	desorption	50-80 °C	35 °C (56.0 mbar)	18%
80°C/40°C/20°C	adsorption	60-40 °C	20 °C (23.3 mbar)	12%
	desorption	59-80 °C	40 °C (73.5 mbar)	12%

3.4.4 Results: typical test detailed analysis

Here below a typical test is described in details. Results refer to the finned Ad-HEx tested under the operating conditions 80/30/20, corresponding to the drop 68-30°C with $T_e = 20^\circ\text{C}$ and water flow rate $V_{\text{adsorber}} = 3$ l/min and $V_{\text{evap}} = 10$ l/min.

Figure 29 shows the Ad-HEx mass evolution versus time during the adsorption step. The registered noise, with fluctuations around the mean value, represents an inevitable consequence of the Ad-HEx oscillation under the hydrodynamic stress. To improve the quality

of the analysis the signal was post-processed, by the smoothing function, to replicate closely the real value as reported in Figure 29.

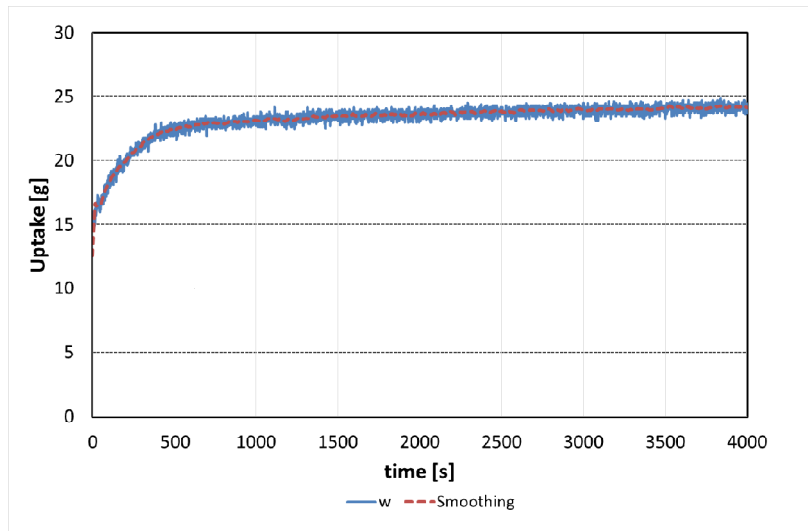


Figure 29: Evolution of the water uptake with its smoothing approximation during adsorption step 68-30 °C T_e , 20°C, $V_{adsorber} = 3$ l/min

Figure 30 shows the dimensionless uptake $w(t)/w_\infty$ evolution. The complete conversion is reached in about 3700 s while the time needed to reach the 90%/80%/63% of conversion is respectively 982 s, 365 s and 200 s.

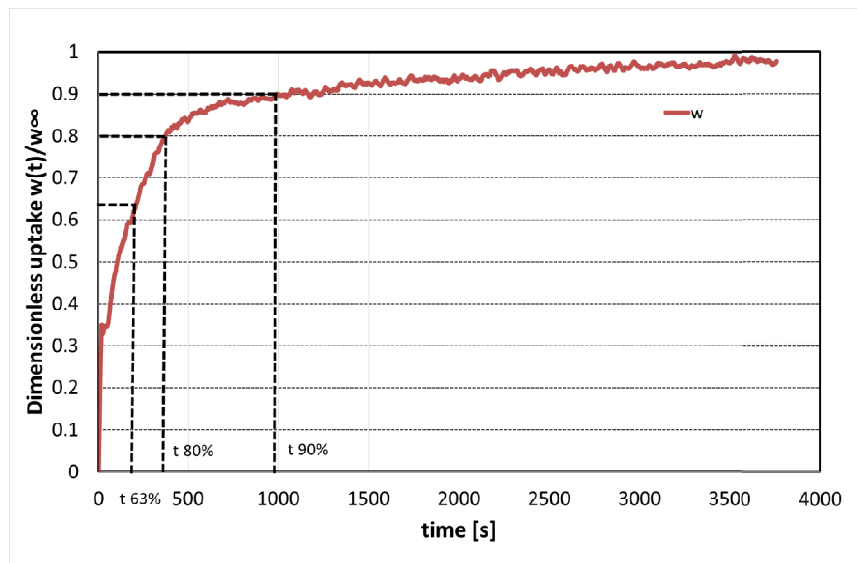


Figure 30: Dimensionless uptake curve during adsorption step 68-30 °C T_e 20°C, $V_{adsorber} = 3$ l/min

Typical time evolutions of inlet-outlet temperatures during the adsorption step as well as of the power exchanged with the heat transfer fluids (both for the evaporator and the adsorber) are reported in Figure 31 and Figure 32. In the first 20 s the exchanged power reaches 3.2 kW due to the high rate of adsorption in the early seconds and the power required to cool down the metal parts of the HEx.

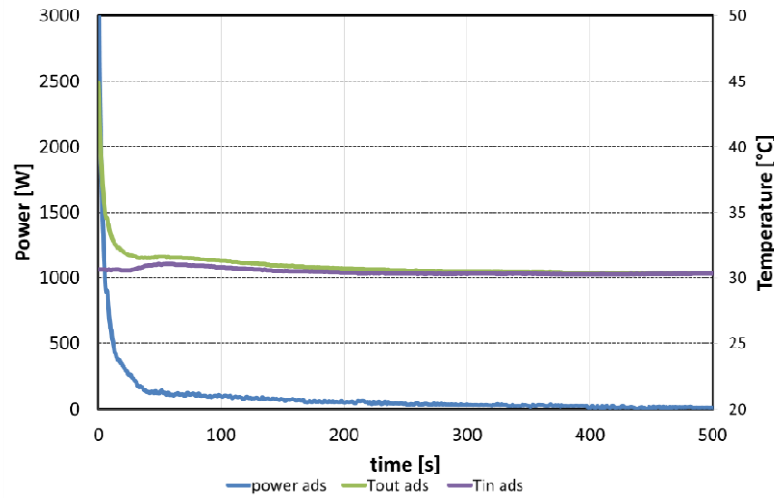


Figure 31: Evolution of the thermal power, inlet and outlet temperatures in the adsorber during adsorption step 68-30 °C T_e 20°C, $V_{adsorber} = 3$ l/min

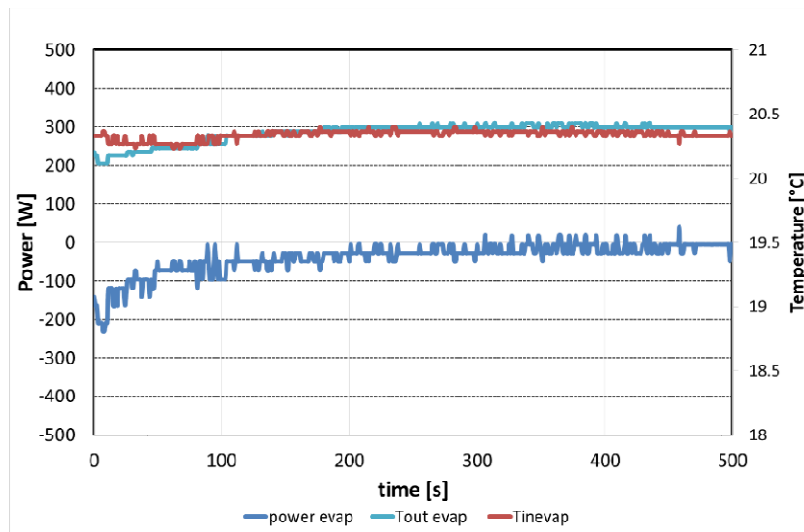


Figure 32: Evolution of the Power, inlet and outlet temperatures in the evaporator during adsorption step 68-30 °C T_{ev} 20°C, $V_{evap} = 10$ l/min

The cooling power delivered in the evaporator has a peak of 200 W while after about 300 s is close to zero since 80% of conversion is already completed.

In order to evaluate the performance of the tested adsorber, the Specific Cooling Power (SCP), which represents the average cooling power delivered per unit of mass, was calculated according to the following equation:

$$SCP(t) = \frac{\Delta w_{\infty} \cdot q_e \cdot Conv\%}{t_{\%}}$$

Where, Δw_{∞} [g/g] is the maximum uptake exchange in the tested conditions, ΔH_{ev} [J/g] is the latent heat of evaporation of liquid water at 20 °C, 2319 J/g, Conv% is the degree of conversion at which the SCP is calculated, $t_{\%}$ [s] is the time needed to reach the selected degree of conversion. In Table 4 an example of the performed calculations is reported.

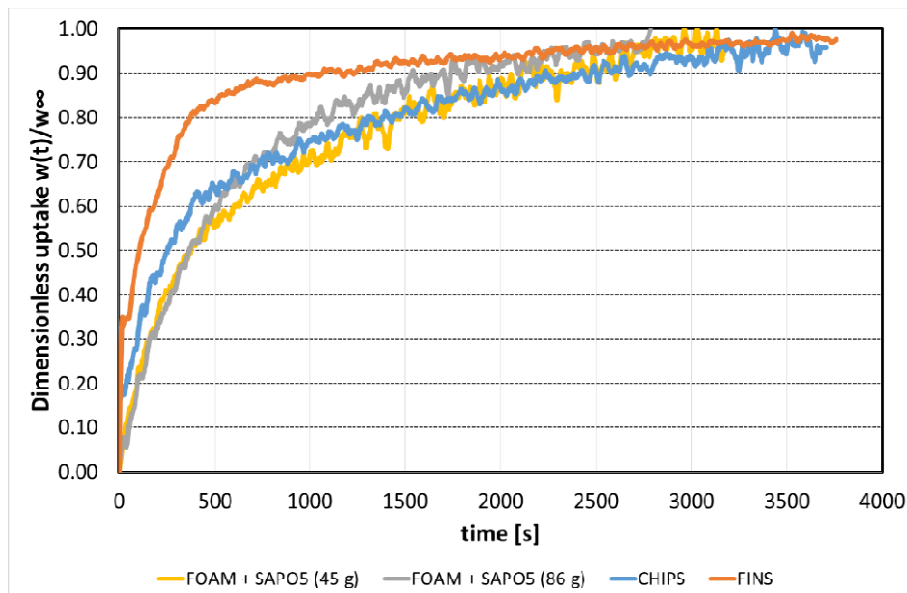
Table 4: Test results for finned Hex during adsorption step 68-30 °C T_{ev} 20°C.

	$t_{90\%}$	$t_{80\%}$	$t_{63\%}$	$\Delta W \%$	$\Delta W \text{ kg}$	$SCP_{90\%}$	$SCP_{80\%}$	$SCP_{63\%}$
Test 1	982	365	200	19%	0.012	0.40	0.97	1.39

3.4.5 Results: Comparison of different adsorber configurations

The comparison of different adsorber configurations was carried out for 80/30/20 °C boundary conditions. Under this condition, the adsorption step corresponds to the drop 68-30°C with $T_{ev} = 20^\circ\text{C}$. The expected Δw is 19%.

Figure 33 displays the adsorption kinetic curves as the water dimensionless uptake versus time under the tested conditions. In particular, data demonstrated that the finned HEx is able to produce a maximum specific cooling power for the adsorption step 68-30 at T_e 20°C of $SCP_{63\%} = 1.39 \text{ kW kg}^{-1}$ and lowest values of $t_{63\%} = 200 \text{ s}$, $t_{80\%} = 365 \text{ s}$, $t_{90\%} = 982 \text{ s}$ were found. For other HEx configurations, higher values of $t_{63\%}$, $t_{80\%}$, $t_{90\%}$ and lower SCP were obtained. Results show that the finned Ad-Hex is, from the dynamic point of view, the fastest configuration. This is most probably due to the better heat transfer efficiency coupled to the limited aluminum mass, which also keeps the thermal inertia of the whole HEx low.


Figure 33: Comparison between HEx's dimensionless uptake curve during adsorption step 68-30 °C T_{ev} 20°C, $V_{ads} = 3 \text{ l/min}$

A detailed list of performed test for each HEx is reported in Table 5.

Table 5: Test results for different Ad-HEx configurations.

	$t_{90\%}$	$t_{80\%}$	$t_{63\%}$	$\Delta W \%$	$\Delta W \text{ kg}$	$SCP_{90\%}$	$SCP_{80\%}$	$SCP_{63\%}$
FINS								
Test 1	982	365	200	19%	0.012	0.40	0.97	1.39
Test 2	684	324	155	19%	0.014	0.59	1.10	1.82
FOAM #1								
Test 1	1690	1037	535	19%	0.016	0.23	0.33	0.51

Test 2	1713	1007	583	19%	0.0156	0.227	0.33	0.45
FOAM #2								
Test 1	2103	1432	691	19%	0.0085	0.19	0.25	0.40
Test 2	1574	1056	540	19%	0.0086	0.25	0.33	0.52
CHIPS								
Test 1	2350	1375	450	19%	0.0128	0.17	0.26	0.63
Test 2	2225	1301	588	19%	0.0128	0.17	0.26	0.47

3.4.5.1 Detailed analysis of best performing adsorber: finned Hex

On the basis of the comparison, it was found that finned HEx was the best performing configuration. In particular, data demonstrated that the specific configuration is able to produce a maximum specific cooling power for the adsorption step 68-30 at T_{ev} 20°C of $SCP_{63\%} = 1.39 \text{ kW kg}^{-1}$ and lowest values of $t_{63\%} = 200 \text{ s}$, $t_{80\%} = 365 \text{ s}$ were found. For other adsorption runs, there is a performance reduction and worst values of $t_{63\%} = 762 \text{ s}$, $t_{80\%} = 520 \text{ s}$, $t_{90\%} = 786 \text{ s}$ and lowest SCP were obtained for the adsorption step 60-40 at T_{ev} 20°C. A detailed list of performed test for each cycle conditions is reported in Table 6.

Table 6: Detailed tests results of finned HEx.

	$t_{90\%}$	$t_{80\%}$	$t_{63\%}$	$\Delta W \%$	$\Delta W \text{ kg}$	$SCP_{90\%}$	$SCP_{80\%}$	$SCP_{63\%}$
Ads 68-30 T_{ev} 20								
Test 1	982	365	200	19%	0.012	0.40	0.97	1.39
Test 2	684	324	155	19%	0.014	0.59	1.10	1.82
Ads 65-35 T_{ev} 20								
Test 1	858	487	276	18%	0.013	0.44	0.69	0.96
Test 2	786	520	289	18%	0.013	0.48	0.64	0.91
Ads 60-40 T_{ev} 20								
Test 1	2241	1445	762	12%	0.009	0.11	0.16	0.23
Test 2	1727	1104	652	12%	0.009	0.15	0.20	0.27

3.5 Adsorber sizing

In order to size the adsorber, the experimental outcomes presented in the previous section were used. The sizing process for the adsorber is shown schematically in Figure 34:

1. At first, the cooling power needed is estimated, by considering that it is equal to the condensation power expected from Daikin compression chiller, i.e. 19 kW under nominal conditions.
2. From the tests in the G-LTJ setup, the specific cooling power available for each structure is calculated. A scaling factor of 0.8 is considered, i.e. the maximum uptake available is taken equal to 0.8 of the maximum Δw measured, to take into account the fact that the kinetic of the process in the range 80%-100% of the uptake is slow and therefore it is more convenient to stop the process at the 80% [7].

3. The cooling power is further scaled by a safety factor γ , considered equal to 3.
4. The density of sorbent on each porous structure is calculated as the ratio between the mass of coating on each structure and the volume of the porous structure itself;
5. The mass and volume of adsorber needed are finally calculated considering the cooling demand and the specific cooling power (per kg or m³) that each structure can deliver.

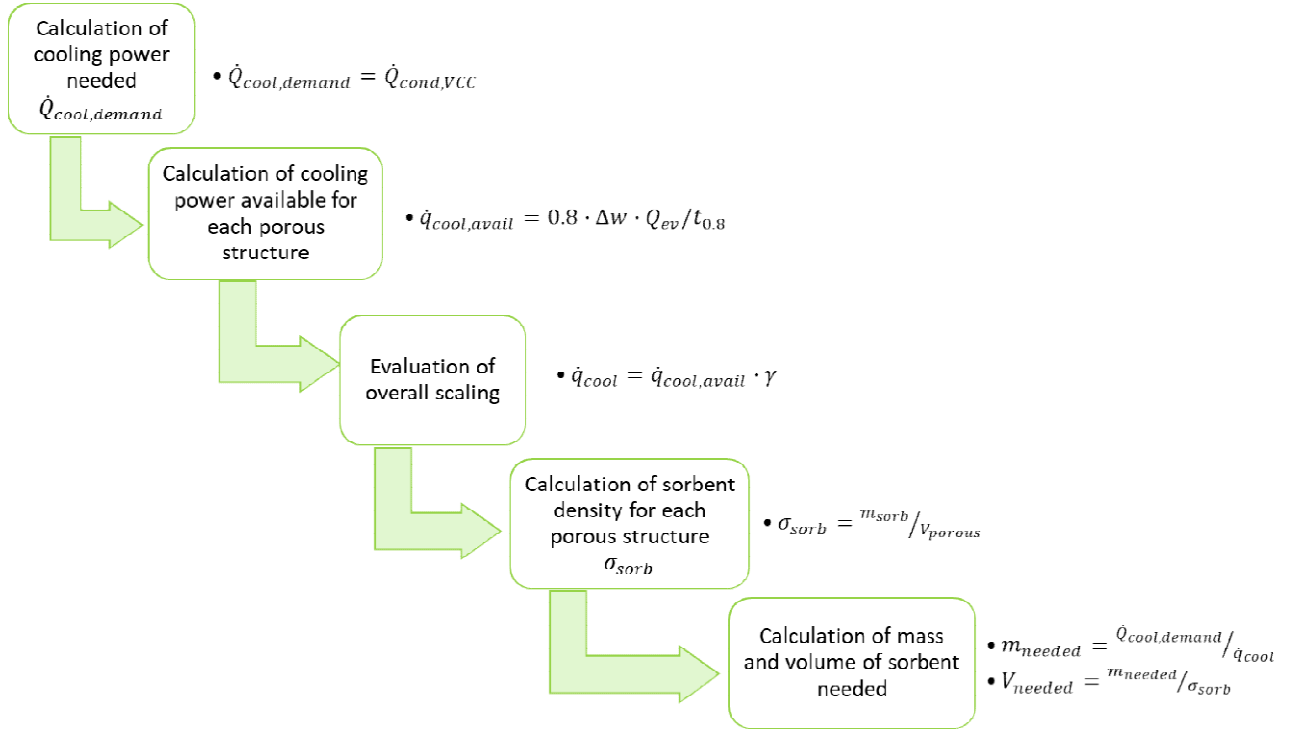


Figure 34: Sizing process for the adsorber.

The results are shown in Table 7. As it is clear, the best performing structures are the pressed fins, that allow reaching a specific cooling power of 1.1 kW/kg_{sorbent} while the structure realised with wastes from aluminium has a very slow kinetic, which results in a low cooling power. The two foams tested show quite a different behaviour, which is due to problems in the height tolerances of the Foam#1 structure, which do not allow the proper brazing on the heat exchanger and therefore a poor heat transfer from the HTF to the sorbent.

Table 7: Results of the sizing of the adsorber.

Structure	\dot{q}_{cool} [kW/kg]	m_{needed} [kg]	V_{needed} [m ³]
Pressed fins	1.1	40	0.5
Foam #1	0.4	100	1.0
Foam #2	0.8	54	0.7
Chips	0.3	130	1.6

Such values were further refined based on the tests from Fahrenheit on medium-scale HEXs. The final sizing of the adsorber is described more in detail in section 3.6.

3.6 Full-scale adsorber design and manufacturing

As described in chapter 3.4.3 multiple versions of small adsorbers with different structures (see Table 2) were manufactured for evaluation of their adsorption performance. Since the sample with fins showed the best performance it was decided to build the full-scale adsorber with fins. Moreover, the insufficient flatness of the foam strips did not allow manufacturing adsorbers with foam structures in the required sizes.

Since AKG does not have the tooling to manufacture the desired fins with high density directly, the existing louvered AKG-fin 18 (Figure 35) was used as basis to produce a fin with the required density. For that purpose, a long piece of fin was compressed to a short compact part that could be used to build the adsorber. For the first adsorbers fin strips of 375mm length were compressed to 135mm length resulting in a fin pitch of 1.8mm (Figure 36).

A special gauge (Figure 37) was manufactured to check the length of the compressed fins and to calibrate their height to the desired 11.5mm. This is needed to guarantee a reproducible fin density for the whole adsorber and a perfect flatness of the fins for high quality braze joints in the adsorber.

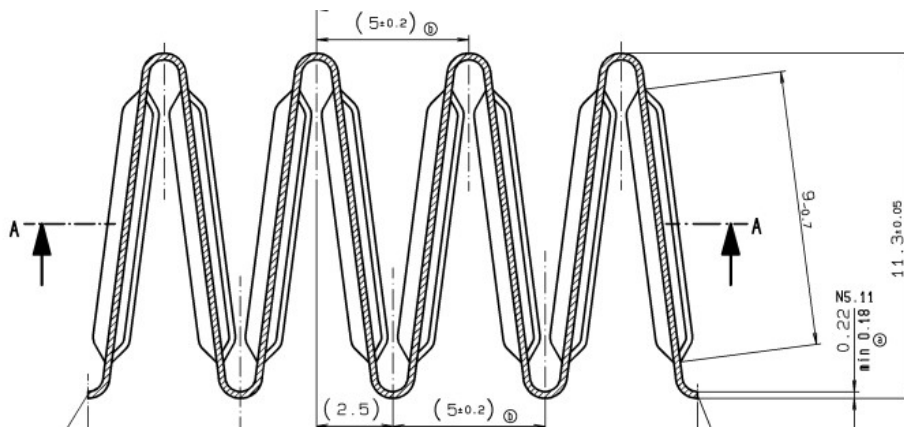


Figure 35: Fin 18, with 5mm nominal fin pitch

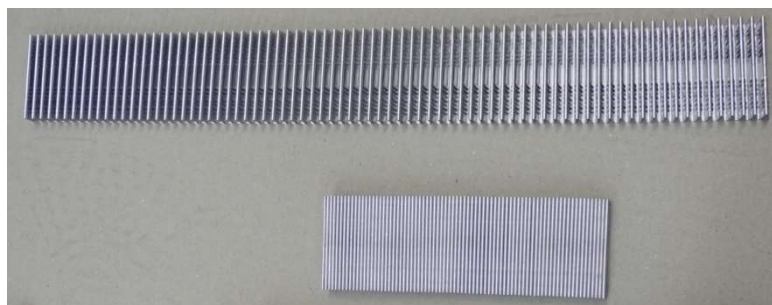


Figure 36: Fin compressed from 375mm to 135mm, fin pitch: 1.8mm, height: 11.5mm



Figure 37: Gauge for checking and calibrating the compressed fins

For first internal performance tests Fahrenheit requested a medium-size adsorber to fit in their test equipment. This was manufactured prior to manufacturing the full-size adsorber for the demo sites. The medium-size adsorber consists of 22 flat aluminium tubes (45mm wide, 4.3mm high, 550mm long) filled with offset turbulator structures (Figure 38). The adsorber operates in U-flow to have the water inlet and outlet on the same side. The tubes were assembled between two header plates (Figure 39).

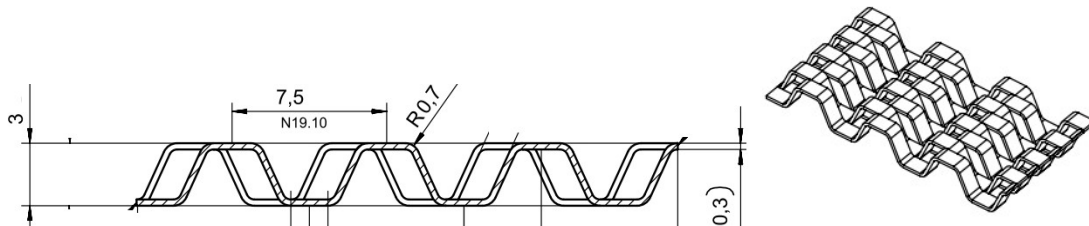


Figure 38: Turbulator 42 used inside adsorber tubes

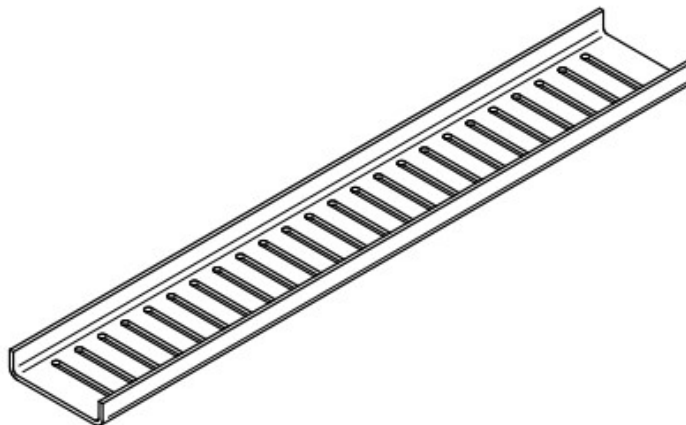


Figure 39: Header plates for adsorber tubes

The complete medium-size adsorber is shown in Figure 40 and Figure 41. The adsorber was brazed in AKG's standard Controlled Atmosphere Brazing process (CAB) at about 600°C. After welding of the header tanks as well as inlet and outlet tubes the adsorber was successfully pressure checked at 9 bar overpressure under water.

The medium-size adsorber was shipped to Fahrenheit in July 2019 for coating with zeolite.

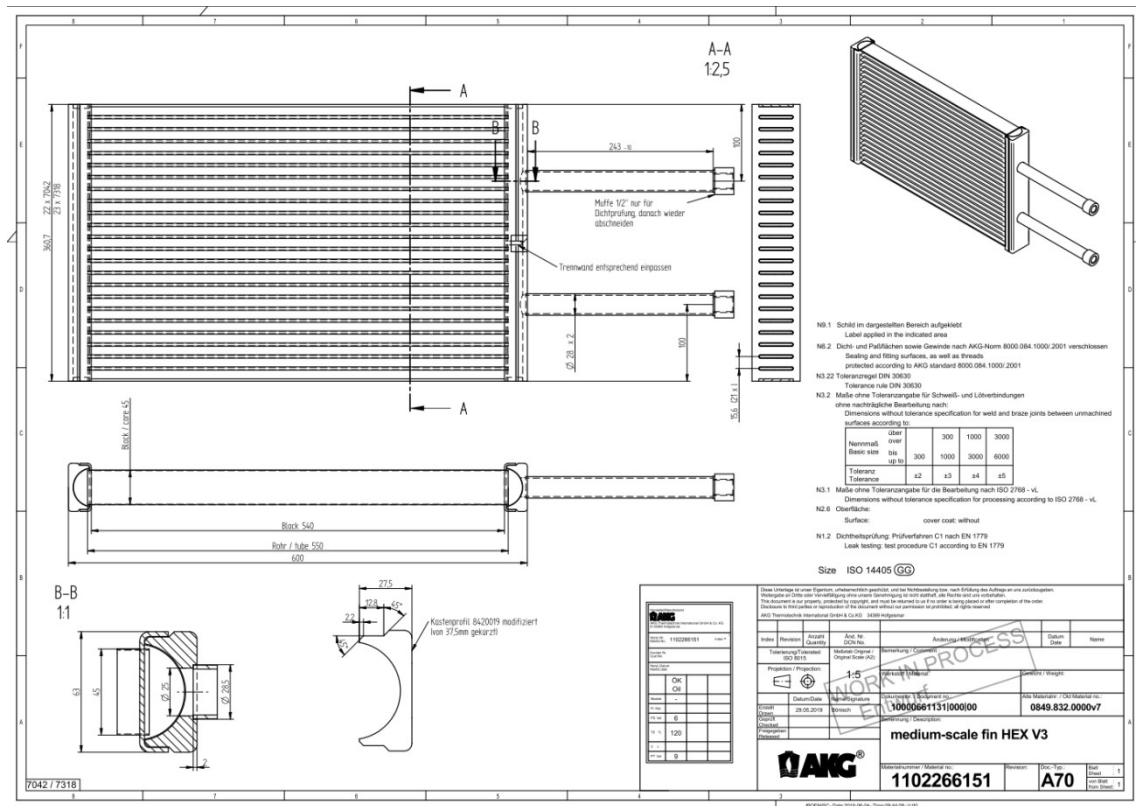


Figure 40: Drawing of medium-size adsorber (NP: 4013590)



Figure 41: Photo of medium-size adsorber (NP: 4013590)

The full-scale adsorber is composed from similar components like the medium-size adsorber but holds 45 tubes, which are now 600mm long (Figure 42). This is the maximum size to be handled in the coating reactor at Fahrenheit. Since one adsorber has a fin space area of around 33m² two of those adsorbers will be combined in one module (Figure 43). This allows to achieve the required minimum of 50m² fin space area needed to generate a zeolite mass between 11 to 13 kg. This provides enough buffer to provide the necessary cooling capacity for Daikin’s chiller. Another advantage is that standard components can be used to build up the module.

A total of six adsorbers will be manufactured by AKG to allow Fahrenheit to optimise their coating process without fear of missing components. To make production more efficient large manufacturing aids to compress and calibrate the fins will be manufactured. Delivery of the parts to Fahrenheit is scheduled for September 2019.

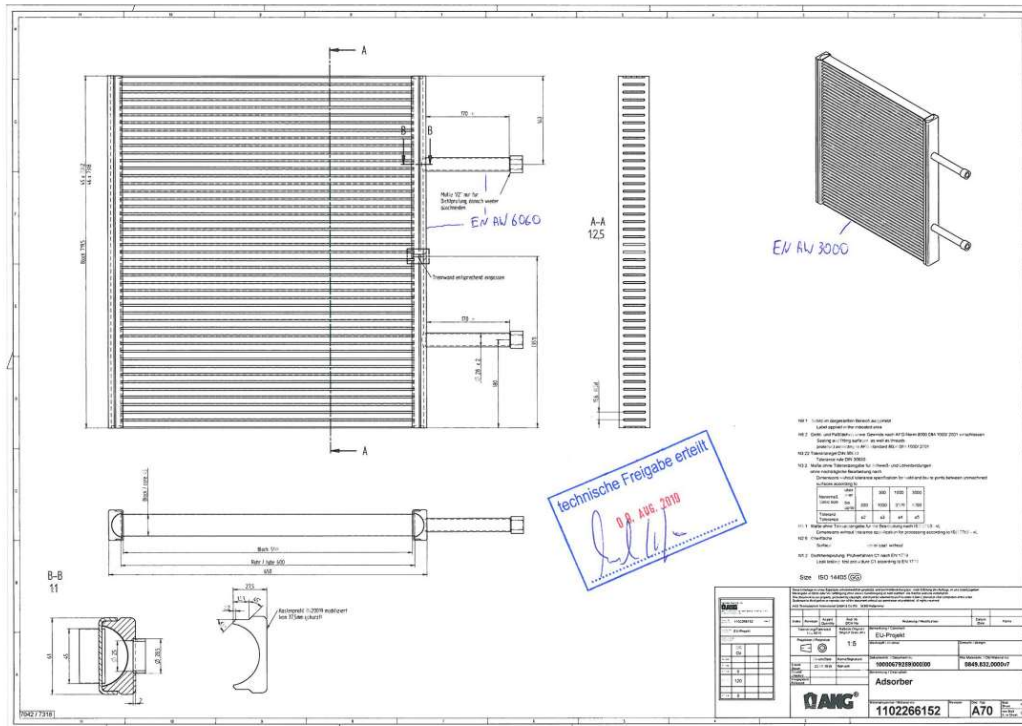


Figure 42: Drawing of full-size adsorber (NP: 4013952, 4013780)

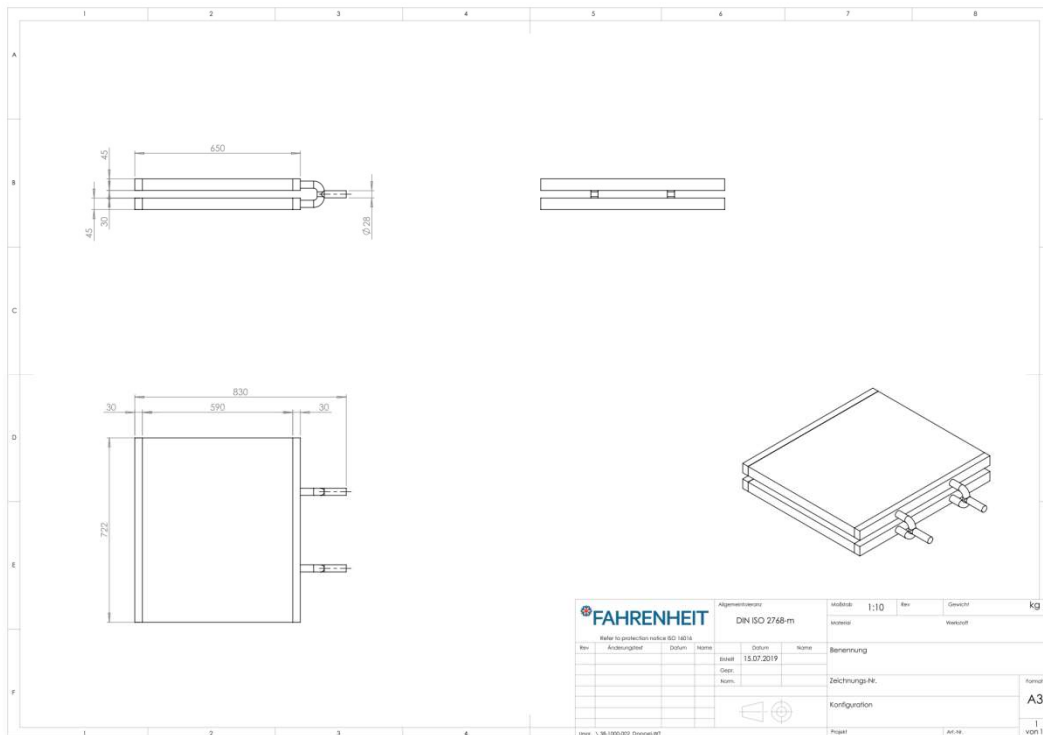


Figure 43: Drawing combination of two adsorbers to one adsorber module

4 Design and manufacturing of the evaporator/condenser

4.1 Lab-scale aluminium HEXs

For the discussion about possible designs of the evaporator/condenser AKG prepared a demonstrator heat exchanger combining densely compressed louvered fins and MPE-tubes (Figure 44).

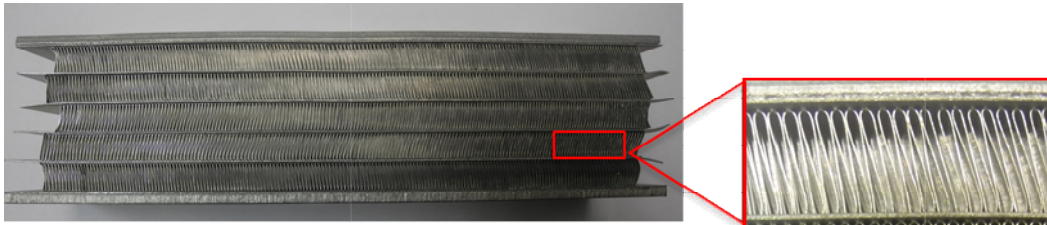


Figure 44: Evaporator demonstrator with dense fins and MPE-tubes

In summer 2018 the sample evaporator to be tested by CNR/ITAE was specified in detail. It was agreed to build it with the densest fin from AKG's portfolio: fin 82 (Figure 45). The maximum dimensions were limited by the size of the test chamber. The design chosen was a bar and plate design with fins and braze sheets were stacked as shown in the core drawing in Figure 46. The core size is 200mm x 272mm with 20 fluid passages of 45mm depth. To avoid flux residues on the surfaces the core was brazed in a vacuum furnace.

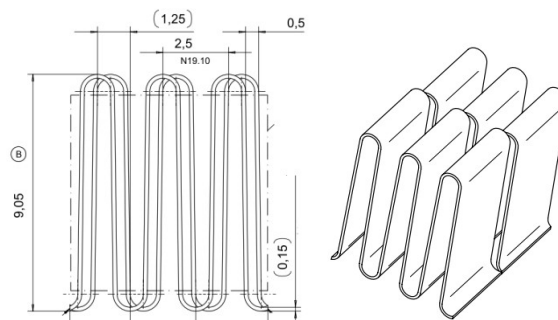


Figure 45: Offset-fin 82, with 2.5mm fin pitch and 9.05mm height

The evaporator was then completed by welding inlet and outlet tanks as well as the connecting pipes to the brazed core as shown in Figure 47. A photo of the finished evaporator before shipping is shown in Figure 48.

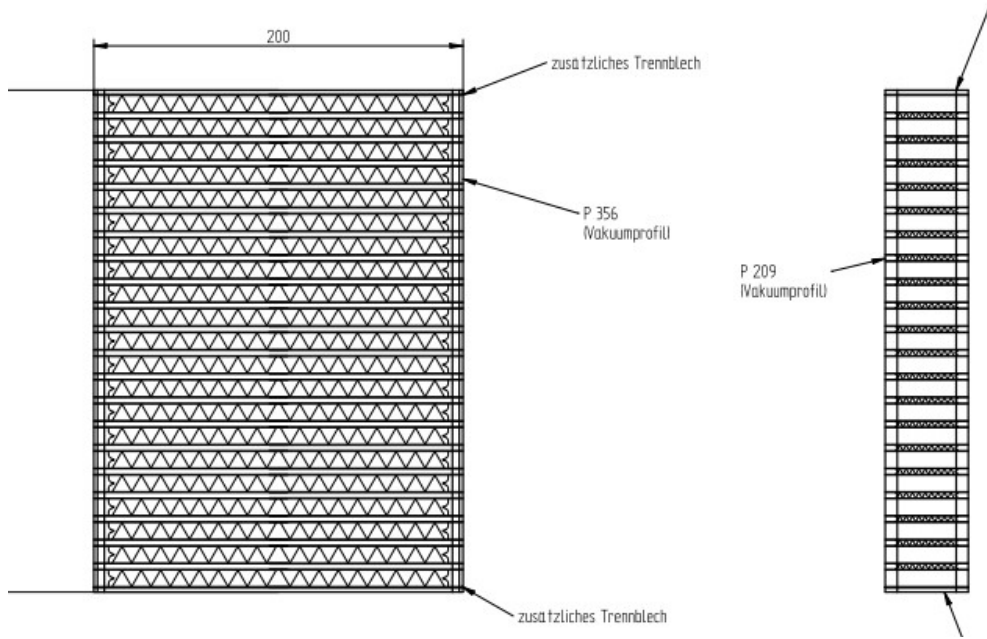


Figure 46: Drawing of the evaporator core

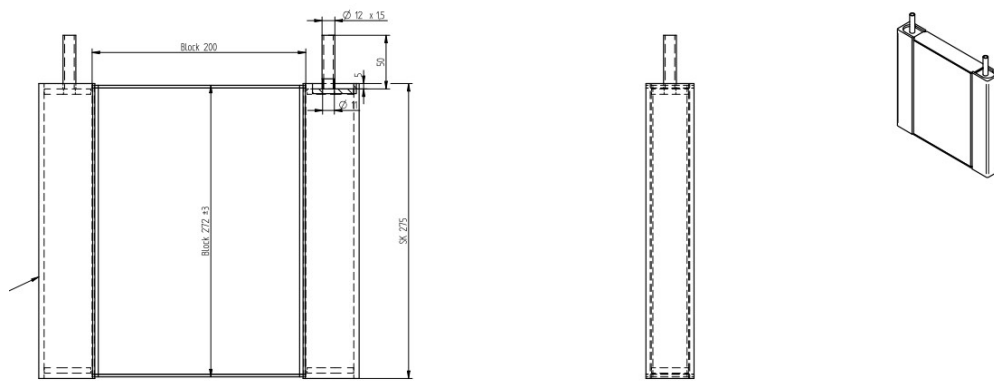


Figure 47: Drawing of the evaporator



Figure 48: Photo of the evaporator (NP 4011915)

4.2 Lab-scale HEXs testing

4.2.1 Testing facilities

The small-scale prototype of evaporator was tested in a testing rig specifically designed and built within T2.1 activity and suitable for the complete characterization of evaporators and condensers under sub-atmospheric conditions.

A schematic layout of the testing rig is shown in Figure 49, whereas Figure 50 presents a rendering of the designed system. The testing rig mainly consists of two vacuum chambers, the condenser (1 in Figure 49) and the evaporator (2 in Figure 49), connected by means of two electrically-actuated pneumatic vacuum valves. In addition, a vacuum pipe with a manual valve allows the flow of the liquid from the condenser to the evaporator, in order to control the level inside the latter component. The temperature level inside the condenser is controlled by means of an aluminium fin-and-tube heat exchanger (4), whereas the temperature level of the pool of the evaporator is controlled by means of a spiral finned coil copper heat exchanger (5). A vacuum circuit is used to keep the pressure at the desired level. The chamber of the evaporator is equipped with two quartz viewports, for visual inspection.

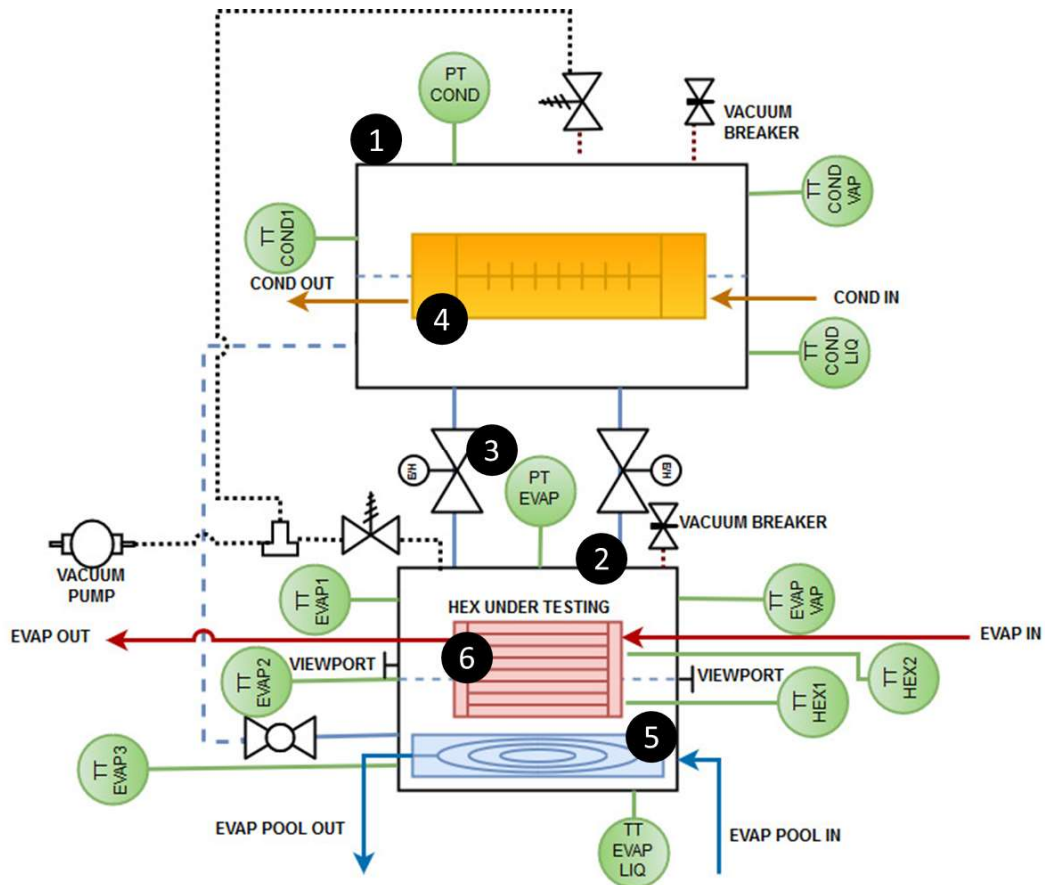


Figure 49: Schematic of the testing rig for the characterization of evaporators under sub-atmospheric conditions at CNR ITAE.

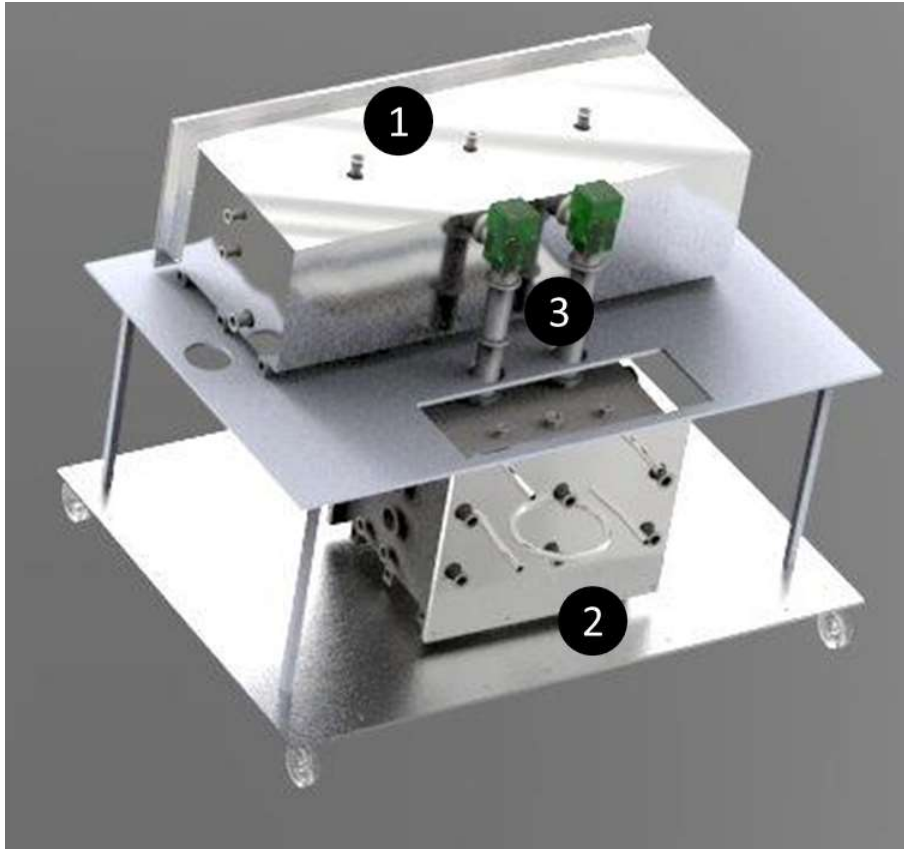


Figure 50: Rendering of the testing rig for the characterization of evaporators at CNR ITAE.

The testing rig was connected to the lab facilities of CNR ITAE, in order to have the desired temperature levels. In particular, the water inside two tanks, a 1.5 m³ hot storage connected to an electric heater and a 1 m³ storage connected to an air-cooled chiller are mixed by means of motorised valves.

Some pictures of the testing rig in the lab of CNR ITAE are shown in Figure 51.



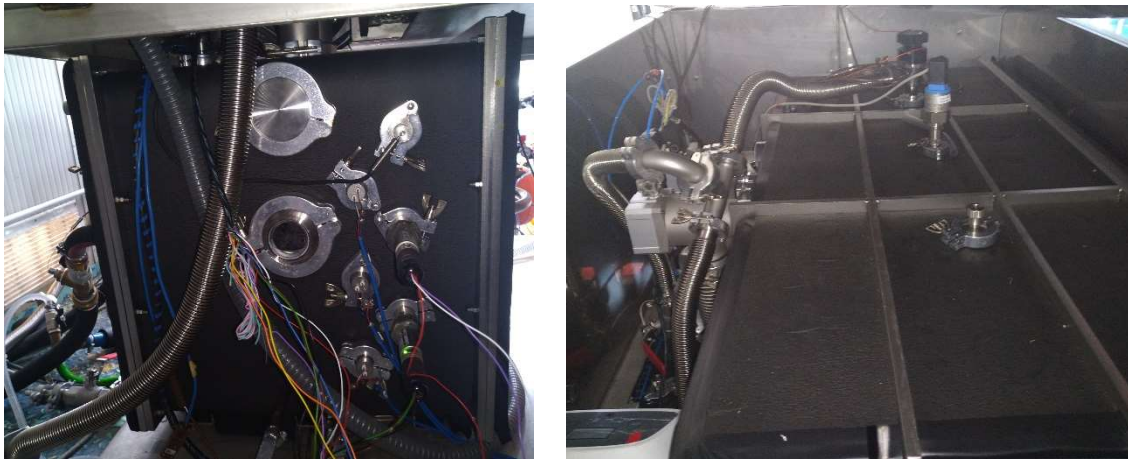


Figure 51: The testing rig for the characterization of evaporators under sub-atmospheric conditions in the lab of CNR ITAE.

The sensors installed are also shown in Figure 49 and are listed in the following Table 8.

Table 8: List of sensors in the testing rig for evaporators and their accuracy.

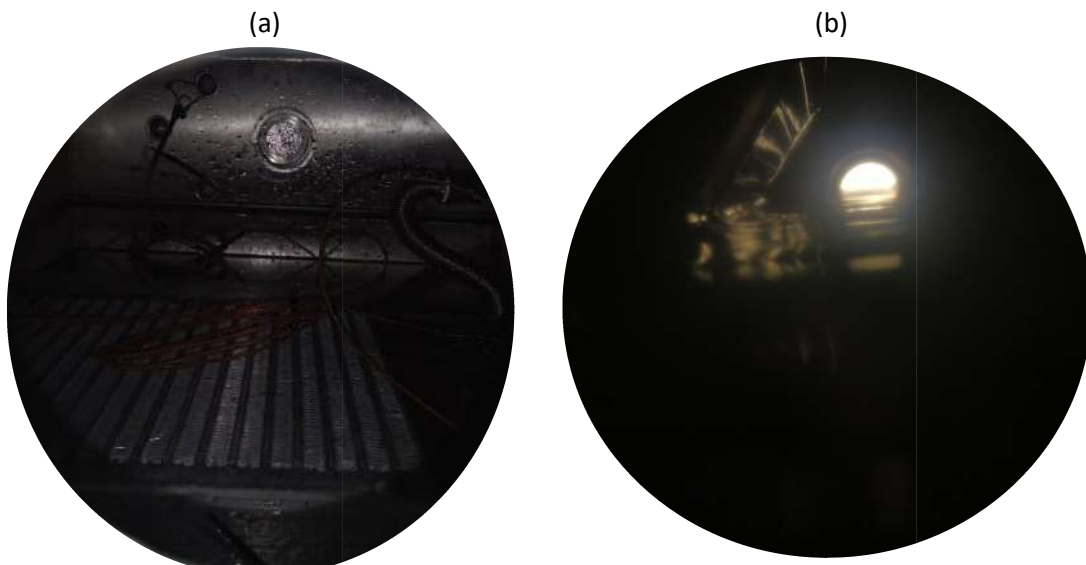
Sensor name	Type of sensor	Parameter measured	Accuracy
PT evap	Piezoelectric pressure sensor	Pressure inside the evaporator chamber	0.25% of reading
PT cond	Piezoelectric pressure sensor	Pressure inside the condenser chamber	0.25% of reading
TT cond vap	Pt100	Temperature of vapour inside the condenser	$\pm 0.1^{\circ}\text{C}$
TT cond liq	Pt100	Temperature of liquid inside the condenser	$\pm 0.1^{\circ}\text{C}$
TT evap vap	Pt100	Temperature of vapour inside the evaporator	$\pm 0.1^{\circ}\text{C}$
TT evap liq	Pt100	Temperature of liquid inside the evaporator	$\pm 0.1^{\circ}\text{C}$
TT cond 1	Type T thermocouple	Temperature of liquid inside the condenser at half height	$\pm 0.3^{\circ}\text{C}$
TT evap 1	Type T thermocouple	Temperature of liquid inside the evaporator at the top of heat exchanger	$\pm 0.3^{\circ}\text{C}$
TT evap 2	Type T thermocouple	Temperature of liquid inside the evaporator in the middle of heat exchanger	$\pm 0.3^{\circ}\text{C}$
TT evap 3	Type T thermocouple	Temperature of liquid inside the evaporator at the bottom of heat exchanger	$\pm 0.3^{\circ}\text{C}$
TT HEX 1	Type T	Temperature of the metal fins of the	$\pm 0.3^{\circ}\text{C}$

	thermocouple	heat exchanger	
FR cond	Magnetic flow meter	Flow rate of the HTF in the condenser	±2% full scale (250 kg/min)
FR evap	Magnetic flow meter	Flow rate of the HTF in the evaporator	±2% full scale (250 kg/min)
FR evap pool	Magnetic flow meter	Flow rate of the HTF in the copper coil for the pool of the evaporator	±2% full scale (100 kg/min)

4.2.2 Configurations tested

Different configurations were evaluated to define the best arrangement for the system. The configurations tested differ in two features: the placement of the heat exchanger, i.e. inclination of 0°, 45° and 90°, and the level of water, i.e. from the heat exchanger completely submerged (or immersed until 60% of the height in the case of the 45° arrangement) until the level is below the height of the heat exchanger.

A particular of the heat exchanger, as installed in 0°, 45° configuration and 90° configurations, is shown in Figure 52.



(c)



Figure 52: Picture of the heat exchanger in the 0° arrangement (a), 45° arrangement (b) and 90° arrangement (c)

For the 0° (vertical) arrangement, the tests were done in order to evaluate two different evaporation mechanisms:

- Pool boiling, which was the mechanism examined for all the other configurations;
- Thin film evaporation.

Indeed, one of the main focal points of the experimental activity here presented is the evaluation of the feasibility and possible performance of an integrated evaporator/condenser for the hybrid chiller developed in the HYBUILD Mediterranean concept. In this case, the design of the sorption module would be a 4-vessels architecture and therefore the most suitable evaporator/condenser would be constituted by a pool boiling system, with the refrigerant of the sorption cycle in the pool and the refrigerant of the compression cycle flowing inside the tubes of the heat exchanger. However, when such a configuration is not possible, and the connection between the sorption and compression units in the hybrid is done hydraulically, by connecting the evaporator HTF circuit of the sorption module with the condenser HTF circuit of the compression unit, the standard design of Fahrenheit chillers, with 2 chambers, is the most suitable. The 2-vessels design, where each module contains the adsorber/desorber and the evaporator/condenser, reduces the space needed and eliminates the necessity of vacuum valves. In this case, thin film evaporation represents the most efficient way to realise the phase change of the refrigerant.

Consequently, both cases were tested, even though specific attention was devoted to the pool boiling case that allows exploiting the integrated evaporator/condenser concept.

4.2.3 Testing procedure – Pool boiling

The testing procedure during each test is as follows:

1. Pre-conditioning of the condenser and evaporator pools;
2. Setting of the level of the liquid and the desired flow rate and temperature of the HTF for the evaporator;
3. Opening of vacuum valves;
4. Start of recording;

5. After at least 10 minutes of evaporation under stationary conditions (i.e. the fluctuations in the evaporation power are lower than ± 200 W), the test is stopped.

In addition, some tests were done starting from the maximum level allowed until the heat exchanger under testing was completely above the level of liquid, in order to assess the effect of this parameter on the evaporation performance.

4.2.4 Testing procedure –Thin film evaporation

The testing procedure is the following:

1. Pre-conditioning of the condenser and evaporator (HTF and pool of the condenser, HTF of the evaporator). The heat exchanger under testing works as condenser, the HEX in the upper chamber as evaporator.
2. Opening of the vacuum valves;
3. The connection between the chambers is closed when the power in the chamber with the HEX under testing is 0 W.
4. Re-conditioning of the condenser and evaporator (HTF and pool of the condenser, HTF of the evaporator). The HEX under testing works as evaporator, the HEX in the upper chamber as condenser.
5. Opening of the vacuum valves;
6. Start recording;
7. The test is stopped once evaporation power is 0 W.

4.2.5 Data reduction

The main parameters used to characterize the heat exchanger, and correlate its performance also with the theoretical models that will be presented in the following sections, are the evaporation power and the overall heat transfer coefficient.

The evaporation power was calculated as:

$$\dot{Q} = \dot{m}c_p(T_{in} - T_{out})$$

Where \dot{m} [kg/s] is the flow rate of the HTF, c_p is its specific heat [kJ/(kgK)] and T_{in} and T_{out} are the temperatures of the HTF measured in proximity of the heat exchanger.

The overall heat transfer coefficient was measured as:

$$U = \frac{\dot{Q}}{A \text{ LMTD}}$$

Where A is the heat exchange area [m²] and LMTD is the logarithmic temperature difference, calculated as:

$$\text{LMTD} = \frac{(T_{in} - T_{out})}{\ln \frac{(T_{pool} - T_{in})}{(T_{pool} - T_{out})}}$$

Where T_{pool} is the average temperature of the liquid in the evaporator.

In addition, the overall heat transfer coefficient was separated into its main three components:

- The internal convective heat transfer on the HTF side of the heat exchanger h_i ;
- The thermal conduction in the metal of the fins k_{fins} ;

- The external convective heat transfer h_e , which is the term characterizing the process of evaporation under vacuum.

$$\frac{1}{U} = \frac{1}{h_i} + \frac{h_{fins}}{k_{fins}} + \frac{1}{h_e}$$

The internal heat transfer coefficient was calculated as:

$$\frac{1}{h_i} = \frac{D_h}{Nu k_w}$$

Where D_h is the hydraulic diameter, k_w is the thermal conductivity of water and Nu is the Nusselt number, which is equal to:

$$Nu_{lam} = 3.6568 \text{ (valid for } Re < 2300\text{)}$$

$$Nu_{turb} = 0.023 * Re^{\frac{4}{5}} * Pr^{\frac{1}{3}} \text{ (valid for } Re \geq 10^4\text{)}$$

where Re is the Reynolds-number (-) and Pr the Prandtl-number (-) of the HTF.

In the range $2300 < Re < 10^4$ the Nusselt number is calculated according to [8]:

$$Nu_m = (1 - \gamma) Nu_{lam} + \gamma Nu_{turb}$$

with

$$\gamma = \frac{Re - 2300}{10^4 - 2300}$$

In addition, the temperature difference between the HTF and the liquid in the evaporator was calculated as:

$$\Delta T_{pool} = \frac{(T_{in,e} - T_{out,e})}{2} - T_{liq,ave,e}$$

While the temperature difference between the condenser and the evaporator was calculated as:

$$\Delta T_{c-e} = T_{liq,ave,e} - T_{liq,ave,c}$$

4.2.6 Example of a typical test – 0° configuration, pool boiling, submersed HEX

In this section, a typical test is analysed, in order to better explain the parameters recorded and their typical evolutions. The test that will be analysed is done with HTF inlet temperature of 40°C, flow rate of the HTF in the evaporator of 12 kg/min, average temperature at the condenser of 10°C and average temperature of the pool at the evaporator of 35°C. Figure 53 shows the evolution of the pressure inside the two vacuum chambers. Since they are connected, the pressure inside the two chambers follows the same trend. The pressure is almost constant throughout the duration of the test and corresponds to the saturation pressure at the temperature of the vapour in the evaporator.

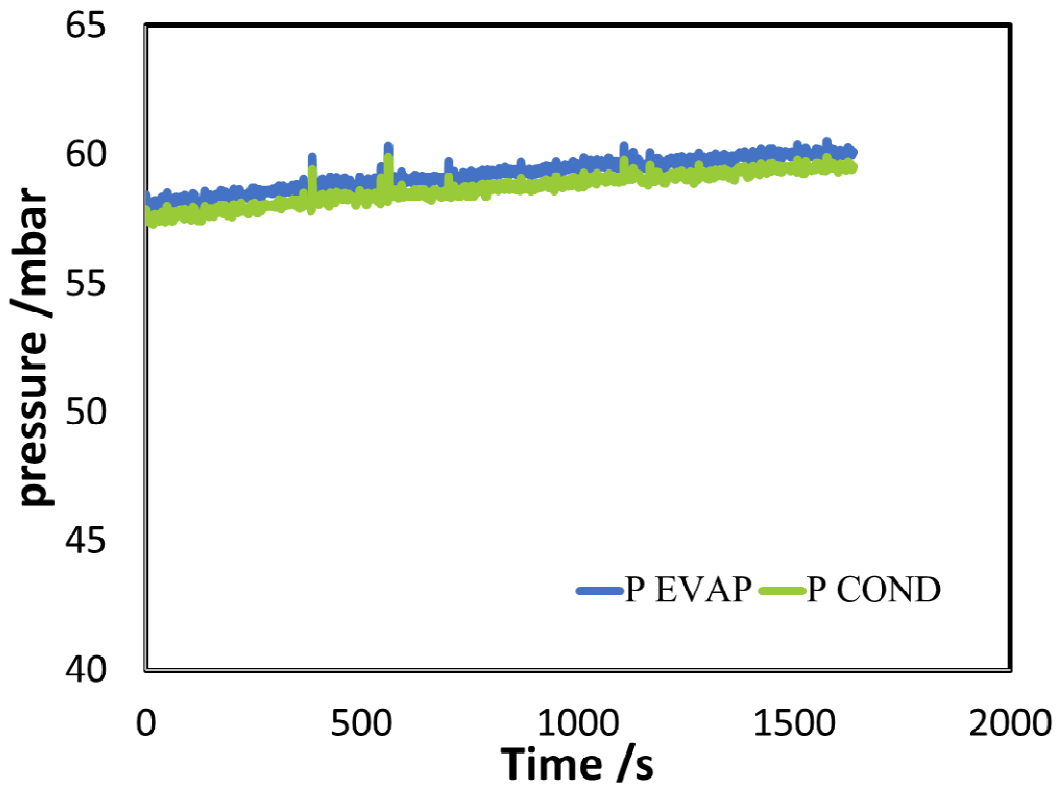


Figure 53: Pressure evolution for a typical test of the evaporator HEX.

Figure 54 presents the trend of the various temperatures inside the evaporator, as well as the ones in the HTF circuit. It is possible to notice that the temperatures are all constant for the duration of the test, with some fluctuations more evident in the temperature of the liquid at the bottom of the evaporator due to the bubbles that arise to the surface and the continuous mixing of water. The three thermocouples located in the proximity of the heat exchanger do not evidence a clear stratification, due to the small height of the HEX when installed horizontally.

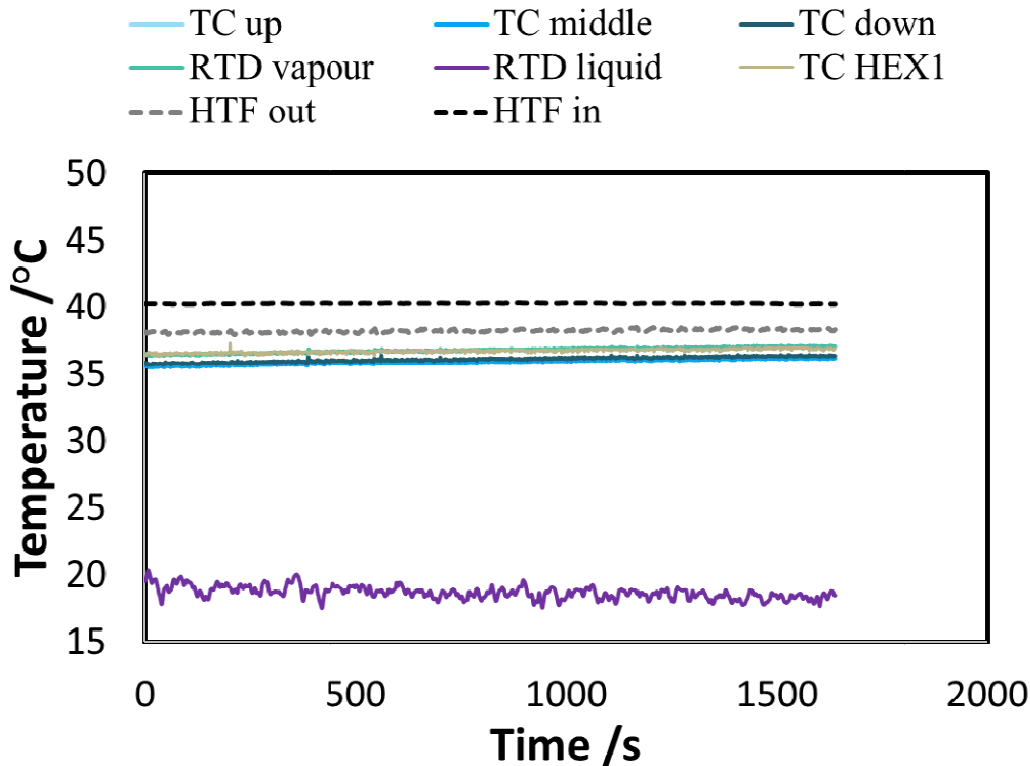


Figure 54: Temperatures in the evaporator for a typical test.

Figure 55 shows the temperatures in the condenser during the same test. It is intuitive to notice that the temperature of the liquid is flat, whereas the temperature of the vapour is fluctuating since it is influenced by the behaviour of the evaporator.

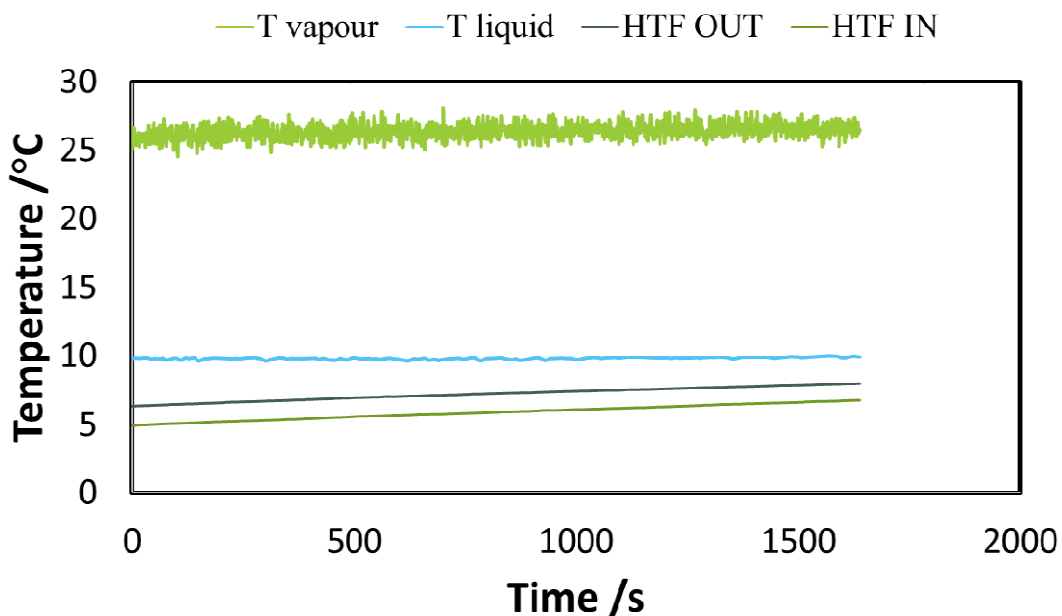


Figure 55: Temperatures in the condenser for a typical test.

Finally, Figure 56 shows the trend of the power measured at the evaporator and condenser. Ideally, the two powers should be identical, but there is indeed a small discrepancy between them, due to two effects: on the one side, there is a small effect of heating of the pool in the proximity of the heat exchanger in the evaporator and, on the other side, since the amount of

liquid water inside the condenser is much bigger than in the evaporator, part of the useful effect cannot be properly detected by the temperature sensors.

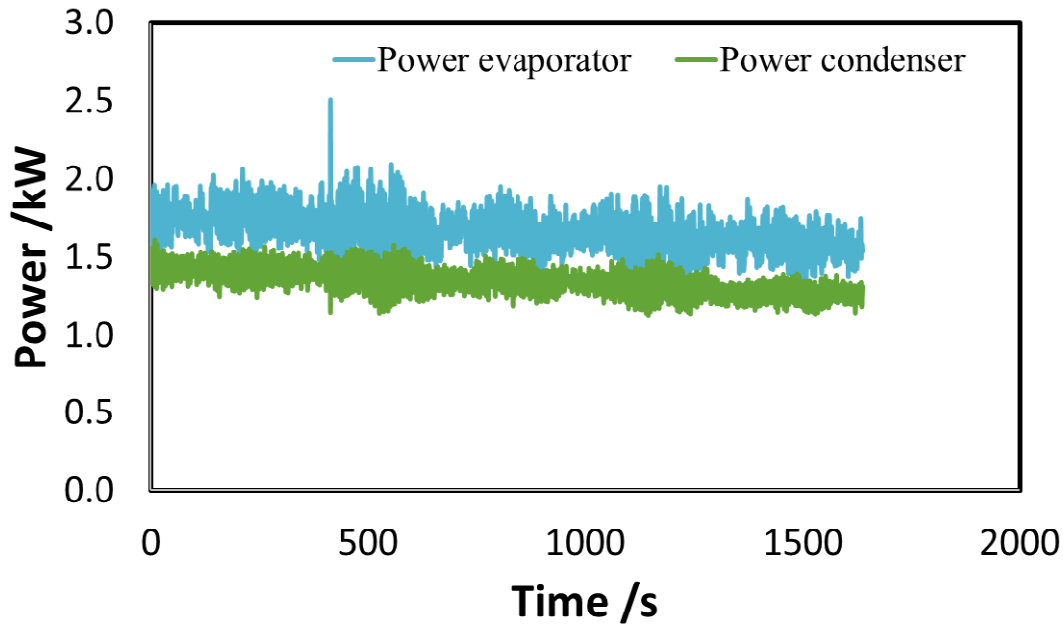


Figure 56: Powers in the condenser and evaporator during a typical test.

4.2.7 List of tests – pool boiling

A wide range of conditions were evaluated, in order to have a complete characterization of the heat exchanger under realistic operation. In particular, flow rate of the HTF in the evaporator, ΔT between evaporator and condenser and ΔT between the HTF in the evaporator and the pool of liquid in the evaporator were varied to determine their effect on the overall performance.

A list of all the testing conditions examined is reported in Table 9.

Table 9: Tested conditions for the characterization of the evaporator under pool boiling.

Test	Evap in	Cond in	Flow rate evap	ΔT_{c-e}	ΔT_{pool}
-	°C	°C	kg/min	K	K
1	33.8	5.3	6.3	17.8	3.0
2	32.4	6.0	9.5	18.0	2.2
3	31.6	4.9	13.3	17.8	1.9
4	31.4	5.7	16.3	17.9	1.8
5	31.3	6.2	20.4	17.9	1.7
6	27.2	6.8	4.1	17.9	3.1
7	32.4	7.0	4.1	16.6	1.9
8	33.9	5.8	8.2	17.9	2.4
9	29.0	5.2	5.2	13.9	2.6
10	28.5	5.4	10.1	14.0	2.2
11	28.3	5.6	12.4	14.1	1.8
12	27.9	6.0	16.8	14.2	1.6
13	28.0	5.6	20.4	14.2	1.5

14	34.2	5.2	5.4	15.2	2.9
15	39.4	6.6	5.4	16.1	4.0
16	39.8	5.3	12.8	16.5	2.8
17	39.8	6.3	20.3	16.9	2.0
18	39.8	5.8	7.8	16.7	2.6
19	38.9	7.9	7.7	13.0	11.6
20	31.0	5.9	5.6	16.5	3.0
21	31.0	5.9	10.7	16.1	2.9
22	31.0	6.5	14.9	16.2	2.9
23	31.4	5.5	20.2	15.9	3.1
24	39.1	5.4	5.9	15.8	5.7
25	39.9	5.5	5.4	17.4	5.0
26	40.0	6.0	9.4	17.5	3.9
27	39.9	5.6	11.7	17.8	3.4
28	39.8	5.8	15.4	18.1	2.3
29	39.9	5.6	19.6	18.4	1.4
30	39.9	5.6	19.1	19.3	1.8
31	40.1	5.8	19.7	14.1	3.9
32	39.3	6.3	5.1	16.3	3.8
33	23.5	7.2	19.5	7.5	4.7
34	28.6	5.4	10.0	10.5	4.6
36	39.2	5.8	8.6	13.9	5.9
39	39.7	6.2	9.7	13.2	5.7
40	39.6	5.8	5.6	13.5	5.2
41	39.8	5.9	15.1	14.3	5.0
42	39.8	5.8	19.9	14.6	5.2
43	23.6	5.8	9.3	11.5	1.8
44	31.6	6.1	9.3	16.1	3.6
45	31.7	5.9	5.4	16.3	3.4
46	32.1	5.8	14.3	16.1	3.3
47	25.5	5.7	9.2	7.6	4.3
48	25.9	6.1	15.7	7.8	4.1
49	25.5	5.7	20.0	8.1	3.6
50	25.6	5.5	5.7	7.4	4.7
51	33.8	5.7	9.4	8.1	6.7
52	34.0	6.0	5.2	8.9	5.9
55	23.5	5.3	10.3	5.9	2.6
56	23.2	5.6	5.3	4.8	2.7
57	24.3	6.1	14.0	5.3	3.0
58	23.6	5.5	20.0	5.2	2.7
59	39.5	5.5	4.9	4.8	9.4
60	39.5	6.0	9.4	5.6	9.3
61	39.1	6.0	14.2	5.7	9.2
62	38.8	6.2	20.2	6.0	9.8

63	29.8	6.0	5.0	5.0	7.0
64	31.1	5.9	10.2	4.9	7.5
65	30.9	5.8	14.5	4.8	7.8
66	30.0	5.8	20.2	5.1	7.9
67	39.2	5.0	9.9	12.8	6.5
68	39.0	5.2	9.9	10.1	7.2
69	38.7	6.6	5.8	9.0	6.6
70	38.8	6.1	14.2	9.8	6.1
71	38.6	6.5	20.4	9.1	6.2
73	39.7	5.1	6.0	8.5	9.1
74	39.5	5.7	9.9	8.6	8.9
75	39.1	5.5	14.0	8.8	8.7
76	38.8	5.4	20.3	9.4	8.5
77	43.7	6.0	20.3	8.2	9.7
78	43.5	5.8	14.1	8.0	9.4
79	43.7	5.5	9.5	8.0	10.2
80	44.0	5.2	5.9	8.6	9.8
81	41.4	5.0	6.0	12.6	8.1
82	43.0	6.1	9.0	13.1	8.7
83	44.9	5.6	13.6	13.0	10.5
84	45.2	5.6	19.9	12.5	12.1

In the next sections, the effect of various operating parameters and a comparison of the various configurations will be presented.

4.2.8 Test results -pool boiling

4.2.8.1 0° configuration

Figure 57 shows the effect of the flow rate of the HTF on the ΔT_{pool} for three sets of tests, differing for the ΔT between the evaporator and condenser. All the tests are done with a fixed inlet temperature of the HTF at the evaporator, i.e. 40°C. As it is possible to notice, there is a progressive reduction in the ΔT_{pool} for an increasing flow rate, whereas the effect of the $\Delta T_{\text{e-c}}$ is secondary. Indeed, this effect (i.e. the reduction in the ΔT_{pool}) becomes noticeable because the spiral copper coil that is used for the initial conditioning of the temperature of the evaporator is undersized compared to the heat exchanger under testing and therefore, at the beginning of each test, there is a phase corresponding to the sensible heating of the liquid in the evaporator, that depends almost solely on the performance of the heat exchanger under testing. Indeed, such a condition corresponds to realistic operating conditions, since in the sorption module the heat exchanger of the evaporator is the only responsible for the conditioning of the water reservoir in the vacuum vessel.

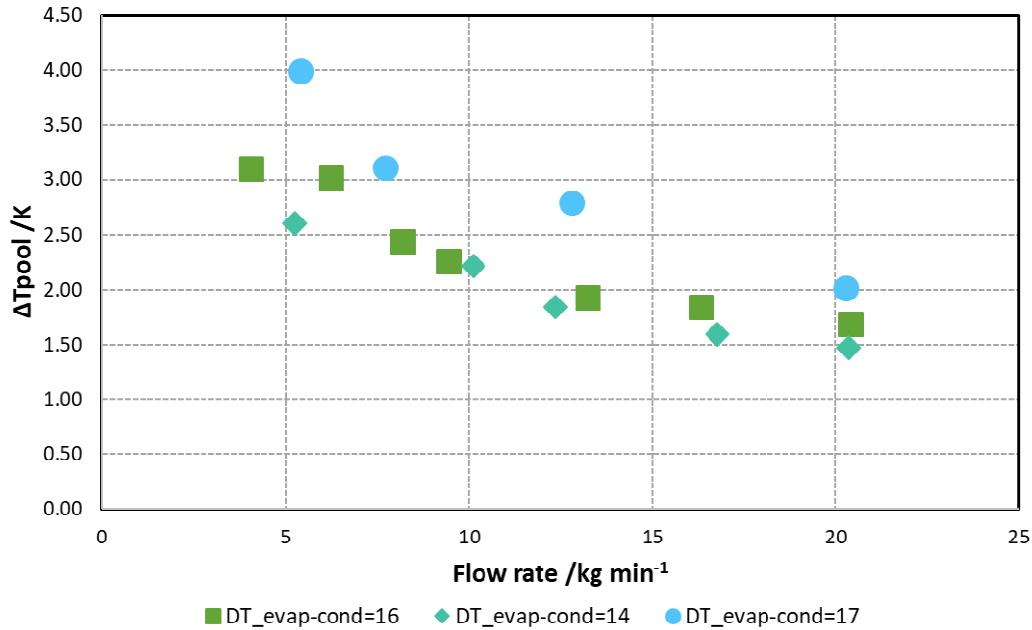


Figure 57: Effect of the flow rate on ΔT_{pool} – 0° configuration.

Figure 58 and Figure 59 show the effect of the flow rate on the evaporation power and overall heat transfer coefficient, respectively. The results are reported for two different ΔT_{e-c} , i.e. 15 K and 19 K. The evaporation power increases with the flow rate and is higher for a higher ΔT_{e-c} : for ΔT_{e-c} of 15 K, it ranges from 1.6 to 2.7 kW, whereas for ΔT_{e-c} =19 K, it ranges from 2.2 kW to 2.9 kW. The experimental points converge around the value of 2.8-2.9 kW that might be considered as the limit of the heat exchanger under the conditions tested. The corresponding overall heat transfer coefficients are reported in Figure 59: for ΔT_{e-c} of 15 K, it ranges from 190 to 427 W/(m²K), whereas for ΔT_{e-c} =19 K, it ranges from 289 W/(m²K) to 607 W/(m²K).

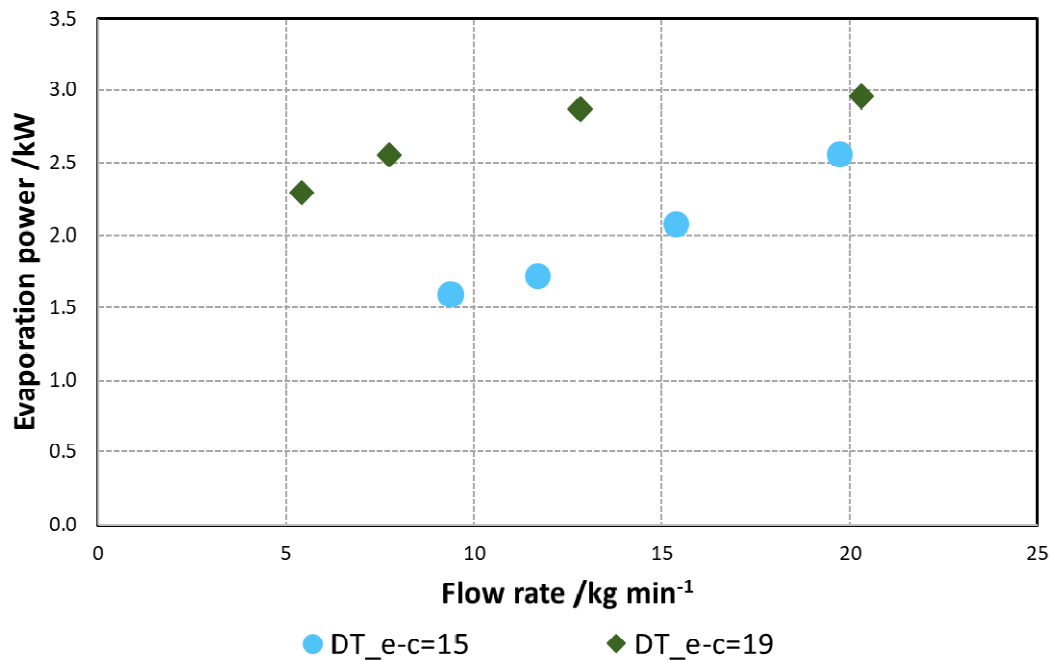


Figure 58: Combined effect of the flow rate and the ΔT_{c-e} on the evaporation power – 0° configuration.

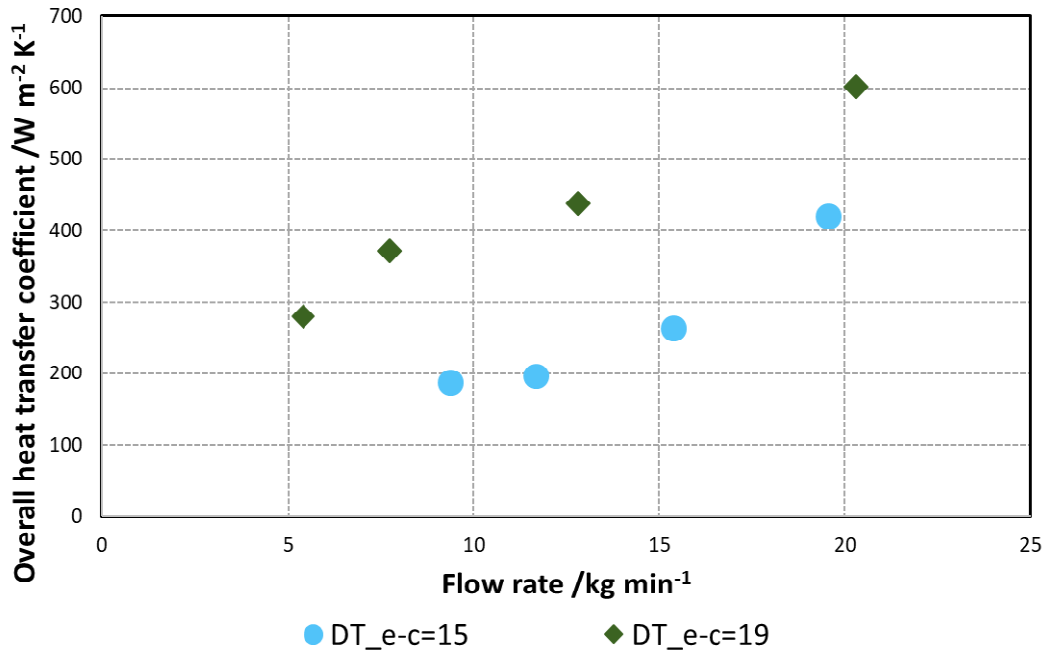


Figure 59: Combined effect of the flow rate and the ΔT_{e-c} on the overall heat transfer coefficient – 0° configuration.

4.2.8.2 45° inclination configuration

The same parameters studied in the horizontal configuration were evaluated also for the case of the heat exchanger with an inclination of 45°. Figure 60 shows the effect of the flow rate of the HTF on the ΔT_{pool} for two sets of tests, differing for the ΔT between the evaporator and condenser. All the tests are done with a fixed inlet temperature of the HTF at the evaporator, i.e. 31°C. Compared to the previous case, where there was a sensible reduction of the ΔT_{pool} with the flow rate, in this case, the value is almost constant under all conditions. This is due to two factors: the higher amount of water needed. Indeed, all the tests presented in this section are done with the water up to half of the height of the heat exchanger. Compared to the previous case, 14 l of additional distilled water were added, which allows keeping the temperature of the pool more constant. Secondly, as will be described in section 4.4.1, in the previous case, evaporation occurred all over the surface of the heat exchanger, whereas in this case it occurs at the interface between the heat exchanger and the water and therefore the mixing of the water in the pool due to the formation of a high number of bubbles is less marked.

Figure 61 and Figure 62 show the effect of the flow rate on the evaporation power and overall heat transfer coefficient, respectively. The results are reported for the same ΔT_{e-c} as in the previous graph, i.e. 8 K and 15 K. The evaporation power increases with the flow rate and is higher for a higher ΔT_{e-c} : for ΔT_{e-c} of 15 K, it ranges from 2.5 to 3.7 kW, whereas for ΔT_{e-c} =8 K, it ranges from 0.5 kW to 1.6 kW. As already evidenced for the horizontal configuration, the initial increase of the evaporation power with the flow rate is quite high, i.e. passing from 5 kg/min to 10 kg/min it increases about 30%, but a plateau is reached afterwards, that can be considered as the limit of the heat exchanger under the conditions tested. The corresponding overall heat transfer coefficients are reported in Figure 62: for ΔT_{e-c} of 15 K, it ranges from 210 to 240 W/(m²K), whereas for ΔT_{e-c} =8 K, it ranges from 70 W/(m²K) to 140 W/(m²K).

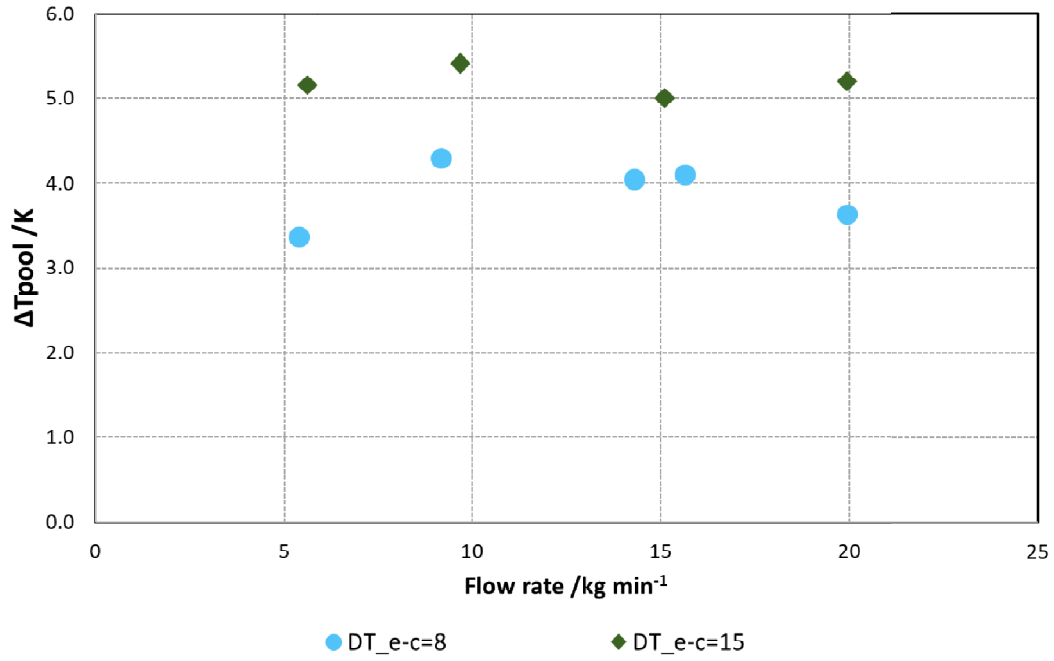


Figure 60: Effect of the flow rate on ΔT_{pool} – 45° configuration.

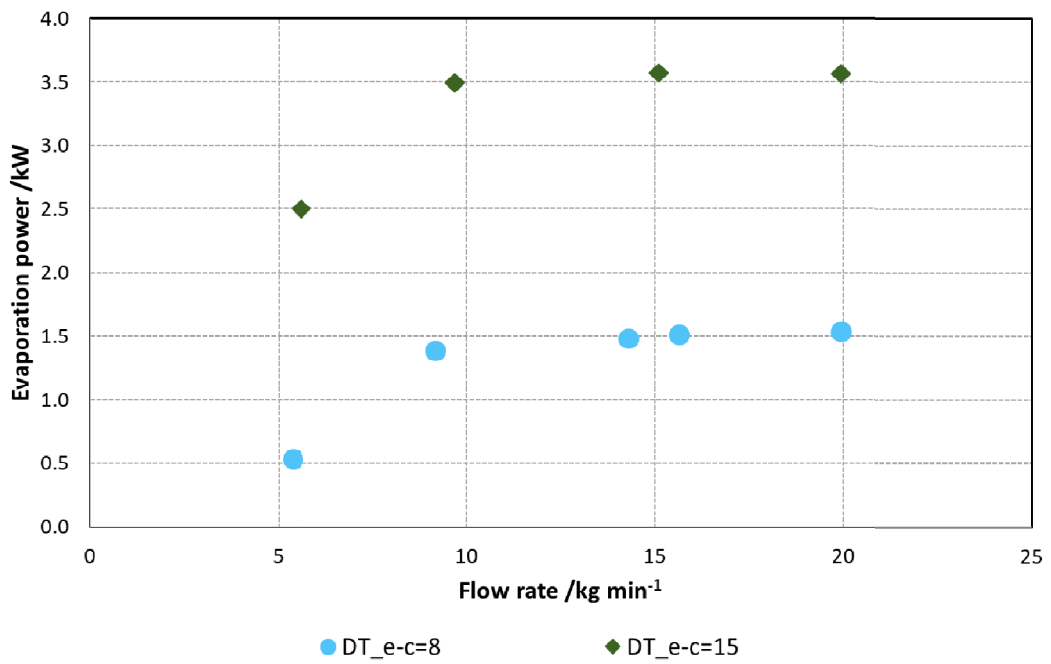


Figure 61: Combined effect of the flow rate and the ΔT_{c-e} on the evaporation power - 45° configuration.

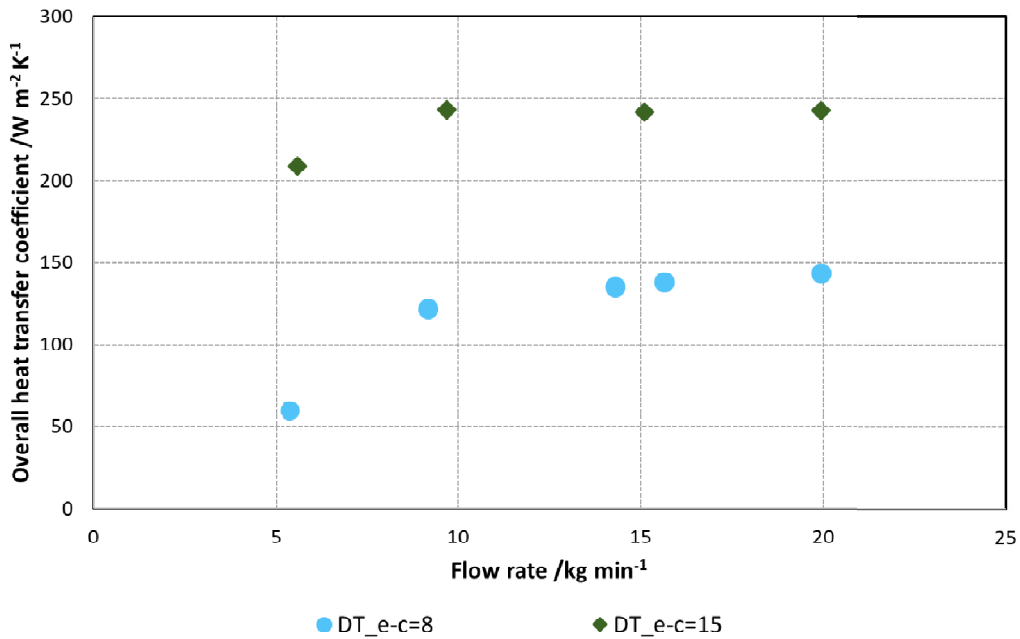
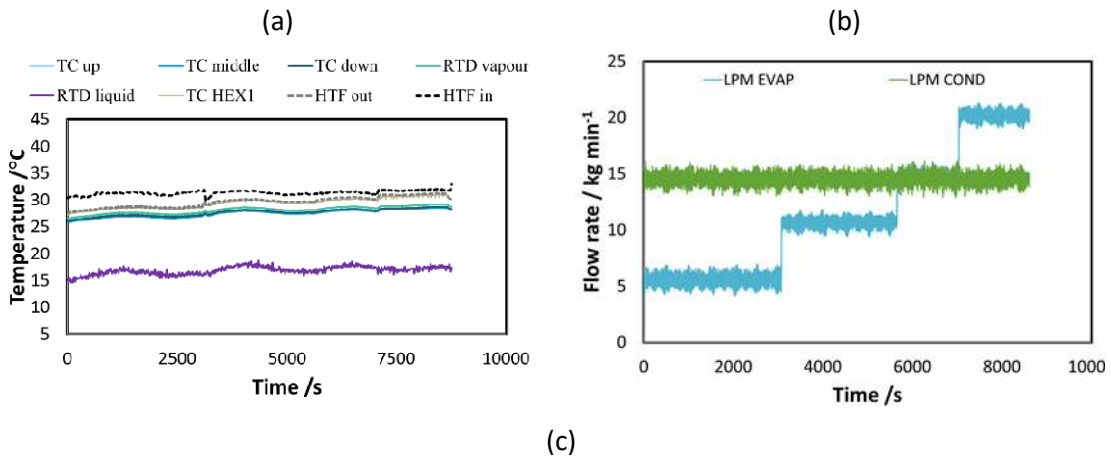


Figure 62: Combined effect of the flow rate and the ΔT_{c-e} on the overall heat transfer coefficient - 45° configuration.

The effect of the flow rate and the various contributions on the overall heat transfer coefficient can be seen by looking at the results in Figure 63. The test was done for 45° configuration keeping constant temperature conditions in the evaporator and condenser, but changing the flow rate of the HTF with time. Two main results can be highlighted: the overall heat transfer coefficient coincides with h_e on the pool side, since it represents the main resistance, and there is a clear increment of the internal convective heat transfer h_i with the flow rate of the HTF, passing from a laminar regime to a turbulent one.



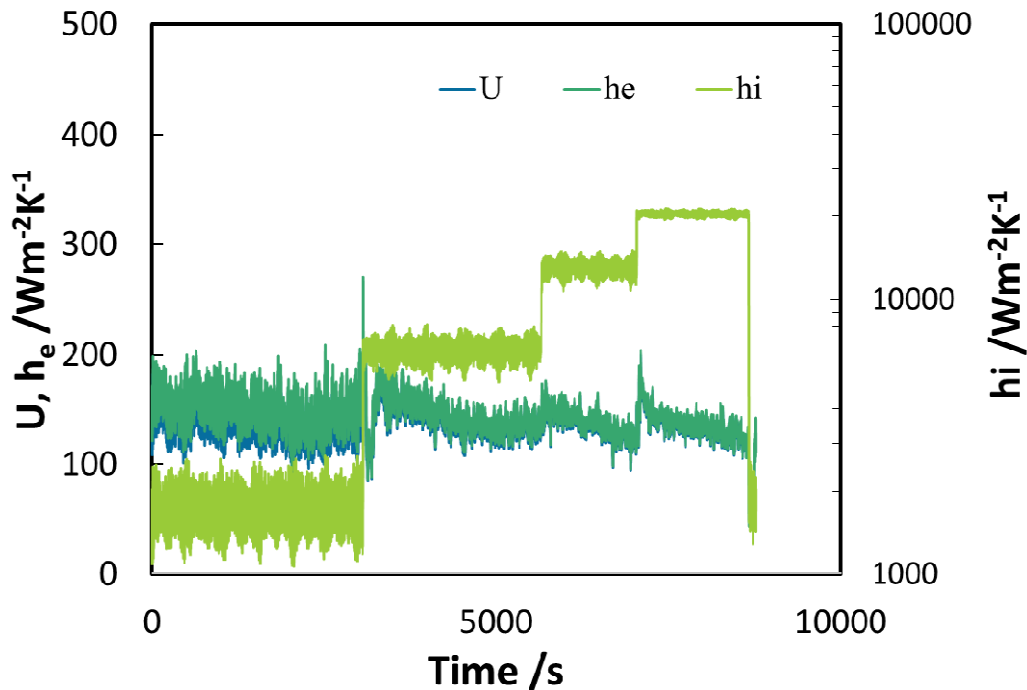


Figure 63: Effect of the flow rate and relative contributions to the overall heat transfer coefficient.

The same results, even though they are not shown in the present report, were obtained for the heat exchanger in horizontal configuration.

4.2.8.3 90° inclination configuration

Finally, the 90° inclination was tested, highlighting the effect of the operating parameters under this condition. Figure 64 shows the effect of the flow rate of the HTF on the ΔT_{pool} for two sets of tests, differing for the ΔT between the evaporator and condenser. All the tests are done with a fixed inlet temperature of the HTF at the evaporator, i.e. 39°C. It can be seen that, for this arrangement, the ΔT_{pool} is higher than in the other cases. This is due to two factors: on the one hand, similarly to the 45° inclination, there is a higher amount of water compared to the 0° inclination case. On the other hand, compared to the 45° inclination, the level of water, related to the height of the heat exchanger, is higher.

Figure 65 and Figure 66 show the effect of the flow rate on the evaporation power and overall heat transfer coefficient, respectively. The results are reported for the same $\Delta T_{\text{e-c}}$ as in the previous graph, i.e. 6 K and 10 K. The evaporation power increases with the flow rate and is higher for a higher $\Delta T_{\text{e-c}}$: for $\Delta T_{\text{e-c}}$ of 10 K, it ranges from 4.1 to 7.7 kW, whereas for $\Delta T_{\text{e-c}}=6$ K, it ranges from 3 kW to 4.8 kW. The corresponding overall heat transfer coefficients are reported in Figure 66: for $\Delta T_{\text{e-c}}$ of 10 K, it ranges from 340 to 480 W/(m²K), whereas for $\Delta T_{\text{e-c}}=6$ K, it ranges from 180 W/(m²K) to 250 W/(m²K). Compared to the cases examined previously, the evaporation power measured is higher, which is due to (i) the higher amount of water with respect to the 0° inclination, that in turn keeps the ΔT_{pool} higher; (ii) the higher level with respect to the 45° inclination, which means that the manifold (that, in the examined heat exchanger, is quite bulky) is completely immersed and that the whole heat exchanger is immersed. The tests with the 45° inclination were done with a level of 0.6H, in order not to have the whole chamber of the evaporator filled with water, since the height of the HEX would have required to have water almost until the top of the chamber, which wouldn't have left space for vapour.

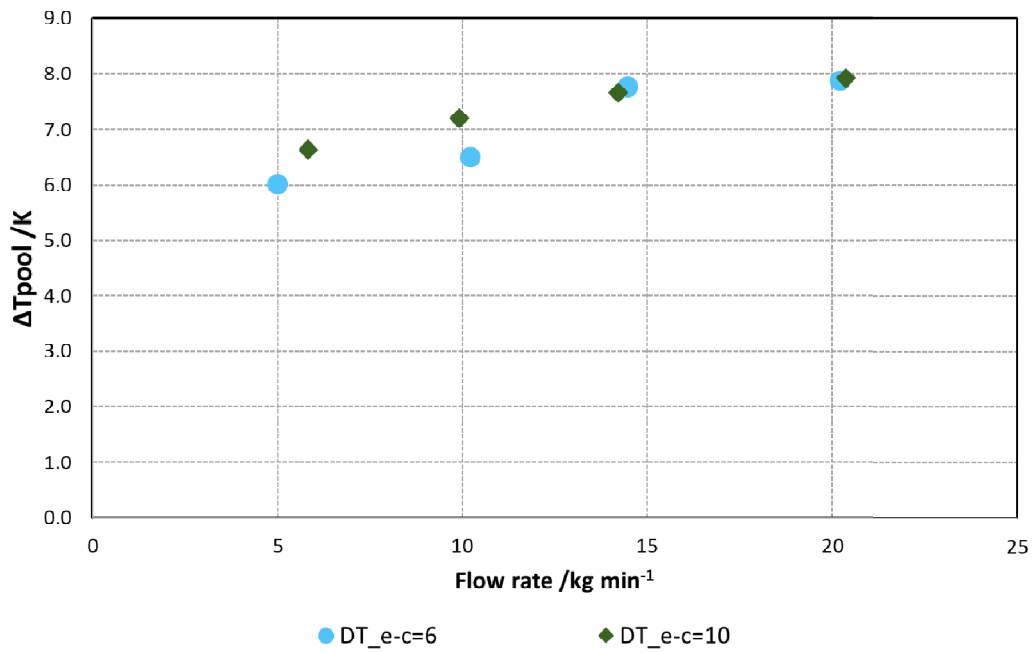


Figure 64: Effect of the flow rate on ΔT_{pool} – 90° configuration.

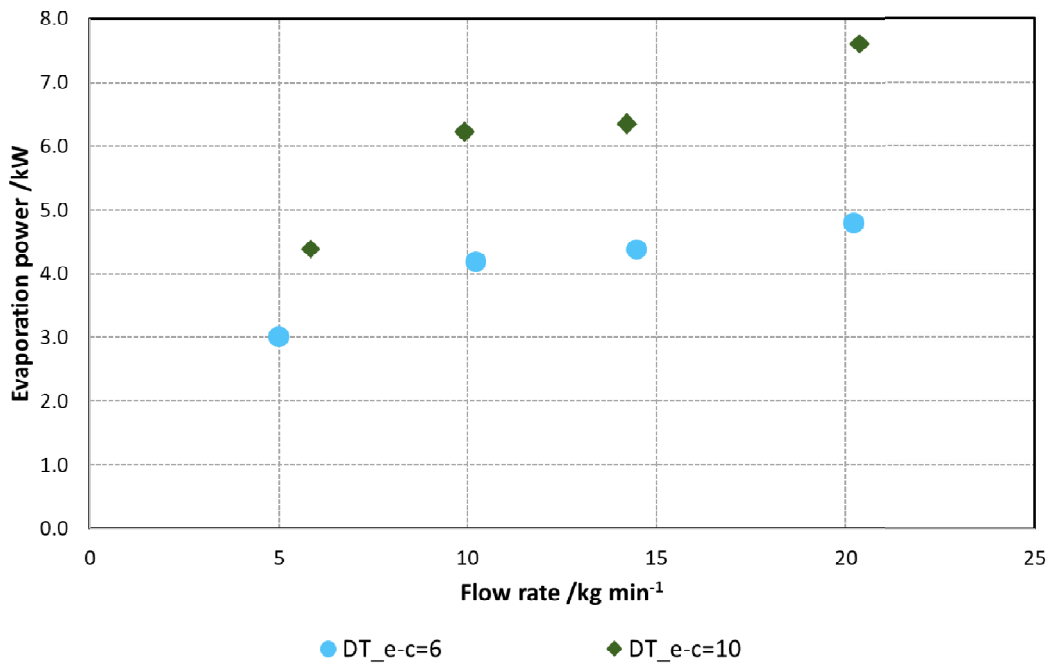


Figure 65: Combined effect of the flow rate and the ΔT_{c-e} on the evaporation power - 90° configuration.

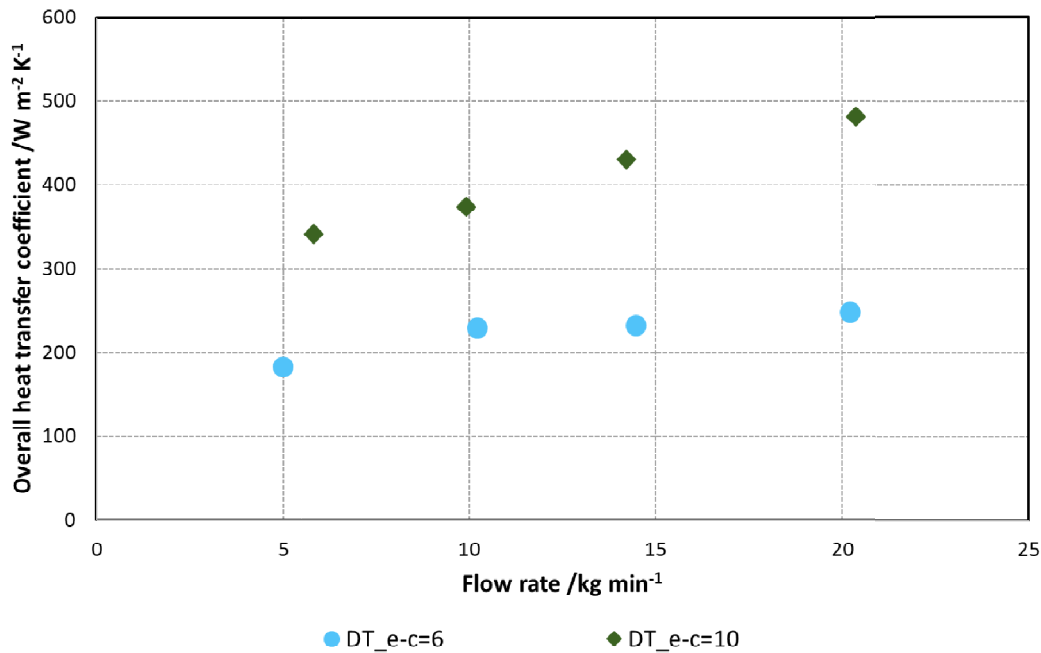


Figure 66: Combined effect of the flow rate and the ΔT_{c-e} on the overall heat transfer coefficient - 90° configuration.

4.2.9 Comparison of the different arrangements

The different arrangements, i.e. installation with inclination of 0° (horizontal), 45° and 90° were compared by means of evaporation power and overall heat transfer coefficient at different flow rates. The tests chosen for comparison are done under the same ΔT_{e-c} and the same level of water in the pool, i.e. 0.6H (with H as height of the heat exchanger). The results are presented in Figure 67 and Figure 68. As it is possible to notice from Figure 68, the overall heat transfer coefficient is higher for a higher flow rate. In general, the overall heat transfer coefficient is higher for the 45° inclination case when the flow rate is lower, whereas almost the same value is measured for higher flow rates, indicating that the limit for the heat exchanger is reached. For all cases, the variation of the heat transfer coefficient, at a given flow rate, is within 50 W/m²K, indicating that the main evaporation mechanism is pool boiling and no other significant phenomena (i.e. capillary or thin film evaporation) occur. Such an aspect will be further investigated in section 4.3. The results of Figure 67, that present the evaporation power in the two cases seem to indicate that the heat exchanger works better in 45° inclination configuration. Indeed, the higher evaporation power is due to an indirect effect of the configuration (that would be present also in the application in realistic conditions in an adsorption module): as previously discussed, the configuration with 45° inclination allows keeping a higher ΔT_{pool} , which has a beneficial effect on the evaporation power. The 90° inclination has an intermediate behaviour between the case of 0° and 45°. This is due to the fact that, similarly to the case of 45°, a higher amount of water is present in the chamber, which works as a reservoir and increases the ΔT_{pool} . The lower evaporation power, if compared to the 45° configuration, is due to the unfavourable inclination that, as will be shown in the next sections, penalises the formation of big bubbles. From such results, it is possible to conclude that the 45° inclination configuration performs better and is less sensible to operating conditions, which is an important factor in a sorption module, since the system should be sized to work under very different boundaries (for example, high variations of ambient temperature).

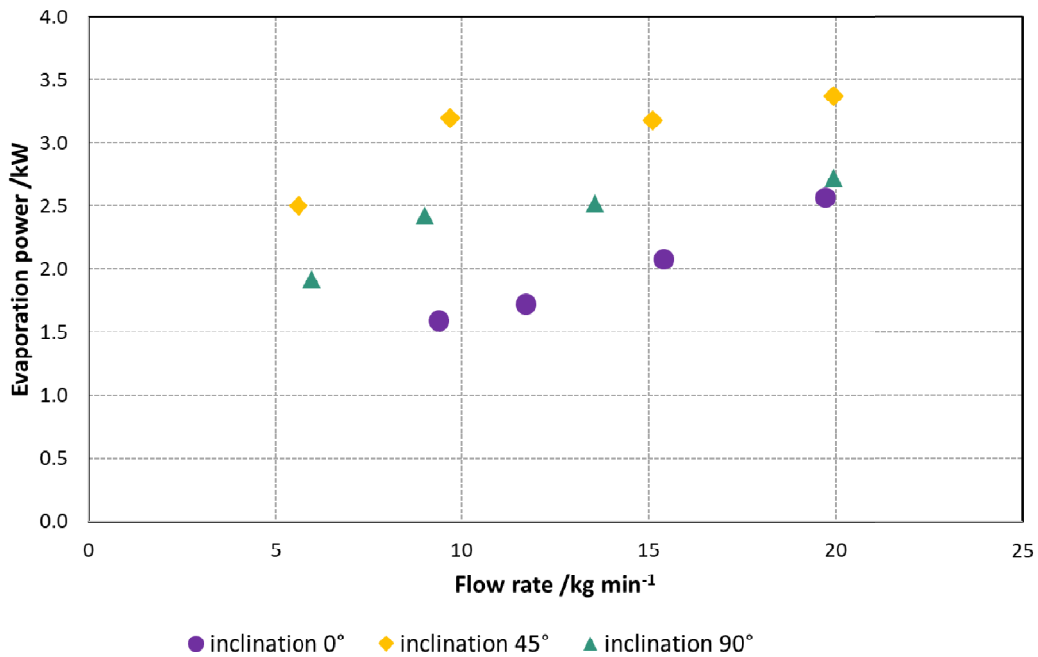


Figure 67: Evaporation power for tests with $\Delta T_{e-c}=15$ K and different inclinations of the heat exchanger.

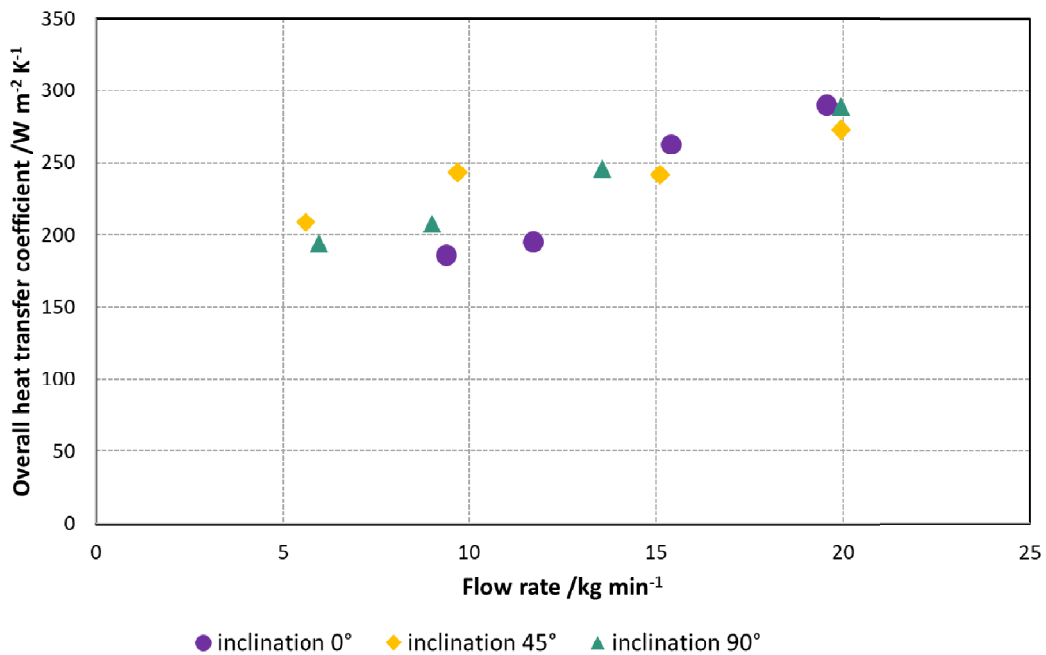


Figure 68: Overall heat transfer coefficient for tests with $\Delta T_{e-c}=15$ K and different inclinations of the heat exchanger.

4.2.10 Configurations with variable level of the refrigerant

Apart from the different inclination of the heat exchanger, the possibility of having a different refrigerant level was investigated. The results are presented in Figure 69 for the 0° inclination case: there is a peak in the evaporation power at the beginning due to the sensible heating of the pool and subsequently, evaporation power progressively decreases until it approaches almost zero when the level of the refrigerant is below the minimum height of the heat exchanger. A similar trend is observed when the heat exchanger is installed with an inclination of 45° and 90°, as shown in Figure 70 and Figure 71. In this case, the time needed to dry out

the heat exchanger is higher due to the higher amount of refrigerant. However, what is interesting to notice is that the system keeps a higher evaporation power throughout the whole process. In addition, the reduction in the evaporation power is gradual with the gradual decreasing level whereas for 0° inclination, there is an abrupt reduction in the evaporation power as soon as the heat exchanger is not wet anymore. It is also possible to see that the fluctuation in the evaporation power is much higher for the 45° case, especially when the water level is high. This is intrinsically due to the fact that the bubbles can form only at the interface between the heat exchanger and the evaporator rather than on the complete surface. This means that there is an “idle” time before one set of bubbles collapses and another one goes up until the interfaces, this behaviour causes periods with lower evaporation power and therefore a marked fluctuation of such a parameter with time.

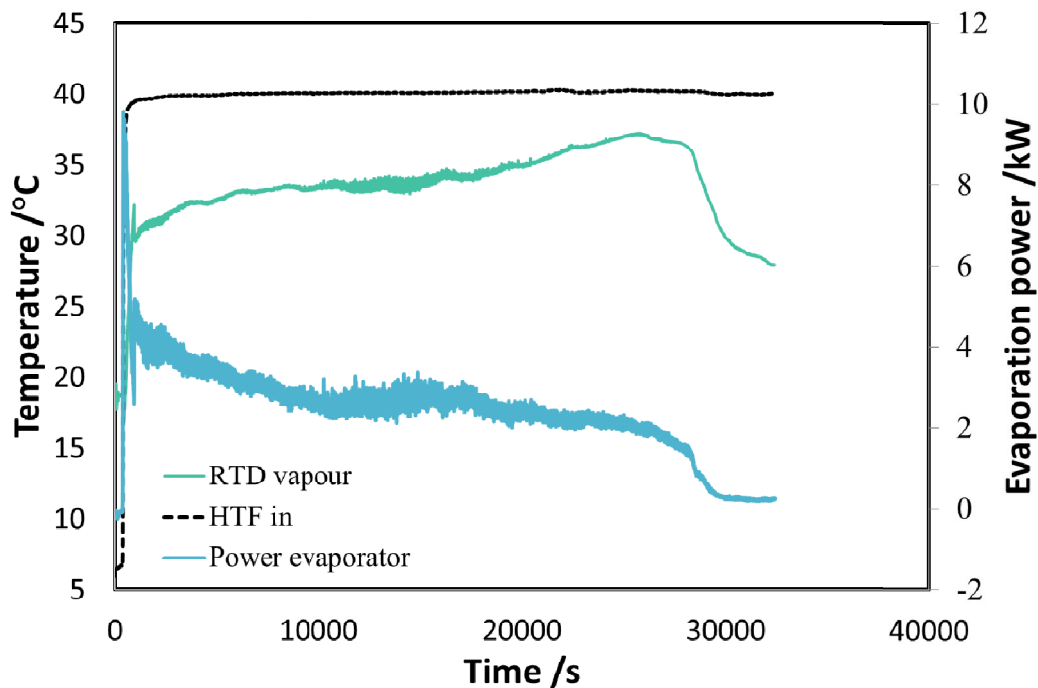


Figure 69: Effect of refrigerant level - horizontal arrangement.

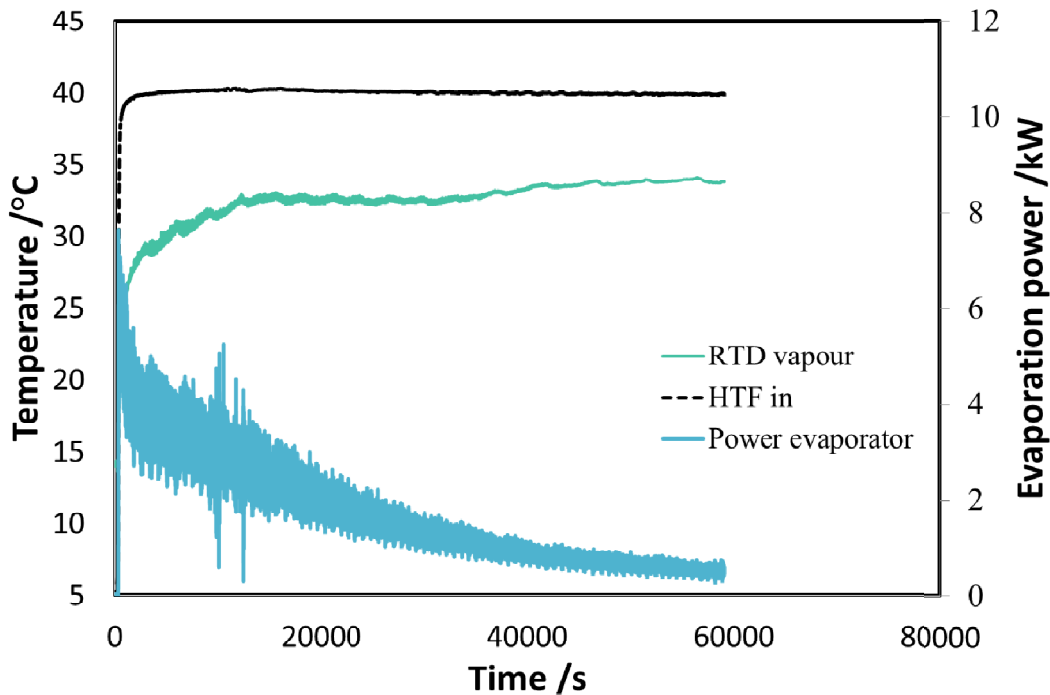


Figure 70: Effect of refrigerant level -45° arrangement.

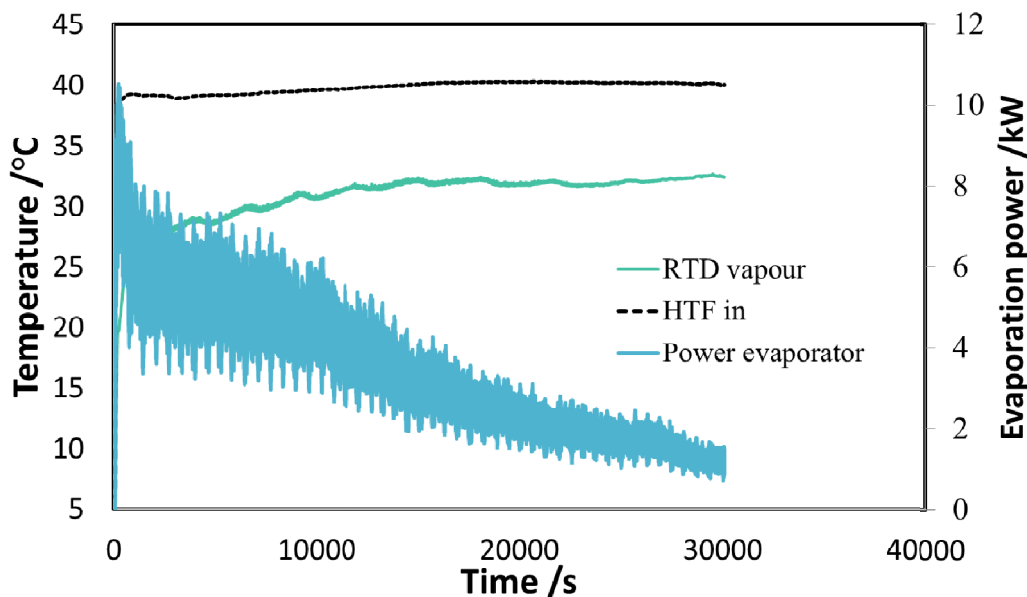


Figure 71: Effect of refrigerant level -90° arrangement.

Outcome of this experimental activity is then that the best configuration, among the various ones tested (i.e. different positions and different refrigerant level) is the one with the heat exchanger at 45° and covered by water for around 60% of its height.

4.3 Test results – thin film evaporation

4.3.1 Effect of HTF flow rate

The tests done under thin film evaporation are intrinsically unsteady, since they are done starting from the HEX wet from the maximum water amount that it can retain during condensation and end once all such water is evaporated. Therefore, their analysis cannot preclude from the dynamic behaviour. The effect of the flow rate of the HTF on evaporation

power can be seen in Figure 72, where three different flow rates are compared. All the tests are done with $T_{\text{cond}}=15^{\circ}\text{C}$ and an inlet temperature of the HTF at the evaporator of 40°C . At 5 kg/min, the peak power is 5.5 kW, at 10 kg/min it is 8.2 kW, at 20 kg/min it is 11.5 kW. Such a result clearly indicates that higher flow rates are beneficial also under this configuration for the evaporator and allow reaching a very high evaporation capacity. It is worth noticing that the peak power obtained at 20 kg/min, i.e. 11.5 kW, is higher than the maximum evaporation capacity measured under pool boiling conditions.

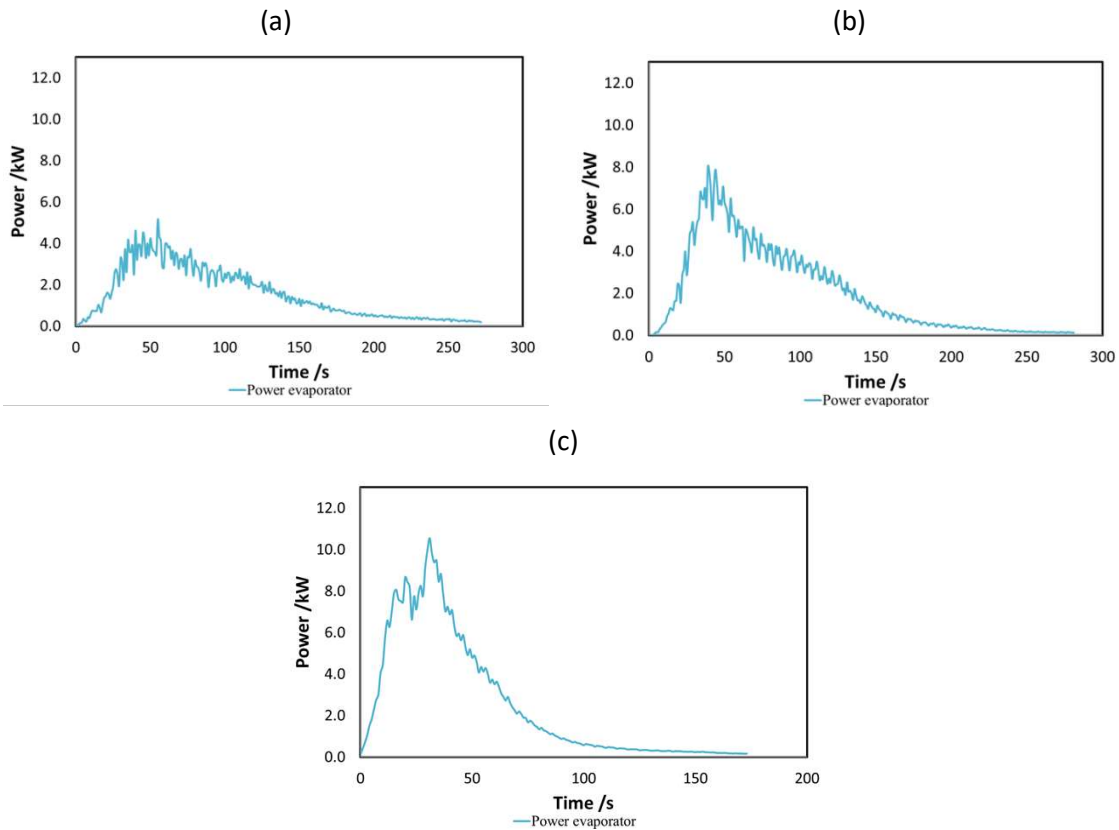
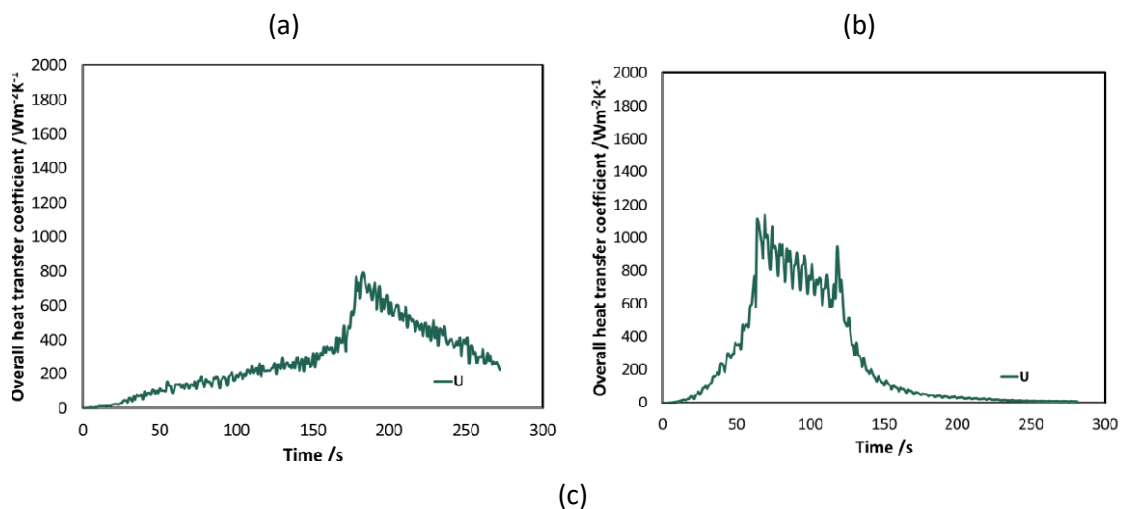


Figure 72: Effect of HTF flow rate on evaporation power for thin film evaporation tests: (a) 5 kg/min; (b) 10 kg/min; (c) 20 kg/min

The effect of the HTF flow rate on the overall heat transfer coefficient can be seen in Figure 73: for 5 kg/min the peak U is $870 \text{ W}/(\text{m}^2\text{K})$, for 10 kg/min it is $1200 \text{ W}/(\text{m}^2\text{K})$, for 20 kg/min it is $1500 \text{ W}/(\text{m}^2\text{K})$, values that are one order of magnitude higher than in the case of pool boiling.



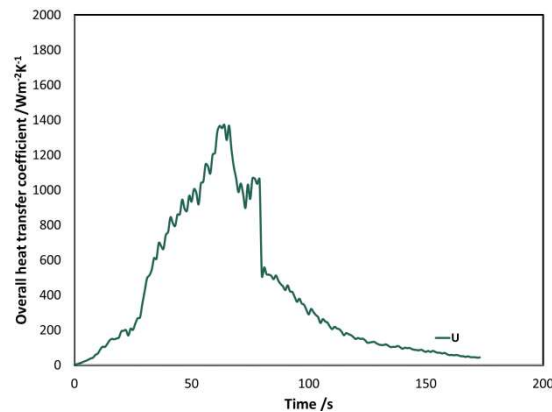


Figure 73: Effect of HTF flow rate on heat transfer coefficient for thin film evaporation tests: (a) 5 kg/min; (b) 10 kg/min; (c) 20 kg/min

4.4 Semi-empirical models for the investigation of water evaporation under sub-atmospheric pressure conditions - pool boiling

The identification of a semi-empirical model was focused on the pool boiling case, due to the higher amount of data collected and in response to the need of being able to design a system with integrated evaporator/condenser, whereas the thin film evaporation, that represents Fahrenheit's standard configuration in commercial products, was not evaluated theoretically but only on the basis of experimental data.

4.4.1 Identification of the evaporation mechanism

The pool boiling of water under sub-atmospheric conditions is a complex phenomenon, whose rigorous study is still on-going. Different works are available in literature that tried to clarify the mechanism of evaporation. For instance, Chan et al [9] investigated pool boiling heat transfer on finned surfaces, using water at sub-atmospheric pressures, observing the boiling mechanism by means of a high speed camera. 2 different behaviours, for low and high heat fluxes were observed:

- for low heat fluxes, nucleation starts at the fin root between two adjacent fins. As the bubble grows, it is forced to take the shape of the fin space, thus forming a thin vertical vapour film/plug. This vapour film grows as it absorbs heat near the fin wall and base. When it reaches the fin tip, the vapour retakes its supposed spherical shape and rapidly expands to a larger bubble. As the bubble lifts off, it drags out the rest of the vapour film from the fin space. Finally, liquid fills up the fin space and the cycle repeats all over again. On occasion vapour film is seen to oscillate in size in the low heat flux region. This occurs while the vapour film is cooled by liquid convection and results in the film intermittently shrinking its size. As thin liquid film is created in between the vapour film and the solid fin, the heat transfer mechanism is similar to thin film evaporation.

- for higher heat fluxes, nucleation occurred in all the inter-fin spaces, so that spherical bubbles are formed in close proximity to one another and coalesce. The newly merged bubble has greater buoyancy and increases its rate of ascension. As this boiling cycle cools down the fins, the vapour film left inside the fin spacing condenses and shrinks as the liquid starts to fill up the fin space all over again. This boiling mechanism is similar to annular flow in pipes.

Giraud et al. [10] analysed a finned geometry with water at sub-atmospheric pressure as refrigerants (under the typical operating conditions of LiBr/H₂O absorption chillers).

Visualization of the boiling mechanism was accomplished through a high-speed camera. Starting point for the analysis is that the major specificity of the pool boiling at low pressure lies in the non-homogeneity of the boiling environment, both in terms of pressure and subcooling degree. Indeed, at sub-atmospheric pressure, as the pressure is very low, the static head imposed by the liquid height can be of the same order of magnitude as the fluid saturation pressure. This non-homogeneity makes really different boiling phenomena than those usually observed

Visualization results showed that bubbles and regimes obtained at atmospheric pressure or at sub-atmospheric pressure for a given imposed heat flux are different: many bubbles of millimetres size are observed at atmospheric pressure water pool boiling whereas single bubble with centimetres size are observed at sub-atmospheric pressure. The departure diameter of these sub-atmospheric bubbles increases when decreasing the pressure. However, at very low pressures (< 2 kPa), bubbles are “Rayleigh bubbles” and expand owing to an excess of pressure derived from the superheat of the heated wall.

The particularity of the sub-atmospheric pool boiling not only lies in the bubbles size but also in the bubbles shape. Because of the highly non-homogeneous boiling environment, various shapes and sizes of bubbles in sub-atmospheric pressure pool boiling are observed. These shapes do not only depend on the pressure imposed but also on the history of the bubbles, i.e. size and frequency of preceding bubbles and on the movements of the free surface interface (due to the rise of bubbles). That is why even during a single experiment diverse bubbles are observed.

In the framework of the present project, the investigation on the evaporator was done in small-scale, but still in relevant dimensions (i.e. heat exchangers with estimated evaporation power of 2-3 kW) and therefore a precise identification of the boiling mechanism was not possible. However, an attempt to confirm the previous experimental works in the literature was done, to serve as the starting base for the definition of a model to correlate the measured data to the expected performance in realistic operating conditions.

Figure 74 shows an example of the pictures recorded from the viewports during the process. Even though they are not really clear, it is still evident that the phenomenon involves the formation of bubbles in centimetre size and a vigorous mixing of the pool.

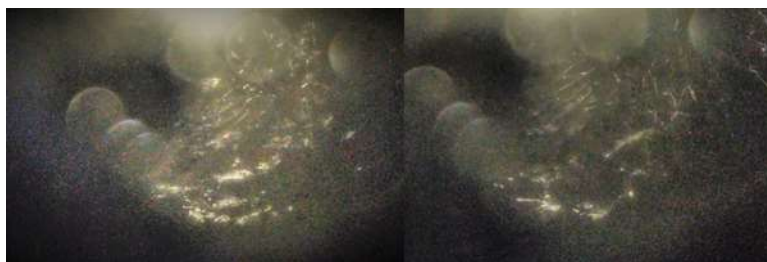


Figure 74: Recorded images during evaporation with $T_{in}=40^{\circ}\text{C}$ and $\Delta T_{pool}=5$ K.

The process can be better described by looking at the frames in Figure 75, where the formation and collapse of some bubbles is highlighted. The bubbles start forming in the lower part of the liquid, in contact with the heat exchanger (1) and move towards the surface (2), where they detach from the surface (3) assuming the form of a liquid jet (4), before collapsing (5). Once the process is finished, new bubbles will form (6)

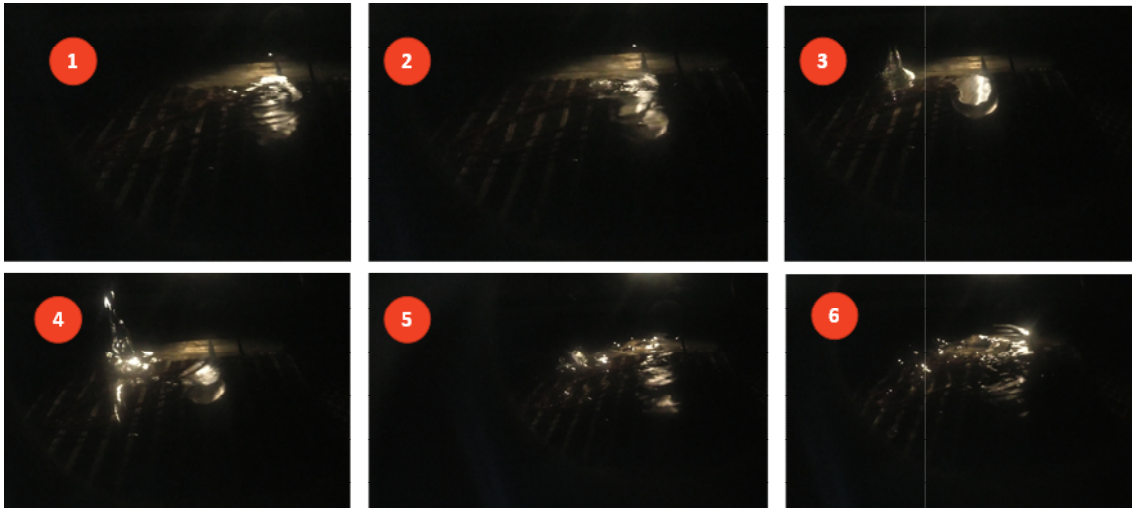


Figure 75: Process of formation and collapse of bubbles.

The process of bubble formation can be correlated to one of the parameters experimentally measured, i.e. the temperature of the liquid in the lower part of the evaporator. As exemplary cases, three tests were selected and compared in Figure 76: tests (a) and (c) are done under the same temperature conditions of the condenser and the evaporator, but changing the flow rate of the HTF, whereas the test (b) is done at the same flow rate of test (a), but under a lower temperatures at the evaporator (the temperature difference between evaporator and condensers is kept constant). It is possible to notice that changing the flow rate does not change the frequency of the process, represented by the time between two peaks in the “RTD liquid” temperature, but it does change the amplitude of the peaks which corresponds to a more vigorous phenomenon, with bigger bubbles and higher liquid jets. This is due to the better heat transfer between the HEX and the surrounding liquid, with a consequently higher local subcooling. On the contrary, reducing the temperature leads to a quasi-flat profile of the temperature, due to the lower ΔT_{pool} , that results in a lower driving force for the process.

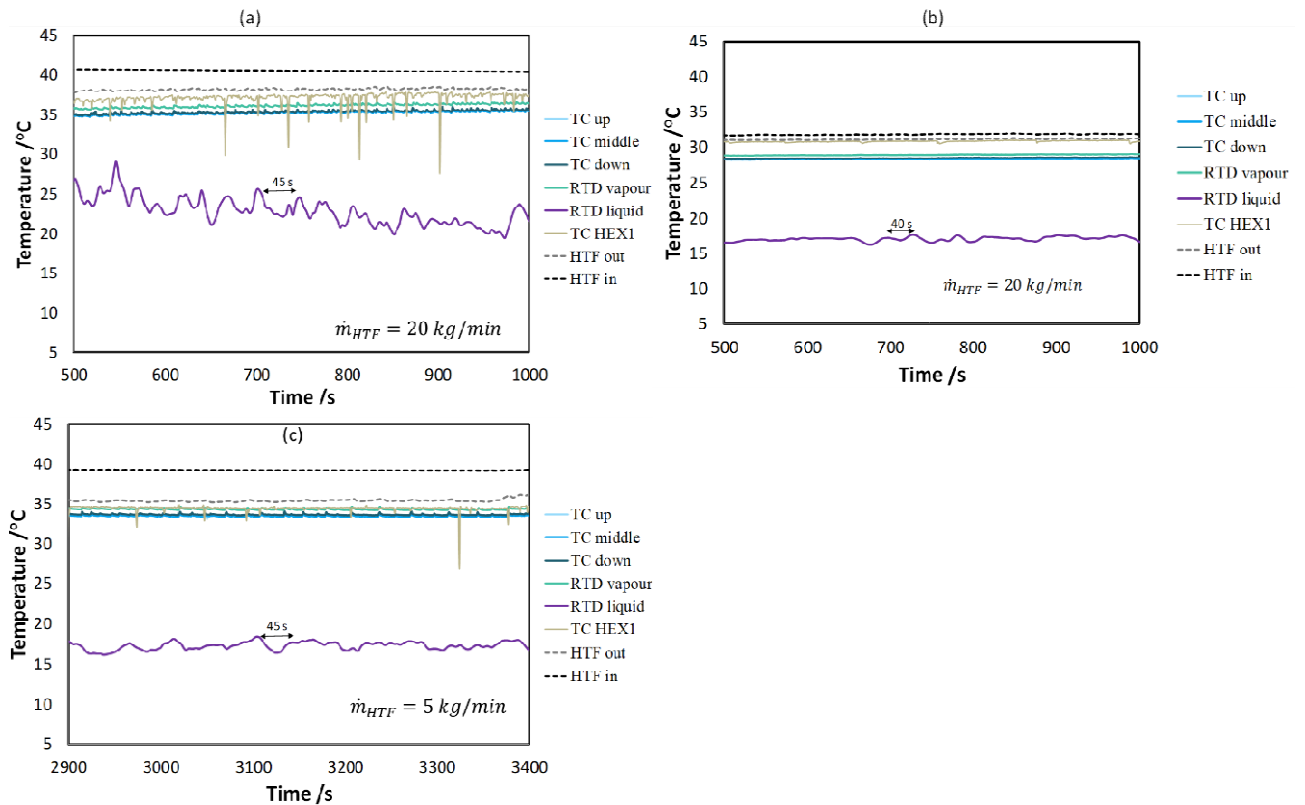


Figure 76: Effect of operating conditions on the bubble formation process.

In the case of the 45° arrangement, the same process occurs, the main difference with the case examined above is that the bubble formation and collapsing occurs at the interface between the heat exchanger and the pool of water, as shown in Figure 77.



Figure 77: Process of bubble formation and collapsing for 45° arrangement.

The same process was evaluated for the 90° inclination, and is depicted in Figure 78. In this case, the bubbles that are formed at the interface between the evaporator and the pool, due to the inclination of the heat exchanger, resemble more small jets than proper spherical bubbles, as was for the case of 45° inclination. Indeed, as previously shown, this has an influence on the evaporation power that the system can deliver.

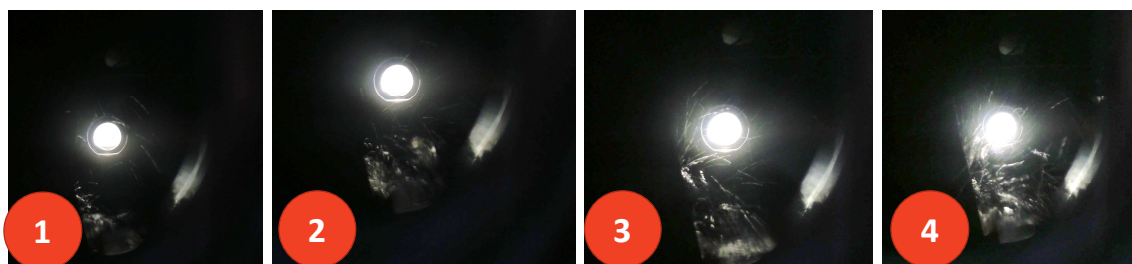


Figure 78: Process of bubble formation and collapsing for 90° arrangement.

4.4.2 Semi-empirical model

The considerations previously described about the evaporation mechanism were elaborated in order to have a semi-empirical model to be used for the sizing of the adsorber, in combination with the experimental results presented in the previous section. In particular, in accordance with what reported in [11], the results can be correlated to some dimensionless numbers commonly used in thermal engineering and fluid dynamics. In particular, a modified Jakob number was considered:

$$Ja_m = \frac{c_{p,liq} \Delta T_{pool}}{q_{ev}} \frac{p_{sat}}{p_{triple}}$$

Where $c_{p,l}$ is the specific heat of the liquid at the temperature of the evaporator pool, Δh_{ev} is the evaporation enthalpy of water, p_{sat} is the saturation pressure at the temperature of the vapour inside the evaporator and p_{triple} is the pressure of the triple point of water. Jakob number is particularly useful to describe the process since it takes into account the heat transfer contributions due to evaporation and sensible heating of the pool and, by means of the modification term $\frac{p_{sat}}{p_{triple}}$, the pressure of the process. As shown in Figure 79, there is a clear linear correlation between the modified Jakob number and the evaporation power measured. It is worth pointing out that the results refer to the tests done for both the 0° and 45° arrangement, thus proving the representativeness of the model.

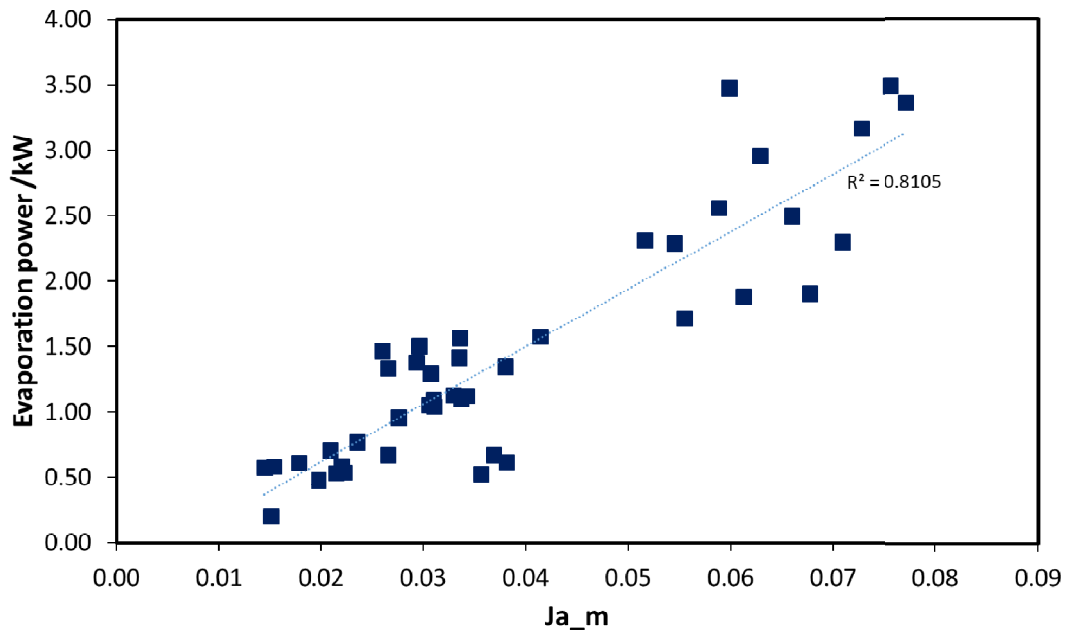


Figure 79: Correlation between the evaporation power and the Jakob number.

There is a correlation between the evaporation power and the Kutateladze number (2) as well [12]. The Kutateladze number (2) is defined as:

$$Ku2 = \frac{q_{ev}}{c_{p,liq} \Delta T_{pool}}$$

Therefore, similarly to Jakob number, can suitably describe the process and allow an experimental correlation as a function of the operating parameters (in this case, the temperatures inside the evaporator).

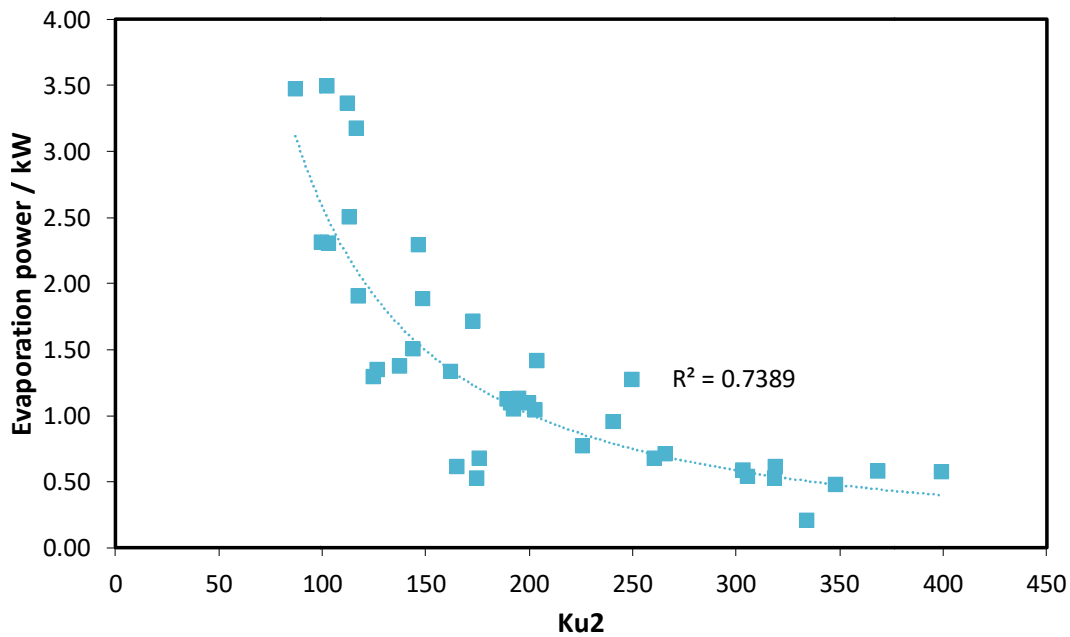


Figure 80: Correlation between evaporation power and Kutateladze number (2).

In addition, the overall heat transfer was correlated with a modified Bond number, a common group used in the description of bubbles and droplets formation [11,12], which corresponds to the ratio of gravitational force over surface tension force. Indeed, as already stated, the main forces influencing the process are static head due to the height of the liquid and the surface tension. The modified Bond number was calculated as:

$$Bo_m = \frac{g(\rho_{liq} - \rho_{vap})r_{crit}^2}{\sigma}$$

Where g is the gravitational constant, ρ_l and ρ_v are the fluid and vapour density, σ is surface tension of water and r_{crit} was calculated as[11]:

$$r_{crit} = \frac{2\sigma}{\Delta p}$$

Δp represents the pressure difference driving the process, which represents also one of the parameters known in the nominal operating conditions of the sorption module and therefore useful for its sizing. It can be calculated as:

$$\Delta p = \frac{p_{sat,cond}}{p_{sat,evap}}$$

Starting from these results, the full-scale evaporator was designed.

4.5 Full-scale evaporator/condenser design and manufacturing

Evaporator/condenser HEX (EC-HEX) in adsorption modules carry liquid water on the vacuum side surface. Since hydrogen in water is reduced by metallic Al forming gaseous H_2 any corrosion of the aluminium results in a pressure increase. Already a small pressure increase of 2-3 mbar decreases the sorption rates significantly.

Fahrenheit is working already on this topic. We have tried different measures to overcome this problem but until now there is no satisfying solution.

For this reason Fahrenheit has suggested to use full copper EC-HEX instead of aluminium parts. This will guarantee the long-term operation of test installations and of the demonstrators

without pressure increase in the modules. Accordingly, a powerful EC-HEX based on finned copper tubes have been designed and constructed. This solution works already fine with Fahrenheit actual generation of zeolite adsorption machines.



Figure 81: Sample for finned copper tubes

The concept of using this type of heat exchanger is based on the capillary effect of thin film evaporation between the fin slots. This makes it possible to reduce overall surface area for evaporation because the HEX extracts the water automatically out of a defined water pool. This water pool is calculated by the possible amount of adsorbed water on the one side and the optimal filling level of the fin tubes on the other side. These functionalities make it easy to use the HEX also as condenser part so that the pool works dynamically with different filling levels during the adsorption process but with really good cooling capacities over the whole cycle (no limitation on evaporator site). In that case FAHR also did measurements with different types of heat exchanger in adsorption modules. The first type was an Al heat exchanger with fins (microchannel HEX similar to the AKG one), the second one is the fin tube HEX FAHR built for the zeolite technology.

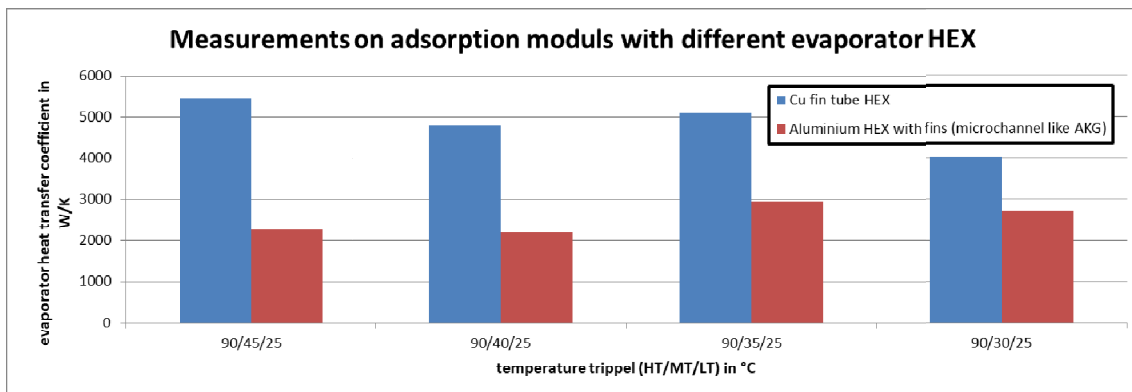


Figure 82: Heat transfer measurements on different evaporator

In Figure 82 you can see, that the copper fin tube HEX (vertical position) works really better as evaporator under different adsorption conditions in relation to a microchannel HEX based on Al fins (horizontal position). Both HEXs were measured with the same adsorber and the same footprint, but with different heat transfer areas of at least 80% and different thermal mass of over 60%. Figure 83 shows the capillary effect onto a finned copper tube, which will be the basis for the final design.

This experience FAHR have collected should be used to build up the prototype for this project. To scale-up the evaporator to the final size for the demo sites, FAHR needs the results of the coated HEX (final size) gets from AKG for the adsorber because the evaporator size is directly

dependent on the zeolite mass FAHR can coated on that HEX. In general, the footprint will be in the first approximation the same as the adsorber configuration, like 722x830 mm.

The EC-HEX will be completely produced by Fahrenheit, exploiting the expertise gained in the manufacturing of HEXs for adsorption modules.



Figure 83: Capillary effect for good heat transfer without big surface areas

5 Conclusions

In the present deliverable, the activity done within T2.1 is presented, including the overall development of the sorption module. The activity was focused on the realization of high-performance components for the sorption module. Different porous structures for the crystallization of zeolite of the adsorber were tested and high-density pressed fins were selected. The full-scale adsorber was consequently sized and manufactured. The experimental activity was coupled to the development of a numerical model, validated by means of experiments in small-scale heat exchangers, to allow for an optimization of the system.

The second part of the activity was devoted to the analysis of evaporators in sub-atmospheric conditions. A testing rig was specifically designed and built at ITAE and used for testing different configurations under thin film and pool boiling conditions. The results were used to validate semi-empirical correlations from the literature and the full-scale evaporator for the demonstration sites was designed.

The development activity allowed the realization of a module with a high packing factor, i.e. $305 \text{ kg}_{\text{adsorbent}}/\text{m}^3_{\text{adsorber}}$, with an expected power density up to $390 \text{ kW}/\text{m}^3$. Particular focus was put on the simple realization of the system: to this aim, among the different configurations, the one presenting the easiest production method was chosen. In addition, the evaporator developed will present a heat transfer capacity higher than $3 \text{ kW}/\text{m}^2\text{K}$, with a significant improvement compared to the state-of-art (i.e. up to 200%), without, however introducing reliability and durability issues in the system, thanks to the use of copper heat exchanger and already tested solutions in full-scale by Fahrenheit.

6 References

- [1] A. Freni, G. Maggio, F. Cipiti, Y.I. Aristov, Simulation of water sorption dynamics in adsorption chillers: One, two and four layers of loose silica grains, *Appl. Therm. Eng.* 44 (2012) 69–77. doi:10.1016/j.applthermaleng.2012.03.038.
- [2] W.M. Rohsenow, J.P. Hartnett, Y.I. Cho, *Handbook of heat transfer*, McGraw-Hill, 1998.
- [3] V. V. Calmidi, R.L. Mahajan, The Effective Thermal Conductivity of High Porosity Fibrous Metal Foams, *J. Heat Transfer.* 121 (1999) 466. doi:10.1115/1.2826001.
- [4] I.I. El-Sharkawy, On the linear driving force approximation for adsorption cooling applications, *Int. J. Refrig.* 34 (2011) 667–673. doi:10.1016/J.IJREFRIG.2010.12.006.
- [5] A. Sapienza, S. Santamaria, A. Frazzica, A. Freni, Y.I. Aristov, Dynamic study of adsorbents by a new gravimetric version of the Large Temperature Jump method, *Appl. Energy.* 113 (2014) 1244–1251. doi:10.1016/J.APENERGY.2013.09.005.
- [6] S. Santamaria, A. Sapienza, A. Frazzica, A. Freni, I.S. Girnik, I. Aristov, Yuri, Water adsorption dynamics on representative pieces of real adsorbents for adsorptive chillers, *Appl. Energy.* 134 (2014) 11–19. doi:10.1016/J.APENERGY.2014.07.053.
- [7] Y.I. Aristov, B. Dawoud, I.S. Glaznev, A. Elyas, A new methodology of studying the dynamics of water sorption/desorption under real operating conditions of adsorption heat pumps: Experiment, *Int. J. Heat Mass Transf.* 51 (2008) 4966–4972. doi:10.1016/J.IJHEATMASSTRANSFER.2007.10.042.
- [8] *VDI-Wärmeatlas*, Springer Berlin Heidelberg, Berlin, Heidelberg, 2002. doi:10.1007/978-3-662-10743-0.
- [9] M.A. Chan, C.R. Yap, K.C. Ng, Pool Boiling Heat Transfer of Water on Finned Surfaces at Near Vacuum Pressures, *J. Heat Transf.* 132 (2010) 1–6. doi:10.1115/1.4000054.
- [10] F. Giraud, R. Rullière, C. Toublanc, M. Clause, J. Bonjour, Experimental evidence of a new regime for boiling of water at subatmospheric pressure, *Exp. Therm. Fluid Sci.* 60 (2015) 45–53. doi:10.1016/j.expthermflusci.2014.07.011.
- [11] F. Giraud, C. Toublanc, R. Rullière, J. Bonjour, M. Clause, Experimental study of water vaporization occurring inside a channel of a smooth plate-type heat exchanger at subatmospheric pressure, *Appl. Therm. Eng.* 106 (2016) 180–191. doi:10.1016/j.applthermaleng.2016.05.151.
- [12] J. Kunes, *Dimensionless Physical Quantities in Science and Engineering*, First edit, Elsevier, London, 2012.